Towards a measurement of the electric dipole moment of the electron with YbF molecules

Christopher Junhong Ho

A thesis submitted in partial fulfilment of the requirements
of the degree of Doctor of Philosophy

Department of Physics
Imperial College London

October 2020

Declaration

I declare that the work presented in this thesis is my own. I have acknowledged the work of others or referenced the correct sources wherever required in this thesis.

Abstract

The search for electric dipole moments (EDMs) of particles has been an active field of research for the past 70 years. Scientific interest in EDMs stems from the fact that these are direct signals of parity symmetry (P) violation, and time-reversal symmetry (T) violation. In most extensions to the Standard Model, new CP-violating interactions that can help explain the origin of the observed matter-antimatter asymmetry in the universe also predict particle EDMs with sizes that current and near-future experiments are sensitive to. The current best measurements of the electron EDM (eEDM) have already constrained the energy scale of a broad class of CP-violating interactions to energies above 3 TeV.

I describe progress towards a measurement of the eEDM using a beam of YbF molecules. I implement a method that distills the molecular population into the required quantum state, and a new method for detecting the molecules with higher efficiency. I characterise the imperfections in this detection scheme. By minimising the impact of these imperfections and various sources of technical noise, I demonstrate an improvement in the shot-noise limited sensitivity by a factor of 14.5 since the last published measurement. The actual noise is limited by magnetic noise to 2.1 times this shot-noise limit. A measurement of the eEDM at this shot-noise-limited sensitivity would improve constraints of new CP-violating interactions by a factor of 3.2, and I present an outlook for such a measurement.

Acknowledgements

The work done in this thesis would not have been possible without the excellent guidance of my supervisors – Ben, Mike and Ed. I have been very fortunate to have had such hands-on supervisors who have supported, corrected and motivated me throughout my PhD. I want to thank Jack and Izzie for helping me find my feet in the lab when I first joined, and for constantly checking in on the progress of the experiment. The work presented in this thesis has very much been built on the foundations of their PhD work. I also benefitted from the experience and help that Pauline, Sid and Jongseok provided when they joined the experiment during the latter stages of my PhD. I acknowledge significant help from both Jongseok and Joanna for numerical simulations done in this thesis. I am indebted to Jon, Dave and Gio in the mechanical workshop for being a reliable and excellent source of technical help and ideas. For sorting out my innumerable administrative headaches, especially when it came to visa applications, I am incredibly thankful to Sanja and Miranda. The time spent on this work would have been significantly less enjoyable were it not for the people that make up CCM, and I especially want to thank Pauline, Mike, Sid and Thom for keeping spirits up in the office or lab when things have been looking bleak. Dance was a significant part of my time at Imperial and a much-needed respite from work at times, and I am grateful to everyone at Imperial College Dance Club, especially Adela, Devon, Ben and Ev. I want to also thank Ben and Max for keeping me sane throughout the writing process. To Daphne, thank you for your constant love, support, encouragement and enthusiasm, for sharing in both the joys and frustrations of my PhD. Finally, and most importantly, to my parents who have always backed me and believed in me, thank you for giving me the opportunities that have led me to where I am today; this thesis is dedicated to you both.

Contents

List of Figures

List of Tables

1. Introduction

1.1. Electric dipole moments, parity conservation and time-reversal symmetry

The possibility of fundamental particles possessing electric dipole moments (EDMs) was first proposed by Purcell and Ramsey in 1950 [1]. At the time, the widely held view was that particles cannot have EDMs because the physical laws of nature are invariant under reflections in space, which is known as parity symmetry. To see this, consider a particle that has internal angular momentum $\mathbf{j}$ and a dipole moment $\mathbf{d}$, as shown in Fig. 1.1. The dipole moment operator is a vector operator, and by the Wigner-Eckart theorem, it must therefore lie along the same axis as the angular momentum [2, p. 199]:

$$\mathbf{d} = \alpha \mathbf{j}. \tag{1.1}$$

The parity operation reverses the sign of $\mathbf{d}$ but not $\mathbf{j}$, which implies that either the dipole moment must be zero, or the two states linked by a parity operation are degenerate [3]. Additionally, the time-reversal operation reverses the sign of $\mathbf{j}$ but not $\mathbf{d}$, which leads us to the same conclusion. Fundamental particles such as neutrons and electrons are known to obey the Pauli exclusion principle, which rules out any degeneracy in the same quantum state. A non-zero EDM in these particles would therefore violate both parity symmetry (P) and time-reversal symmetry (T), as was first pointed out by Landau [4].

It should be noted that the usual electric dipole moments of polar molecules do not violate P and T. These “molecule-frame” dipole moments only arise when a sufficiently strong electric field is applied to orient the molecule. In the weak-field limit, these molecular dipole moments vanish in the laboratory frame. Another way of looking at it

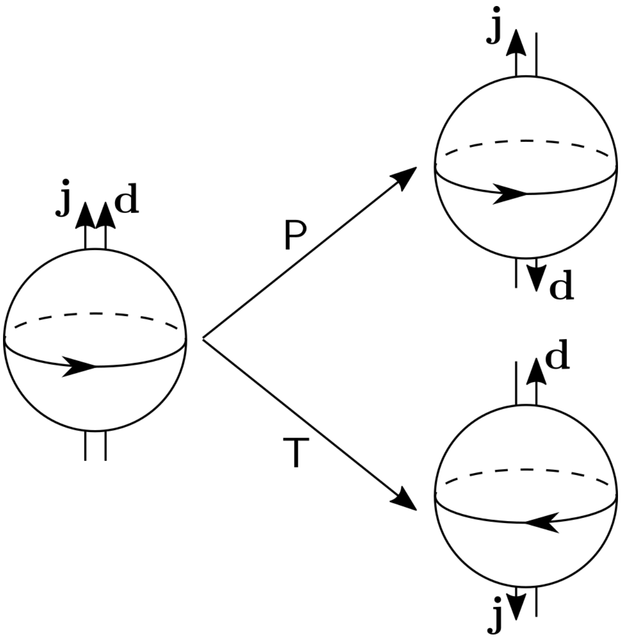

Figure 1.1.: A particle which has angular momentum **j** and electric dipole moment **d** violates both P and T.

is to consider the electric dipole interaction $-\boldsymbol{\mu}_{\text{mol}} \cdot \mathbf{E}$, where $\boldsymbol{\mu}_{\text{mol}}$ is the molecular dipole moment and $\mathbf{E}$ is an applied electric field. Since the alignment of the molecule depends on the direction of the electric field, the direction of $\boldsymbol{\mu}$ reverses when $\mathbf{E}$ is reversed. The interaction term therefore does not change sign under reversal of $\mathbf{E}$. A fundamental EDM $\mathbf{d}$ does not depend on an external field, therefore the EDM interaction term $-\mathbf{d} \cdot \mathbf{E}$ does reverse sign when $\mathbf{E}$ reverses.

1.1.1. Evidence for violation of parity and time-reversal symmetries

Although no experimental evidence for non-zero particle EDMs has been found thus far, violation of P and T have been separately observed in other systems. Parity violation was first demonstrated by Wu and coworkers [5] in the β-decay of ^{60}Co, then shortly afterwards in the decay of π^+ mesons [6, 7]. In the Wu experiment, it was observed that in the β-decay process, electrons were preferentially emitted in the opposite direction to the nuclear spin of ^{60}Co (which has been called “left-handed” decay). If this process obeyed P, then we would expect "right-handed" decay, where electrons are emitted in the same direction as the nuclear spin, to occur with equal probability.

Direct evidence of T violation was first observed in the B meson system by the BaBar collaboration [8]. The experiment they carried out measured differences in the forward and reverse transition rates of several decay processes in neutral B mesons. Crucially, the initial and final states of the decays were linked by a time-reversal operation, which enabled a direct method of measuring T-violating effects, independent of other symmetry-violating effects such as CP violation [9].

CP refers to the symmetry under the combined action of parity and charge conjugation (C). The latter refers to symmetry under the exchange of particles and anti-particles. The violation of CP is also relevant here because of the CPT theorem, which states that any local, Lorentz-invariant quantum field theory is invariant under the combined action of C, P and T [10–13]. CPT invariance is a property of the Standard Model and of most popular extensions of the Standard Model, and is supported by all experimental tests carried out so far [14, see Tests of Conservation Laws]. Assuming CPT invariance allows us to interpret experimental observations of CP violation in the K meson [15] and B meson [16] systems as indirect evidence for T violation as well.

CP violation is also important for cosmology, and in particular hitherto undiscovered CP-violating processes may be the origin of the observed matter-antimatter asymmetry in the universe. The latter is also known as the baryon asymmetry of the universe (BAU), and its origin can be attributed to either a matter-antimatter asymmetric initial state of the universe, or to *baryogenesis* processes that occurred shortly after the Big Bang which created the asymmetry from an initially symmetric state [17]. Sakharov [18] showed that the necessary ingredients for baryogenesis are (i) violation of baryon number, (ii) C and CP violation and (iii) deviation from thermal equilibrium. Since no significant amount of antimatter remains in the universe, and the product of annihilation processes between matter and antimatter is photons, one can estimate the size of the BAU by the baryon to photon ratio, $\eta = N_B/N_\gamma$. This ratio has been measured independently from cosmic abundances of elements created during big bang nucleosynthesis and the cosmic microwave background (CMB), and found to be $\eta \sim 10^{-10}$ [19].

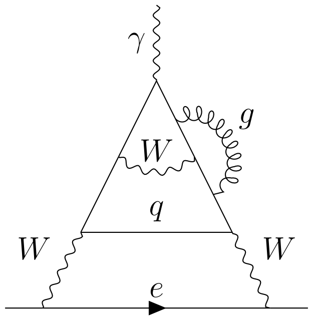

Figure 1.2.: Example of a lowest-order Feynman diagram showing how an electron EDM can be generated within the Standard Model, adapted from [24].

1.1.2. Overview of theoretical models

The Standard Model of particle physics (SM) was being developed when the experiments that discovered P violation [5] and CP violation [15] were carried out. It is no surprise then that the SM accounts for these symmetry violations. P is violated maximally by the V-A interaction in weak processes, which only allows the W boson to couple to either left-handed particles or right-handed anti-particles [20]. CP violation occurs in the complex phase in the Cabibbo-Kobayashi-Maskawa (CKM) matrix, which governs quark mixing in the electroweak sector [21]. Although it is possible for the strong interaction to violate CP via a term in the QCD Lagrangian parametrised by θ, current experimental results on the neutron EDM limit the size of the θ parameter to $\theta \lesssim 10^{-10}$ [22]. The extremely small value for θ constitutes the "strong CP problem": since a CP-violating term is allowed in the strong interaction, why is it so highly suppressed? The resolution to this puzzle may lie in the existence of an axion field [23], which has been proposed as a dark matter candidate as well, though it remains undetected thus far.

Nevertheless, almost all the experimental results for P, CP and T violations described above agree with SM predictions[1]. The exception here is the observed baryon asymmetry of the universe, η, which is far too large to have been produced by the CP-violating CKM phase in the SM [17]. This, together with many issues such as the aforementioned strong CP problem, the existence of dark matter and non-zero neutrino masses, motivate the need for beyond-Standard-Model (BSM) theories. These theories generally include additional sources of CP violation, which would generate T-violating phenomena such as particle EDMs [22]. CP violation in the SM, via the CKM matrix, generates EDMs

---

[1] The SM obeys the CPT theorem, so CP violation in the CKM matrix also implies T violation.

that are many orders of magnitude smaller than current experimental sensitivities. For example, the lowest-order Feynman diagram that contributes to a non-zero electron EDM is a four-loop diagram; an example is shown in Fig. 1.2. The SM prediction for the eEDM is $d_e \leq 10^{-38}\, e\,\text{cm}$[2] [24], while the current experimental bound for it is $d_e < 1.1 \times 10^{-29}\, e\,\text{cm}$ (90% confidence limit) [25]. Experimental searches for particle EDMs are therefore background-free[3] probes of new physics beyond the SM, and even null results can set stringent limits on CP-violating mechanisms in BSM theories [22, 26, 27].

1.1.3. Theoretical interpretation of EDMs

A convenient and model-independent way to discuss the observation of BSM physics is effective field theory (EFT). A schematic of this is shown in Fig. 1.3. EFT makes the assumption that new physics occurs at high energy scales, and the SM can be viewed as an effective "low-energy limit of a more fundamental theory" [28]. Below the energy scale E_{new} at which new particles appear, the effect of BSM physics can be described by a set of effective low-energy operators which involve only SM fields [29]. Taking into account only CP-violating (CPV) terms, the effective Lagrangian can be written at the electroweak scale ($E_{\text{EW}} \sim 246\,\text{GeV}$) as [29]

$$\mathcal{L}_{\text{CPV}} = \mathcal{L}_{\text{CKM}} + \mathcal{L}_{\theta} + \mathcal{L}^{\text{eff}}_{\text{BSM}}, \tag{1.2}$$

where $\mathcal{L}_{\text{CKM}}$ and $\mathcal{L}_{\theta}$ are the CPV terms due to the CKM matrix and the strong interaction within the SM description, and are of dimension four. The effective CPV BSM terms are of dimension six, and can be written as [29]

$$\mathcal{L}^{\text{eff}}_{\text{BSM}} = \frac{1}{\Lambda^2} \sum_i \alpha_i \mathcal{O}_i, \tag{1.3}$$

---

[2] According to Ref. [24], a CKM-induced electron EDM is, in fact, several orders of magnitude lower at $d_e \sim 10^{-44}\, e\,\text{cm}$. This is the calculated value from four-loop diagrams such as the one in Fig. 1.2. The main P and T-violating signal from the CKM matrix in the Standard Model actually comes from a scalar electron-nucleon coupling, parametrised by C_S (more on this later). However, electron EDM experiments are unable to distinguish between d_e and C_S, and this CKM-induced electron-nucleon coupling produces an equivalent d_e of order $10^{-38}\, e\,\text{cm}$.

[3] The background here refers to observables predicted by Standard Model physics.

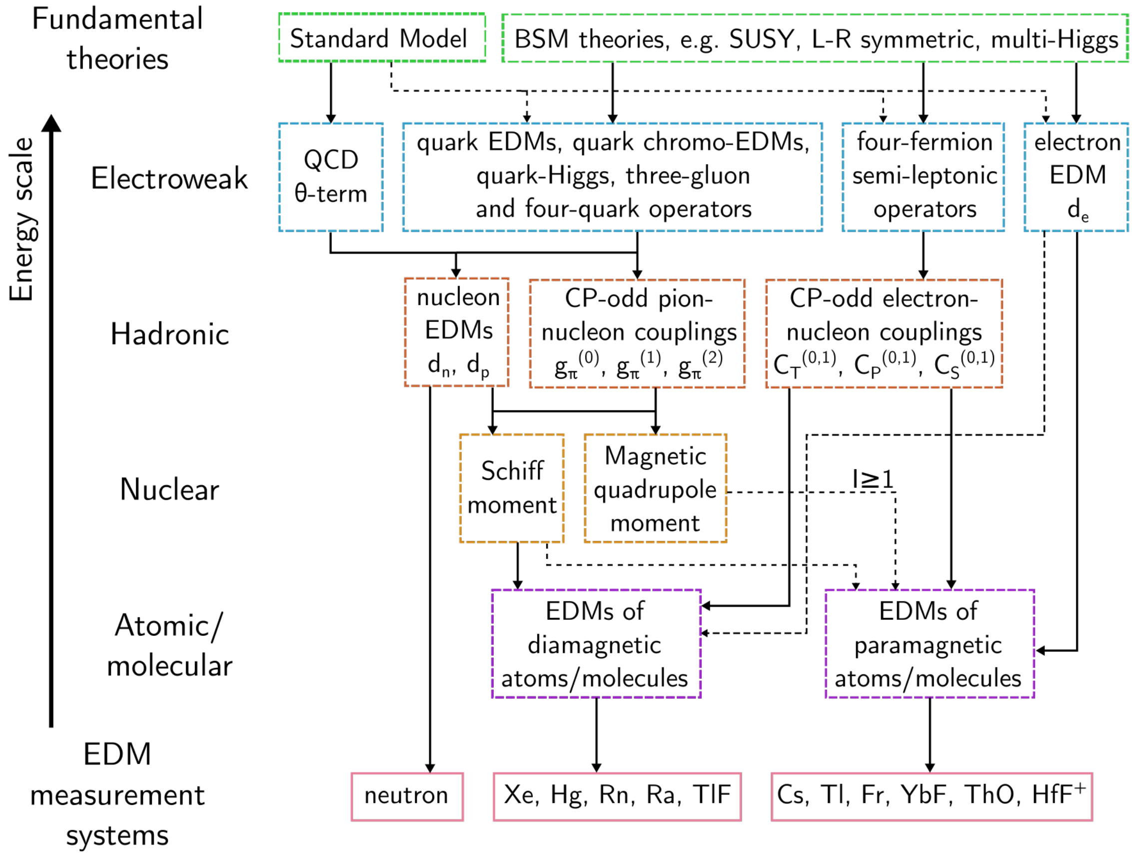

Figure 1.3.: Schematic showing how CP-violating physics in the SM and BSM theories at high energy scales can lead to observable EDMs in low-energy atomic and molecular systems. Solid (dashed) arrows indicate strong (weak) contributions from higher-energy interactions to effective lower-energy ones.

where Λ is the energy scale of BSM physics, the α_i's are Wilson coefficients which encapsulate the details of the exact nature of BSM physics at higher energies, and the $\mathcal{O}_i$'s are SM operators. It turns out that there are twelve possible $\mathcal{O}_i$ terms in Eq. (1.3), which include electron and quark EDMs, quark chromo-EDMs, semi-leptonic interactions, as well as four-quark and three-gluon couplings. Although the SM can contribute to these terms via the CKM mechanism, its effect is negligibly small compared to proposed BSM contributions [29]. A full list and description of these terms can be found in [22] or [29]. Any underlying BSM theory can be expressed as Eq. (1.3) at the electroweak scale, thus the EFT formalism can be used to interpret a wide range of experiments in a model-independent way.

While particle physics experiments can access the electroweak scale, tabletop atomic and molecular EDM experiments operate at much lower energy scales. EFT is used again to bridge the gap: the Lagrangian in Eq. (1.2) can be expressed in terms of effective low-energy operators and coefficients when moving down energy scales [29] as shown in Fig. 1.3. One would first match the terms in Eq. (1.3) to effective CP-violating interaction terms at the hadronic scale ($E_{\text{hadron}} \sim 1\,\text{GeV}$): electron-nucleon couplings, pion-nucleon couplings and nucleon EDMs. This would be sufficient for interpreting neutron EDM experiments, but for atomic and molecular experiments one would need to match the terms at the hadronic scale to terms at the nuclear, atomic and molecular scales. At the nuclear scale, the interaction terms are due to P- and T-violating nuclear moments. The lowest such electric moment is the "Schiff moment", which is effectively a dipole moment that takes into account the effect of electron shielding, and the lowest such magnetic moment is the magnetic quadrupole moment (MQM)[4] [31]. Finally, the dependencies of the EDMs of paramagnetic and diamagnetic atoms and molecules on nuclear moments, the electron EDM and electron-nucleon couplings can be calculated from atomic theory [31].

The EDMs of heavy paramagnetic atoms and molecules are primarily sensitive to the electron EDM, d_e, and the scalar electron-nucleon coupling, C_S [32]. The MQM contributes as well if the nuclear spin is greater than 1/2 [31]. On the other hand, the dominant contributions to the EDMs of heavy diamagnetic atoms and molecules are the tensor electron-nucleon coupling, C_T, and the isoscalar and isotensor pion-nucleon couplings, $g_\pi^{(0)}$ and $g_\pi^{(1)}$. One way to constrain these parameters is to adopt the single-source approach, where the atomic or molecular EDM is assumed to arise solely from one cause. This is the way most EDM results are reported; for example, the most recent limit on the electron EDM set the limit $d_e < 1.1 \times 10^{-29}\, e\,\text{cm}$ assuming that $C_S = 0$, and also gave $C_S < 7.3 \times 10^{-10}$ while assuming $d_e = 0$ [25]. An alternative method to constrain these parameters is to carry out a global fit, for example in [32]. The global analysis has the advantage that two separate results from different molecules can often constrain the parameters better than either of the results alone [32]. This last point motivates using a variety of experimental systems to measure fundamental P- and T-violating phenomena.

---

[4] A non-zero MQM requires a nuclear spin of $I \geq 1$ due to angular momentum selection rules [30]

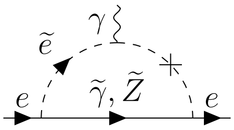

Figure 1.4.: Example of a one-loop diagram showing how an electron EDM can be generated in supersymmetry, adapted from [27]. The tildes indicate superpartners of regular SM fields and the cross indicates a CP-violating phase due to breaking of supersymmetry at low energies.

1.1.4. Connection to particle physics

Particle physics experiments have long sought evidence of new, massive particles through direct production of these in colliders. The possibility of the existence of these new particles have been introduced by a variety of theories that extend the Standard Model, such as supersymmetry, left-right symmetric models and multi-Higgs models. The current upper limits to the mass of these new particles can be found in [33]. To give an example, the mass of the selectron particle must be higher than 0.7 TeV based on the most recent experimental data from the Large Hadron Collider.

EDM experiments, on the other hand, probe the existence of these massive particles by their impact on a low-energy particle, such as an electron. An example of a one-loop correction to the electron EDM due to the selectron is shown in Fig. 1.4. The strength of the constraint that an EDM measurement places on the masses of these particles are dependent on the exact mechanism of EDM generation. However, one can make rough estimates. For example, Cesarotti and coworkers have shown that the best constraint of the electron EDM thus far limits the mass of the selectron to above 50 TeV for one-loop diagrams and 3 TeV for two-loop diagrams [34]. Thus, EDM measurements can complement direct searches for new, heavy particles with collider experiments by probing their indirect effect on the EDMs of low-energy particles. Moreover, with further improvements in measurement sensitivity, the mass reach of EDM experiments can even exceed that of the LHC.

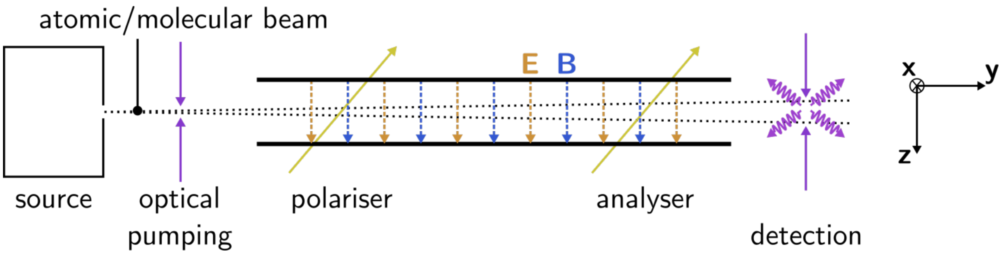

Figure 1.5.: Schematic of a beam-type EDM experiment.

1.2. Measuring the electron EDM with atoms and molecules

In this work, we are interested in measuring the electron EDM (eEDM). Such experiments usually measure the EDM of paramagnetic atoms or molecules and then derive a limit on the eEDM from the result. These experiments usually employ some variant of Ramsey's separated oscillatory fields method [30] to measure small energy shifts due to the EDM interaction. A simple schematic of a beam-type experiment is shown in Fig. 1.5. An atomic or molecular beam, which can be continuous or pulsed, is produced by a source. There is usually an optical pumping step which aims to increase the number of useful atoms or molecules in the experiment by preparing them in a single quantum state, and deplete the population in states which might otherwise interfere with the rest of the experiment. The beam then enters a region of uniform electric ($\mathbf{E}$) and magnetic ($\mathbf{B}$) fields which are aligned along the laboratory z-axis. The atoms or molecules are then prepared in a state where their spins are aligned along the x-axis. This "polariser" step is equivalent to the $\pi/2$-pulse of rf applied in a typical Ramsey-type experiment. The spins precess in the xy-plane for a time τ, at a rate

$$\omega = (\mu\mathbf{B} + d\mathbf{E}) \cdot \frac{\mathbf{F}}{\hbar|F|}, \tag{1.4}$$

where μ and d are the magnetic moment and EDM of the atom or molecule and $\mathbf{F}$ is its total angular momentum. At the end of the precession region, an "analyser" step maps the precession phase $\phi = \omega\tau$ onto the population of another state, which is typically detected by laser-induced fluorescence (LIF). The EDM, d, can be measured by reversing the direction of $\mathbf{E}$ relative to that of $\mathbf{B}$ and measuring the change in the precession frequency ω.

Paramagnetic atoms and molecules are favoured when it comes to measuring the eEDM because of the large enhancement of the latter in these systems. I will now discuss how this enhancement arises and give an overview of eEDM experiments.

1.2.1. Paramagnetic atoms

The idea of interpreting limits of EDMs of paramagnetic atoms or molecules as limits on the eEDM was initially not considered promising because of a theorem by Schiff [35], which states that the EDM interaction of an atom or molecule with an electric field is zero even if its constituent electrons and nucleons have non-zero EDMs. This can be understood as follows. Consider an electrically neutral system composed of point particles with electrostatic forces between them. If an external electric field is applied, the system remains neutral and so the electrostatic forces on each of its constituent particles must vanish. Then, even if the particles have EDMs, since the average electric field at each particle is zero due to shielding from the other particles, there is no first-order energy shift. However, this is true only in the non-relativistic limit. Sandars [36] showed that if relativistic effects were taken into account, then not only does an eEDM give rise to an atomic EDM, but in fact for heavy paramagnetic atoms the atomic EDM can be much larger than the eEDM. For an atom with an unpaired valence electron, the energy shift due to the eEDM can be calculated in the framework of the Dirac equation as [36, 37]

$$\Delta E_{\text{edm}} = -\left\langle\phi_0\right|(1-\beta)d_e\mathbf{\Sigma}\cdot\mathbf{E}_{\text{t}}\left|\phi_0\right\rangle, \tag{1.5}$$

where $|\phi_0\rangle$ is the Dirac four-component spinor of the electron, $\beta = \left(\begin{smallmatrix}\mathbf{1} & 0\\ 0 & -\mathbf{1}\end{smallmatrix}\right)$ and $\mathbf{\Sigma} = \left(\begin{smallmatrix}\boldsymbol{\sigma} & 0\\ 0 & \boldsymbol{\sigma}\end{smallmatrix}\right)$ are Dirac matrices, and $\boldsymbol{\sigma}$ is a vector of the three Pauli spin matrices. The total electric field $\mathbf{E}_{\text{t}} = \mathbf{E}_{\text{int}} + \mathbf{E}_{\text{ext}}$ is the sum the internal field $\mathbf{E}_{\text{int}}$ and an externally applied field $\mathbf{E}_{\text{ext}}$, and $|\phi_0\rangle$ is the electronic wavefunction. As Sandars notes [36], the dependence on the external field "is contained both within the operator and in the wavefunction" since the atom is partially polarised by the external field. Treating the external field as a perturbation, the resulting energy shift can be written to first order in $\mathbf{E}_{\text{ext}}$ as [38]

$$\Delta E_{\text{edm}} = -2d_e\sum_{n\neq 0}\frac{\left\langle\phi_0\right|\mathbf{r}\cdot\mathbf{E}_{\text{ext}}\left|\phi_n\right\rangle\left\langle\phi_n\right|(1-\beta)\mathbf{\Sigma}\cdot\mathbf{E}_{\text{int}}\left|\phi_0\right\rangle}{E_0-E_n} - d_e\left\langle\phi_0\right|(1-\beta)\mathbf{\Sigma}\cdot\mathbf{E}_{\text{ext}}\left|\phi_0\right\rangle. \tag{1.6}$$

Table 1.1.: Enhancement factors for some heavy atoms.

Atomic species	R
Cs	124 [40]
Tl	-585 [40]
Fr	895 [41]
Xe	-0.008 [42]
Hg	0.012 [42]

The first term is the energy shift due to the interaction of the eEDM with the internal electric field that arises when the external field mixes higher-lying states of opposite parity, $|\phi_n\rangle$, with the ground state $|\phi_0\rangle$. The second term comes from the interaction of the eEDM with the external field. For heavy paramagnetic atoms, it can be shown that the first term is of order $Z^3\alpha^2$, while the second term is of order $Z^2\alpha^2$ [39], where Z is the atomic number and α is the fine structure constant[5]. The second term is therefore negligible for heavy atoms and the EDM energy shift can be estimated as [37, 39]

$$\Delta E_{\text{edm}} \approx -10 Z^3 \alpha^2 d_e E_{\text{ext}}, \tag{1.7}$$

where E_{ext} is the magnitude of the external field. Since the energy shift due to the interaction of an EDM of a bare electron in an external field is $-d_e E_{\text{ext}}$, one can define an enhancement factor that heavy paramagnetic atoms provide for the eEDM:

$$R = \frac{d_{\text{atom}}}{d_e} \approx 10 Z^3 \alpha^2. \tag{1.8}$$

Some values for R for heavy atoms, calculated more carefully than the estimate above, are tabulated in Table 1.1. I have included calculations for some diamagnetic atoms (Xe and Hg) as well for completeness. The contribution of the eEDM to the EDMs of diamagnetic atoms enters at one order higher in perturbation theory than that of paramagnetic atoms, via the hyperfine interaction [31]. The factor R is not really an "enhancement" in this case, but nevertheless it can be calculated.

The best experimental limits for the eEDM from atomic systems, assuming that d_e is the sole source of the atomic EDM, are given in Table 1.2. Despite the insensitivity of the EDM of diamagnetic Hg to the electron EDM, the extraordinary precision of the Hg experiment [45] means that it is able to set an extremely stringent limit on d_e, if

---

[5] See Appendix A for an explanation of these estimates.

Table 1.2.: Experimental limits on d_e (with confidence limits) set by some heavy atoms, assuming that the eEDM is the sole contribution to the atomic EDM.

Atomic species	Upper bound on d_e (e cm)
Cs	5.7×10^{-26} [43] (68% C.L.)
Tl	1.6×10^{-27} [44] (90% C.L.)
Hg	6.2×10^{-28} [45] (95% C.L.)

we assume that other sources of T violation in the Hg atom are zero. However, since the EDM of Hg is also sensitive to P- and T-violating nucleon EDMs and pion-nucleon couplings, the Tl result would be more constraining in a global analysis of P- and T-violating parameters.

Ultimately, the Tl experiment was limited by three large systematic effects [44, 46]. First, there is a "motional magnetic field" generated in the moving frame of the atoms, $\mathbf{B}_\mathrm{m} = (\mathbf{v} \times \mathbf{E})/c^2$, where $\mathbf{v}$ is the velocity of the atoms and $\mathbf{E}$ is the applied electric field. If $\mathbf{B}$ and $\mathbf{E}$ were slightly misaligned, then $\mathbf{B}_\mathrm{m}$ would cause a Zeeman shift that correlated with the direction of $\mathbf{E}$, which mimics an EDM energy shift. Second, the same motional magnetic field tilts the quantisation axis of the atoms in the electric field, which causes a geometric phase to be accumulated if magnetic field gradients are present. This phase depends on the sign of the electric field relative to the magnetic field, and so also mimcs an EDM phase. Third, a magnetic field that correlates with $\mathbf{E}$ could be generated by leakage and charging currents when switching the direction of $\mathbf{E}$. This also leads to a false EDM signal.

1.2.2. Paramagnetic molecules

Paramagnetic and polar molecules offer two distinct advantages over atoms for measuring d_e. First, these molecules are much more polarisable than atoms, and therefore have larger enhancement factors than atoms. Second, molecules offer better suppression and rejection of systematic effects than atoms.

It can be seen from Eq. (1.6) that the EDM energy shift, ΔE_edm, can be large if the spacing between states of opposite parities, $E_0 - E_n$, is small. In atoms, typically it

Table 1.3.: Effective electric fields for some polar molecules.

Molecular species	E_{eff} (GV cm^{-1})
YbF	-26 [49]
BaF	7.4 [50]
PbO	25 [51]
ThO	-80 [52]
HfF$^+$	23 [53, 54]
ThF$^+$	35 [55]
YbOH	-23 [56]

is the valence s and p states that are mixed, which have separations on the order of 10^{14} Hz. As a result, atoms are only weakly polarised in an external field, which is evident from the linear dependence of ΔE_{edm} on E_{ext} in Eq. (1.7). In polar molecules, rotational levels that are adjacent have opposite parities and these have a typical energy spacing of 10^{10}–10^{11} Hz. Polar molecules are therefore much more strongly polarised by external fields, resulting in greater enhancement of the eEDM. This was first pointed out by Sushkov and Flambaum [47], though Sandars had earlier considered a similar effect to investigate the proton EDM in the TlF molecule [48]. In this regime of strong polarisation, the perturbative description in Eq. (1.6) is no longer appropriate. One description is to consider the valence electron in the polar molecule interacting with an effective electric field E_{eff} inside the molecule, which by symmetry must be directed along the internuclear axis, $\hat{\mathbf{n}}$ [48]. In the absence of an external field to align the molecule, this interaction averages to zero. The role of the external field is then to polarise the molecule so that we can leverage the large effective field provided by the molecule itself, which has typical magnitudes of 10–100 GV cm^{-1}. The calculated values for E_{eff} for some polar molecules are shown in Table 1.3. The EDM energy shift for polar molecules can then be written as

$$\Delta E_{\text{edm}} = -\eta(E_{\text{ext}}) d_e E_{\text{eff}}, \tag{1.9}$$

where the polarisation factor $\eta(E_{\text{ext}}) = \langle \hat{\mathbf{n}} \cdot \hat{\mathbf{z}} \rangle$ quantifies how aligned the molecule is to the direction of the external field (defined to be along $\hat{\mathbf{z}}$).

So far, only four paramagnetic molecules – YbF, PbO, ThO and HfF$^+$ – have been used to set limits on the eEDM. The best results from each experiment are given in Table 1.4. The YbF molecule was the first paramagnetic molecule used to measure the eEDM, using its ground X$^2\Sigma^+$ state [60]. The strong tensor polarisability of the ground state

Table 1.4.: Experimental limits (90% confidence level) on d_e set by some paramagnetic molecules, assuming that the eEDM is the sole contribution to the molecular EDM.

Molecular species	Upper bound on d_e (e cm)
YbF	1.06×10^{-27} [57]
PbO	1.7×10^{-26} [58]
HfF$^+$	1.3×10^{-28} [59]
ThO	1.1×10^{-29} [25]

of YbF effectively "pins" the internuclear axis of the molecule to the electric field [61], making the molecule insensitive to magnetic fields perpendicular to the direction of the electric field. This greatly reduces the effect of the motional magnetic field and the geometric phase [60], which had limited the Tl experiment. Control of leakage currents is also made easier since only relatively modest fields are required to achieve high enhancement factors. For example, the electric field strength in the YbF experiment was 10 kV cm^{-1} [62] (which gives $\eta = 0.558$) whereas that of the Tl experiment was 123 kV cm^{-1} [44]. In 2011, the precision of atomic measurements was surpassed by polar molecules for the first time as the Imperial group used YbF molecules to set an upper bound[6] of $|d_e| < 1.06 \times 10^{-27}\, e$ cm [57]. Future experiments are likely to yield much better sensitivities through longer coherence times τ as YbF has an electronic structure that is amenable to laser cooling and the eEDM-sensitive state is the ground state and so has an infinite lifetime.

In 2013, the Yale group published a measurement of the eEDM using PbO molecules in the paramagnetic $a^3\Sigma^+$ state, which reported a limit of $|d_e| < 1.7 \times 10^{-26}\, e$ cm [58]. The experiment was conducted in a high-temperature vapour cell, rather than in a beam-type configuration. Although it set a weaker limit than the YbF experiment, this experiment demonstrated the advantages of using a state with an Ω-doublet structure for an eEDM measurement, where Ω refers to the projection of electronic angular momentum ($\mathbf{J}_e$) on the internuclear axis ($\hat{\mathbf{n}}$). Such a doublet occurs in molecular states with $\Omega \neq 0$, as there are two possible projections of $\mathbf{J}_e$ onto $\hat{\mathbf{n}}$: $\Omega = \pm|\Omega|$. In the absence of an external field, the eigenstates are symmetric or antisymmetric combinations of $|\Omega\rangle$ and $|-\Omega\rangle$ and are defined by their parity, P, as shown in the top of Fig. 1.6. The "parity-doublet" has a small splitting Δ_Ω due to a coupling between $\mathbf{J}_e$ and the total angular momentum $\mathbf{J} = \mathbf{J}_e + \mathbf{N}$, where $\mathbf{N}$ is the rotational angular momentum. This splitting can be very

---

[6] All eEDM limits quoted here are at the 90% confidence level.

small compared to the splitting between the rotational levels: for PbO $\Delta_\Omega = 11.2\,\mathrm{MHz}$ compared to the rotational constant of $B_r \approx 7\,\mathrm{GHz}$ [63]. This has two consequences that are advantageous for an eEDM measurement. First, full polarisation of the molecule ($|\eta| = 1$) is easily achieved with low electric fields, $|\mathbf{E}_\mathrm{ext}| \geq 15\,\mathrm{V\,cm^{-1}}$ [63], allowing the experiment to leverage the large effective field of the molecule and be independent of the magnitude of $\mathbf{E}_\mathrm{ext}$. Second, the fully-polarised molecule can be in one of two states, $\eta = \pm 1$, indicating the molecule pointing along or against the direction of the applied field, as shown in the bottom of Fig. 1.6. These states have approximately the same magnetic g-factor[7], but the opposite sign for E_eff, so by taking differences between measurements in the two states one can protect against systematic effects due to unwanted magnetic fields [58]. This property of having an "internal co-magnetometer" due to the Ω-doublet structure of the EDM-sensitive state helped reduce the systematic error due to leakage currents in this experiment by a factor of 100 [58].

In 2014, using a beam of ThO molecules in the paramagnetic $\mathrm{H}^3\Delta_1$ state, the ACME collaboration pushed the eEDM limit down to $|d_e| < 8.7 \times 10^{-29}\,e\,\mathrm{cm}$ [65]. The ThO molecule has an effective field of $80\,\mathrm{GV\,cm^{-1}}$ [52], which is 3 times as large as that of YbF or PbO. Just like the PbO experiment, the $^3\Delta_1$ state has an Ω-doublet structure ($\Delta_\Omega \approx 360\,\mathrm{kHz}$ [66, appendix D]) and the advantages associated with such a structure. The $^3\Delta_1$ state has the added benefit of having a very small magnetic g-factor[8], $g \approx -0.0044$ [67], which further suppresses the effect of any systematics related to magnetic fields. In 2018, the second-generation ThO experiment improved the eEDM limit to $|d_e| < 1.1 \times 10^{-29}\,e\,\mathrm{cm}$ [25], where the increase in sensitivity came primarily from increasing the number of molecules detected in this experiment. This was done by improving the state preparation through a carefully-designed rotational cooling and STIRAP[9] scheme [68], as well as increasing the detected solid angle of the molecules and detection efficiency [25]. This last result is the current experimental limit on d_e.

---

[7] In PbO, the difference in the g-factors of the $\eta = \pm 1$ states depends on the applied electric field magnitude E_ext: $\Delta g_\pm \approx \frac{\Delta_\Omega}{\mu_\mathrm{mol} E_\mathrm{ext}} \Delta g_0 \pm \frac{3\mu_\mathrm{mol} E_\mathrm{ext}}{20 B_r} \bar{g}$, where $\Delta g_0 \approx 0.0003$ and $\bar{g} \approx 0.86$ are the difference and average of the g-factors of the parity states, Δ_Ω is the Ω-doublet splitting and μ_mol is the molecular dipole moment [64]. The first term is suppressed at high fields, and the second changes sign between opposite η states and so averages to zero.

[8] This arises because the $^3\Delta_1$ state has the effective g-factor $g = g_L \Lambda + g_S \Sigma \approx 0$ since $g_L = 1$, $g_S = 2$, and for this state the projection of orbital and spin angular momenta onto the internuclear axis are $\Lambda = 2$ and $\Sigma = -1$. The dominant contribution to $g \neq 0$ comes from spin-orbit coupling of the H state to other electronic states [67].

[9] STIRAP stands for Stimulated Raman Adiabatic Passage.

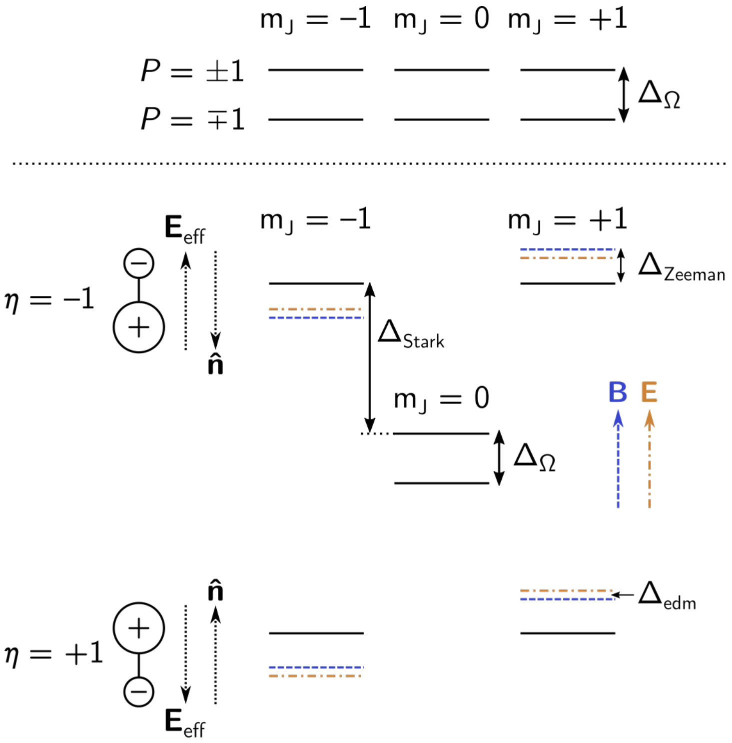

Figure 1.6.: An example of a $J = 1$ Ω-doublet structure in the absence (top) and presence (bottom) of electric and magnetic fields. Δ_{Stark} is the tensor Stark shift in an electric field, Δ_{Zeeman} is the magnetic Zeeman shift and Δ_{edm} is the shift due to the EDM interaction in the molecule, $d_e E_{\mathrm{eff}}$.

Finally, a group at JILA carried out an eEDM measurement using trapped HfF$^+$ molecular ions, and in 2017 they reported the limit $|d_e| < 1.3 \times 10^{-28}$ e cm [59]. This was the first such measurement using trapped molecular ions. The experiment was carried out in an rf ion trap, and instead of the usual uniform electric field found in EDM experiments, a rotating bias electric field was applied which caused the ions to undergo additional circular micromotion in the trap [69]. This electric field polarises the HfF$^+$ ions and defines the quantisation axis, so it can be viewed as the “uniform” electric field in the molecule’s frame of reference. A uniform magnetic field in the rotating frame is produced by generating a static magnetic field gradient in the laboratory frame with a pair of anti-Helmholtz coils [69]. HfF$^+$ has a similar $^3\Delta_1$ state to ThO, with $\Delta_\Omega \approx 700\,\mathrm{kHz}$ [70]. The experiment allows long coherence times of $\tau > 700\,\mathrm{ms}$ although at the expense of fewer molecules, especially when compared to beam-type experiments.

1.2.3. Future eEDM experiments

This thesis describes an improvement in the statistical sensitivity of the YbF experiment through better state preparation and detection, which was reported recently in [71]. The demonstrated sensitivity is close to the shot-noise limit, and investigation of potential systematic effects is ongoing. The HfF^+ experiment at JILA has also shown an improvement of almost a factor of 50 in statistical sensitivity by developing a new state detection method that can distinguish between two different oriented states. This development helped them overcome technical noise and reach the quantum projection noise (QPN) limit, which allowed them to leverage the long coherence times of 1.5 s and relatively large number of trapped molecular ions [72]. The ACME collaboration has reported the characterisation of a $\mathrm{Q}^3\Delta_2$ state in the ThO molecule, which can be used for electrostatic lensing and co-magnetometry due to its large Stark shift and magnetic moment [73]. This can be used to increase the number of useful molecules in the experiment and improve their characterisation of systematic effects due to magnetic field gradients. The last two experiments are likely to be eventually limited by the eEDM-sensitive state lifetime, which is 2.1 s for HfF^+ [74] and $\sim 2\,\mathrm{ms}$ for ThO [75].

Elsewhere, efforts are underway to incorporate laser cooling and trapping into eEDM experiments. Laser cooling can significantly increase the number of atoms or molecules in the experiment and improve coherence times, leading to better sensitivities. At Pennsylvania State University, Cs atoms are laser-cooled in a magneto-optical trap (MOT) before being loaded into an optical lattice and subsequently launched into a region of uniform electric and magnetic fields, where the EDM measurement is performed [76]. An experiment to measure the EDM of laser-cooled Fr atoms is underway in Tohoku University [77], where Fr was chosen for its large enhancement factor of 895 (see Table 1.1). The NL-eEDM collaboration and the Imperial group are planning to measure the eEDM with a laser-cooled beam of BaF [78] and YbF [79], respectively. The Imperial group has already demonstrated successful transverse cooling of YbF molecules [80] from a cryogenic buffer-gas-cooled source, and are planning to carry out a future experiment with much longer coherence times with these laser-cooled molecules. The PolyEDM collaboration has also achieved transverse laser cooling of YbOH molecules [81]. The YbOH molecule is a promising candidate for eEDM searches as it is both amenable to laser cooling and has low-lying "bending" vibrational modes which are long-lived and are similar to the Ω-doublet structures of HfF^+ and ThO [82].

Finally, a method to measure the EDM of polar molecules trapped in an inert-gas matrix has been proposed by Vutha, Horbatsch and Hessels [83]. The main benefit of the proposed technique is a large increase in the number of molecules in the experiment, while maintaining second-long coherence times. This technique also has potentially strong systematic error rejection by embedding a molecule that is less sensitive to the eEDM in the same matrix [83].

1.3. This thesis

The last published measurement of the eEDM from the YbF experiment was in 2011 [57]. Since then, various upgrades were carried out and the details of these are in [84–86]. The most important of these are the new state preparation and state detection schemes, proposed by J. Devlin [85] and implemented together with I. Rabey [86]. These schemes increased the number of molecules participating in the experiment and their detection efficiency. An overview of the YbF energy levels and these schemes are given in Chapter 2.

I joined the experiment in June 2016, while the detection method was being tested. I helped to implement the detection methods and I later developed techniques to maximise the interferometer contrast with the new detection scheme. Furthermore, I helped install new optical atomic magnetometers in order to better characterise the ambient magnetic field of the experiment. These details, together with a comprehensive look at all the other experimental methods, are presented in Chapter 3. After improving the theoretical shot-noise limit of the experiment, I helped reduce various sources of noise in the experiment to below this limit and achieved an experimental eEDM sensitivity close to this limit. I also modified the data acquisition and analysis procedure to incorporate the new detection methods. This is the subject of Chapter 4. After achieving this, we are now in the process of characterising potential systematic effects in the experiment. I conclude this thesis in Chapter 5 by first discussing the main systematics that we are currently investigating, and then presenting an outlook for a full EDM measurement. Finally, I discuss a next-generation experiment that will use a source of buffer-gas-cooled and laser-cooled YbF molecules to make an eEDM measurement with an order-of-magnitude improvement in sensitivity.

2. Experiment overview

This chapter gives an overview of the YbF EDM experiment at Imperial College London. First, I introduce the molecular structure of YbF and highlight the relevant states and transitions for the experiment. I then give an overview of the eEDM measurement sequence. Finally, I derive the shot-noise limit for the statistical sensitivity of the experiment.

2.1. Molecular structure of YbF

To describe the energy levels of a diatomic molecule, the first step is to use the Born-Oppenheimer approximation to separate nuclear motion from electronic motion. This is justified as follows: since the electron is much lighter than the nucleus, the electrons move much more quickly than the nuclei and so the electrons are able to adiabatically follow the slowly-changing positions of the nuclei.

2.1.1. Electronic states

The largest contribution to the electronic state energy is the electrostatic Coloumb interaction between the electrons and the nuclei. In atoms, the quantum numbers used to describe electronic states are the principal quantum number n, the orbital angular momentum L, the magnetic quantum number m_L which is the z-component of the orbital angular momentum, and the spin angular momentum S. In diatomic molecules, there is a strong internal electric field along the internuclear axis $\hat{\mathbf{n}}$. The electronic orbital

Table 2.1.: Angular momentum operators and quantum numbers used in this thesis and their descriptions. The subscript z' here indicates the component along the internuclear axis.

Operator	Quantum number	Description
$\mathbf{L}$	L	Electronic orbital angular momentum
$\mathbf{S}$	S	Electronic spin angular momentum
$\mathbf{R}$	R	Rotational angular momentum
$\mathbf{I}$	I	Nuclear spin angular momentum
$\mathbf{J} = \mathbf{L} + \mathbf{S} + \mathbf{R}$	J	Total angular momentum without nuclear spin
$\mathbf{N} = \mathbf{J} - \mathbf{S}$	N	Total angular momentum without electronic or nuclear spin
$\mathbf{G} = \mathbf{S} + \mathbf{I}$	G	Total spin (electronic and nuclear)
$\mathbf{F} = \mathbf{J} + \mathbf{I}$	F	Total angular momentum
$L_{z'}$	Λ	Component of **L** along internuclear axis
$S_{z'}$	Σ	Component of **S** along internuclear axis
$J_{z'}$	Ω	Component of **J** along internuclear axis

angular momentum vector $\mathbf{L}$ is strongly coupled to this field and precesses rapidly around it, thus L is not well-defined and therefore no longer a good quantum number. However, the component of $\mathbf{L}$ along the internuclear axis, Λ, is still a good quantum number. For a state with orbital angular momentum L, Λ can take on values $0, \pm 1, \pm 2, \ldots, \pm L$, which by convention is denoted as a $\Sigma, \Pi, \Delta, \ldots$ state. States with $\Lambda \neq 0$ have two components $\pm\Lambda$ which are degenerate, although spin-orbit and rotational couplings with nearby electronic states can lift this degeneracy (Λ-doubling). These $\Lambda \neq 0$ states also generate an internal magnetic field along $\hat{\mathbf{n}}$, which the magnetic moment of the electrons (arising from their spin) can couple to. This is known as spin-orbit coupling, and for sufficiently strong coupling strengths the spin vector $\mathbf{S}$ precesses around $\hat{\mathbf{n}}$ as well. In this case, we define the component of $\mathbf{S}$ along $\hat{\mathbf{n}}$ as Σ, which can take on values $-S, -S+1, \ldots, S-1, S$. The spin multiplicity is therefore $2S+1$. The total electronic angular momentum along the internuclear axis is then defined as $\Omega = \Lambda + \Sigma$. A summary of symbols used in this thesis to describe various angular momenta[1] is given in Table 2.1. The electronic state of a diatomic molecule in a $\Lambda \neq 0$ state is written as ${}^{2S+1}\Lambda_{\Omega}$.

For a $\Lambda = 0$ state, there is no spin-orbit coupling, which means that $\mathbf{S}$ is not coupled to $\hat{\mathbf{n}}$. Thus, Σ and Ω are not well-defined. These states are labelled as ${}^{2S+1}\Lambda^{+/-}$, where the

---

[1] Note that Σ is both the symbol for a state with $\Lambda = 0$ and the quantum number for the operator $S_{z'}$; its meaning should be clear from the context in which it is used.

Table 2.2.: Measured values of molecular parameters for the ground $X^2\Sigma^+$ state and first excited $A^2\Pi_{1/2}$ state of ^{174}YbF, all from [89] unless stated.

Parameter (units)	Value for $X^2\Sigma^+$ state	Value for $A^2\Pi_{1/2}$ state
E_0 (THz)	0	542.8102(1)
A (THz)	-	40.9304(1)
ω_e (THz)	15.1895(2)	-
$\omega_e x_e$ (GHz)	67.3(1)	-
$B(v=0)$ (GHz)	7.23377(2) [90]	7.4276(4)
α_e (MHz)	46.5(4)	-
$D(v=0)$ (kHz)	7.16(12)	7.35(12)

superscript $+/-$ refers to the symmetry of the electronic wavefunction upon reflection about an arbitrary plane containing the internuclear axis. The electronic energy of a state is then given by

$$E_{\mathrm{el}} \approx E_0 + A\Lambda\Sigma, \tag{2.1}$$

where E_0 is the electrostatic energy relative to the ground state and A parametrises the spin-orbit coupling term in the molecular Hamiltonian, $A\mathbf{L}\cdot\mathbf{S}$. For the YbF molecule, the measured values for E_0 and A are given in Table 2.2 alongside other parameters which we will introduce later.

The Yb atom has the ground-state electronic configuration $[\mathrm{Xe}]4f^{14}6s^2$, whereas that of the F atom is $[\mathrm{He}]2s^2 2p^5$. In the YbF molecule, one $6s$ electron is donated to the $2p$ orbital of fluorine, leaving a valence electron that in the molecular ground state has mostly Yb $6s\sigma$ character [87]. This ground state is labelled $X^2\Sigma^+$. There is no spin-orbit coupling in this state since it is a Σ state. In the first excited state of YbF, labelled $A^2\Pi$, the valence electron is of approximately $6p\pi$ character [88]. This state has strong spin-orbit coupling, as shown in Table 2.2, which splits the state into $\Omega = 1/2$ and $\Omega = 3/2$ components. These components are sufficiently distinct that it is common to treat them as separate electronic levels $A_1^2\Pi_{1/2}$ and $A_2^2\Pi_{3/2}$, and in this thesis we will only be concerned with the former (which lies closest in energy to the X state), and will refer to this as the A state.

2.1.2. Nuclear motion — vibration and rotation

Turning to the nuclear motion, we find that it can be separated into vibrational and rotational parts. The vibration of a diatomic molecule can be thought of as a stretching along its internuclear axis, or equivalently an oscillation of the bond length around the equilibrium distance between the two nuclei. To lowest order, this can be approximated as a harmonic oscillator. We can therefore write the energies of the vibrational levels as

$$E_{\text{vib}}(v) = \omega_e(v + 1/2), \tag{2.2}$$

where the frequency ω_e depends on the electronic state of the molecule and v is the vibrational quantum number. The rotational motion of the molecule can be approximated as a rigid rotor, where the two nuclei rotate about their centre of mass at a fixed distance from each other. The energies of the rigid rotor are

$$E_{\text{rot}}(R) = BR(R + 1), \tag{2.3}$$

where the rotational constant B is related to the moment of inertia of the rotor I by $B = h^2/(8\pi^2 I)$, and R is the rotational quantum number. Higher-order corrections to the above energies can be obtained via a more rigorous analysis of the vibrational and rotational motion [91, § 6.8], leading to the expressions

$$\begin{aligned} E_{\text{vib}}(v) &= \omega_e(v + 1/2) - \omega_e x_e(v + 1/2)^2 + \cdots , \\ E_{\text{rot}}(v, R) &= B(v)R(R + 1) - D(v)R^2(R + 1)^2 + \cdots , \end{aligned} \tag{2.4}$$

where

$$\begin{aligned} B(v) &= B_e - \alpha_e(v + 1/2) + \cdots , \\ D(v) &= D_e + \beta_e(v + 1/2) + \cdots . \end{aligned} \tag{2.5}$$

The term parametrised by x_e represents a first-order correction due to anharmonicity in the vibration potential. The term $B(v)$ is the same rotational constant as B in Eq. (2.3), but with corrections due to the vibrational motion, and the subscript e explicitly shows the dependence on the electronic state. Finally, the term with $D(v)$ represents the first-order correction due to the stretching of the bond from the rotational motion and is usually referred to as the centrifugal distortion term. Dunfield *et al.* [89] measured these parameters for the X and A states of ^{174}YbF; their results are reproduced in Table 2.2.

The vibrational constants were not determined for the A state as its $v = 1$ level is strongly perturbed by a nearby $\Omega = 1/2$ state labelled as 18.6[0.5] [88, 89].

The gross-structure energies of a diatomic molecule can therefore be written as

$$\begin{aligned} E &= E_{\mathrm{el}} + E_{\mathrm{vib}} + E_{\mathrm{rot}} \\ &\approx E_0 + A\Lambda\Sigma + \omega_e(v + 1/2) + BR(R+1). \end{aligned} \tag{2.6}$$

From the measured values of the parameters given in Table 2.2, we see that $E_{\mathrm{el}} \gg E_{\mathrm{vib}} \gg E_{\mathrm{rot}}$, so the molecular structure of YbF can be described first by an electronic state, which splits into different vibrational states $v = 0, 1, \ldots$, and within each vibrational manifold we get a further splitting into rotational states $R = 0, 1, \ldots$. The structure of the rotational levels is dependent on the couplings between the electronic, rotational and nuclear degrees of freedom, which are sometimes referred to as rotational perturbations [92]. In this experiment, we are only concerned with the three lowest rotational states of the ($\mathrm{X}^2\Sigma^+$, $v = 0$) manifold, and the lowest rotational state of the ($\mathrm{A}^2\Pi_{1/2}$, $v = 0$) manifold. We will now describe these states in more detail.

2.1.3. Rotational and hyperfine couplings

As mentioned above, rotational couplings involve interactions between the rotational motion of the molecule, described by $\mathbf{R}$, and either the nuclear or electronic angular momenta. The hyperfine interaction describes the coupling of nuclear spin $\mathbf{I}$ to the electronic angular momenta $\mathbf{L}$ and $\mathbf{S}$. The form of these interactions depends on the electronic state, and so we will discuss these separately for the X and A states.

$\mathbf{X^2\Sigma^+}$ ground state

There is no orbital angular momentum in this state, $\mathbf{L} = 0$, so the spin-orbit coupling vanishes. This state is therefore best described by Hund's case (b) [91], where $\mathbf{S}$ is not coupled to $\hat{\mathbf{n}}$. The total angular momentum without spin is $\mathbf{N} = \mathbf{J} - \mathbf{S} = \mathbf{R}$, so $\mathbf{N}$ and $\mathbf{R}$ are interchangeable in this state. We can write down the effective Hamiltonian that

Table 2.3.: Spin-rotation and hyperfine parameters for the ground $X^2\Sigma^+$ state of ^{174}YbF, all from [90]. Note here that b_0 and b_1 parametrise the centrifugal distortion of b: $b = b_0 + b_1 N(N+1)$.

Parameter (units)	Value
γ_0 (MHz)	-13.42400(16)
γ_1 (kHz)	3.9823(11)
γ_2 (mHz)	-25(1)
b_0 (MHz)	141.7956(5)
b_1 (kHz)	-0.510
c (MHz)	85.4026(14)
C (kHz)	20.38(13)

includes molecule rotation, spin-rotation coupling and hyperfine interactions [90, 93]:

$$\mathcal{H} = B\mathbf{N}^2 + \gamma\mathbf{S}\cdot\mathbf{N} + b\mathbf{I}\cdot\mathbf{S} + cI_{z'}S_{z'} + C\mathbf{I}\cdot\mathbf{N}. \tag{2.7}$$

The first term describes molecule rotation, $\mathcal{H}_{\text{rot}} = B\mathbf{R}^2 = B\mathbf{N}^2$, so N is the rotational quantum number. The next term describes the spin-rotation coupling with parameter γ, and we note here that γ displays a strong dependence on rotation in this state and can be parametrised as [90, 94]

$$\gamma = \gamma_0 + \gamma_1 N(N+1) + \gamma_2 N^2(N+1)^2 + \cdots\,. \tag{2.8}$$

The last three terms in Eq. (2.7) describe the hyperfine interaction of the electron spin $\mathbf{S}$ and molecule rotation $\mathbf{N}$ with nuclear spin $\mathbf{I}$, where b, c and C are hyperfine parameters and z' refers to the z-axis in the molecule frame, i.e. the internuclear axis. These parameters were measured in [90] and are reproduced here in Table 2.3.

We will be using the first three rotational states for the experiment, $N = 0, 1, 2$, and in these low-N states the hyperfine interaction is stronger than the spin-rotation coupling. Therefore, the states are well described by a basis which couples first the electron and nuclear spins, $\mathbf{G} = \mathbf{I}+\mathbf{S}$, and then couples the spin and rotation angular momenta to give the total angular momentum $\mathbf{F} = \mathbf{G}+\mathbf{N}$, which is also known as Hund's case ($\mathrm{b}_{\beta S}$) [95]. The ^{174}Yb isotope has zero nuclear spin while ^{19}F has a spin of 1/2, so $I = 1/2$ which means $G = 0, 1$. The $N = 0$ rotational level is therefore split into hyperfine components $F = 0, 1$, whereas $N \neq 0$ levels are split into $F = N+1, N_{\mathrm{h}}, N_{\ell}, N-1$ levels, where we use the notation N_{h} and N_{ℓ} to refer to the higher-lying and lower-lying $F = N$ states,

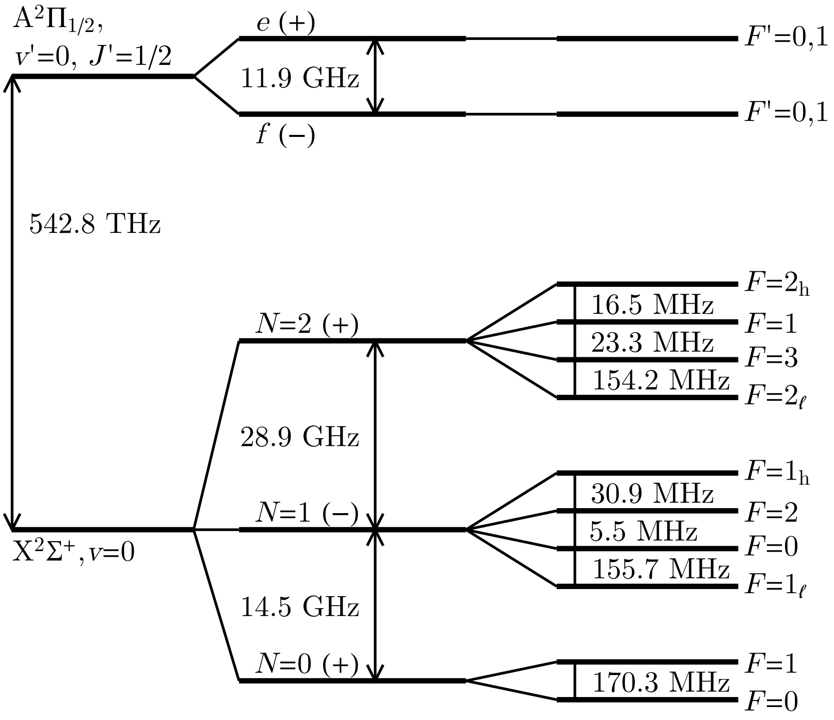

Figure 2.1.: Energy level diagram of the states used in the experiment. The energy separations were measured by Sauer *et al.* [90].

respectively. Each hyperfine level has a $(2F+1)$-fold degeneracy, which is lifted by an external magnetic field via the Zeeman interaction. Fig. 2.1 shows the hyperfine and rotational splittings in the $N = 0, 1, 2$ levels of the ground state. The states that we use to measure the eEDM are the $m_F = \pm 1$ components of the $F = 1$ hyperfine level in the $(\mathrm{X}^2\Sigma^+, v = 0, N = 0)$ manifold.

$\mathrm{A}^2\Pi_{1/2}$ excited state

We will use primed quantum numbers in the $\mathrm{A}^2\Pi_{1/2}$ state to distinguish them from quantum numbers in the ground state. The spin-orbit coupling in the $\mathrm{A}^2\Pi_{1/2}$ state is sufficiently large that the state is best described by Hund's case (c) [88]. In this case, **L** is no longer tightly coupled to the internuclear axis by electrostatic forces and thus Λ' is not well-defined. Instead, the electronic angular momenta **L** and **S** are combined with the rotational angular momentum **R** to give the total angular momentum excluding nuclear spin: $\mathbf{J} = \mathbf{L} + \mathbf{S} + \mathbf{R}$. The component of **J** along the internuclear axis, $J_{z'}$, has two quantum numbers $\Omega' = \pm 1/2$ which correspond to $J_{z'}$ pointing along or against the internuclear axis. However, these are not eigenstates of parity as the parity operation transforms the $\Omega' = 1/2$ state into the $\Omega' = -1/2$ state and vice versa[2]. We can, however, construct eigenstates by taking symmetric and antisymmetric combinations of these states:

$$\begin{aligned} |e\rangle &= \frac{1}{\sqrt{2}}\left(|\Omega' = 1/2\rangle + |\Omega' = -1/2\rangle\right), \\ |f\rangle &= \frac{1}{\sqrt{2}}\left(|\Omega' = 1/2\rangle - |\Omega' = -1/2\rangle\right). \end{aligned} \tag{2.9}$$

The e and f states have well-defined parities of $\pm(-1)^{J-1/2}$ respectively. The degeneracy of these states is lifted by terms in the rotational Hamiltonian and spin-orbit interaction that have off-diagonal matrix elements between the $\mathrm{A}^2\Pi_{1/2}$ state and the higher-lying $\mathrm{B}^2\Sigma^+$ state. This can be seen by considering the rotational Hamiltonian:

$$\begin{aligned} \mathcal{H}_{\text{rot}} &= B\mathbf{R}^2 \\ &= B(\mathbf{J} - \mathbf{L} - \mathbf{S})^2 \\ &= B[(\mathbf{J}^2 - J_{z'}^2) + (\mathbf{L}^2 - L_{z'}^2) + (\mathbf{S}^2 - S_{z'}^2) \\ &\quad + (L_+S_- + L_-S_+) - (J_+L_- + J_-L_+) - (J_+S_- + J_-S_+)]. \end{aligned} \tag{2.10}$$

The first term is the effective rotational Hamiltonian $B\mathbf{J}^2$ which gives the rotational energy spectrum $BJ'(J'+1)$. The terms $\mathbf{L}^2$, $L_{z'}^2$, $J_{z'}^2$, $\mathbf{S}^2$ and $S_{z'}^2$ give a constant energy offset. All the terms involving ladder operators can be treated as perturbations as these only have non-zero off-diagonal matrix elements with other electronic levels. It turns out that these matrix elements are slightly different for the e and f states, therefore resulting in different perturbative shifts in energy and a splitting to occur between the two states. This is called Ω-doubling and the magnitude of the splitting is $\Delta_\Omega \approx p(J' + 1/2)$ for a perturbation of $^2\Pi_{1/2}$ levels by a $^2\Sigma^+$ state [92, § 2.5.4]. For the lowest rotational state in the A state of ^{174}YbF, $J' = 1/2$, the Ω-doubling splitting has been measured to be $p = 11.8\,\text{GHz}$ [89].

The e and f states in $J' = 1/2$ are then further split by the hyperfine interaction into states $F' = 0, 1$, where $\mathbf{F} = \mathbf{J} + \mathbf{I}$. The form of the hyperfine interaction in this $^2\Pi$ state is more complicated than the ground state because of the non-zero Λ and Ω-doubling,

---

[2] We should be careful in stating what the parity operation means here: it is the reflection through a plane containing the internuclear axis. This reverses the coordinates of all the electrons but not the nuclei, so Ω' is reversed with respect to the internuclear axis.

so we will not go into its details here, but it has been considered in [88] and [93]. The hyperfine splitting in the $J' = 1/2$ state has been measured to be very small, on the order of a few MHz [88] and smaller than the natural linewidth of the excited state, which is 5.7 MHz [96]. Therefore, we treat these levels as degenerate in Fig. 2.1.

2.1.4. Interactions with external fields

To measure the eEDM, the YbF molecules are placed in a region of uniform electric and magnetic fields. We now discuss the Stark, Zeeman and EDM interactions that arise due to these fields, with particular attention paid to states in the $(\mathrm{X}^2\Sigma^+, v = 0, N = 0)$ manifold.

Stark interaction

In the presence of an electric field $\mathbf{E}$, the Hamiltonian for the Stark interaction is $\mathcal{H}_\mathrm{s} = -\boldsymbol{\mu} \cdot \mathbf{E}$, where $\boldsymbol{\mu}$ is the dipole moment operator. The dipole moment of the $\mathrm{X}^2\Sigma^+$ state is 1.97 MHz/(V/cm) [88]. Let us consider the effect of the Stark interaction on the rotational levels of the ground state. The effective Hamiltonian can be written as

$$\begin{aligned} \mathcal{H} &= \mathcal{H}_\mathrm{rot} + \mathcal{H}_\mathrm{s} + \mathcal{H}_\mathrm{hfs} \\ &= B\mathbf{N}^2 - \boldsymbol{\mu} \cdot \mathbf{E} + \gamma \mathbf{S} \cdot \mathbf{N} + b\mathbf{I} \cdot \mathbf{S} + cI_{z'}S_{z'} + C\mathbf{I} \cdot \mathbf{N}. \end{aligned} \tag{2.11}$$

The Stark Hamiltonian has non-zero matrix elements connecting rotational states with $\Delta N = \pm 1$, $\Delta m_N = 0$. The rotational levels are therefore strongly mixed by the electric field, resulting in a large Stark shift of these levels as shown in Fig. 2.2. For the electric fields we are considering, the levels initially labelled by N do not cross so we can still use N and m_N to label these Stark-shifted levels, although N is no longer a good quantum number.

Within each rotational manifold, the hyperfine levels are also shifted differently due to the so-called tensor Stark interaction. When the electric field is absent, the tensor part of the hyperfine interaction mixes levels with the same F but different N, where $\Delta N = \pm 2$. Since the rotational energy is much larger than the hyperfine energies, this mixing term is very small, which results in a small F-dependent, but m_F-independent

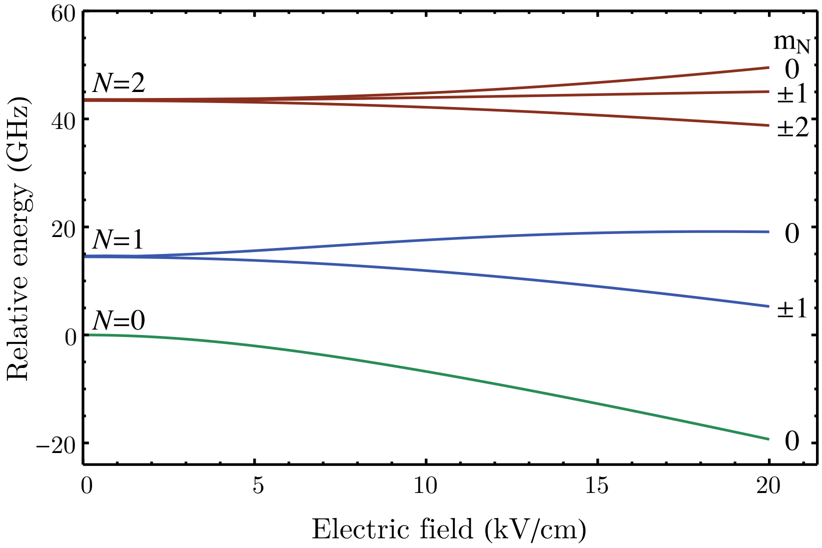

Figure 2.2.: Stark shift of the rotational levels in the $X^2\Sigma^+$ state.

shift of the hyperfine levels. When the electric field is present, rotational levels with the same $|m_N|$ but different N are strongly mixed together, which now causes the effect of the tensor hyperfine mixing to become much larger. Moreover, since the rotational mixing is dependent on $|m_N|$ (see Fig. 2.2), the shift in energies of the hyperfine levels now depends on $|m_F|$. In the $N = 0$ ground rotational state, this causes the hyperfine splitting Δ_{hyp} between the $F = 0$ and $F = 1$ levels to change with the applied electric field. Additionally, it causes a tensor Stark shift Δ_{S} between the $|1, 0\rangle$ and $|1, \pm 1\rangle$ Zeeman sublevels. These effects are shown in Fig. 2.3.

We can use the Hamiltonian in Eq. (2.11) to calculate the polarisation factor, which we introduced in Section 1.2.2. Recall that it was given by $\eta = \langle \hat{\mathbf{n}} \cdot \hat{\mathbf{z}} \rangle = \langle \cos\theta \rangle$, where θ is the angle between the internuclear axis and the z-axis. Here we let the electric field point along the z-axis. Since $\boldsymbol{\mu} \cdot \mathbf{E} = \mu E \cos\theta$, we can easily calculate η by taking the derivative of the energy of the relevant state with respect to E:

$$\begin{aligned} \frac{d\langle\mathcal{H}\rangle}{dE} &\approx \langle\frac{d\mathcal{H}}{dE}\rangle = -\mu\langle\cos\theta\rangle = -\mu\eta \\ \implies \eta(E) &= -\frac{1}{\mu}\frac{d\langle\mathcal{H}\rangle}{dE}, \end{aligned} \tag{2.12}$$

where in the first step I have neglected extra terms due to the change in the wavefunction with E. Figure 2.4 shows the dependence of η on the applied electric field. We usually

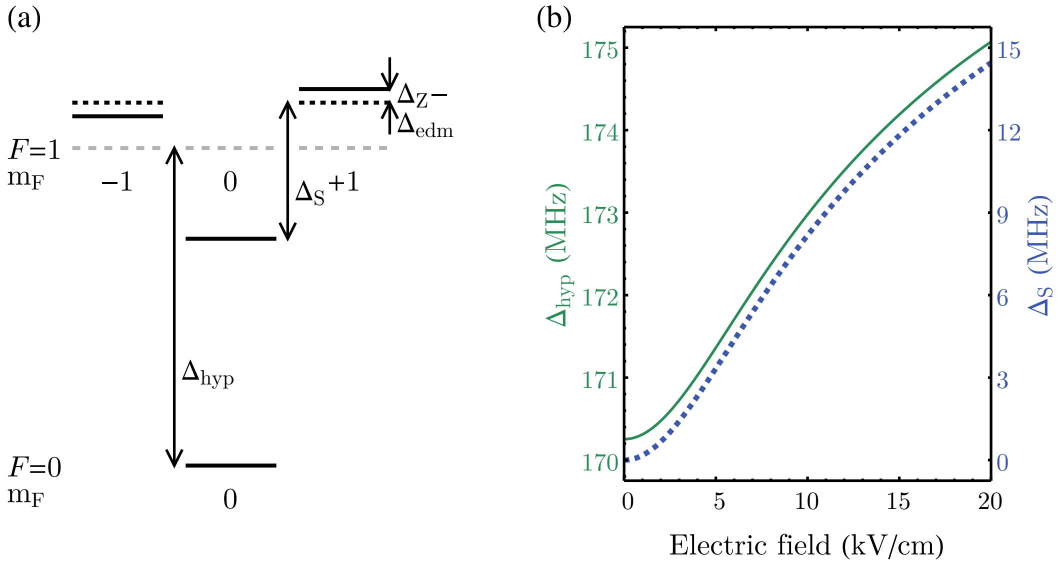

Figure 2.3.: (a) The hyperfine levels of $N = 0$ in the ground electronic and vibrational manifold. The grey dashed lines represent the $F = 1$ levels without any fields present. The tensor Stark effect causes a splitting of Δ_S between the $|1, 0\rangle$ and $|1, \pm1\rangle$ sublevels and a change in the hyperfine splitting Δ_{hyp} between $|0, 0\rangle$ and $|1, \pm1\rangle$. The Zeeman and EDM interactions cause a splitting of $2(\Delta_Z - \Delta_{edm})$ between the $|1, \pm1\rangle$ sublevels. (b) The variation of Δ_{hyp} (green solid line) and Δ_S (blue dotted line) with applied electric field.

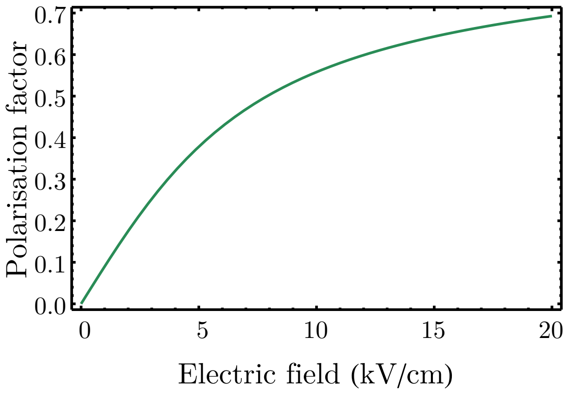

Figure 2.4.: Polarisation factor of the $N = 0$ state.

run the experiment at $10\,\mathrm{kV\,cm^{-1}}$, which gives $\eta = 0.558$. Importantly, reversing the direction of the electric field changes the sign of η.

Zeeman interaction

In the experiment, we also apply a weak magnetic field $\mathbf{B}$ in the presence of a strong electric field. The magnetic field is nominally parallel to the electric field, along the z-axis, but may contain components in the plane perpendicular to the electric field direction. The effective Hamiltonian describing the Zeeman interaction in the ground state is given by

$$\mathcal{H}_{\mathrm{Z}} = g_S \mu_B \mathbf{S} \cdot \mathbf{B} = g_S \mu_B S_z B_z, \tag{2.13}$$

where $g_S \approx 2.002$ is the electron spin g-factor, $\mathbf{S}$ is the total spin and μ_B is the Bohr magneton. We have neglected the Zeeman interaction between the external magnetic field and the nuclear spin of fluorine since it is smaller by a factor of the electron-to-nucleon mass ratio. We have also neglected any component of the magnetic field perpendicular to z; its effect has been shown to be small as it is suppressed by the tensor Stark splitting Δ_{S} [61]. The Zeeman shift is then $\Delta E_{\mathrm{Z}} = g_F \mu_B m_F B_z$, where the relation of g_F to the electron g-factor, $g_S \approx 2$, can be calculated from spherical tensor methods. For the state $(N, F) = (0, 1)$ in which we measure the eEDM, g_F has been calculated to be $g_F = g_S/2 \approx 1$ [85, Appendix B.3].

EDM interaction

Recall that the eEDM is directed along the spin of the electron $\mathbf{S}$, and that in a polar molecule it interacts with an effective electric field directed along the internuclear axis of the molecule $\hat{\mathbf{n}}$. The effective Hamiltonian describing the eEDM interaction in this state is therefore given by

$$\mathcal{H}_{\mathrm{edm}} = -\mathbf{d}_e \cdot \mathbf{E}_{\mathrm{eff}} = d_e \frac{\mathbf{S}}{|\mathbf{S}|} \cdot E_{\mathrm{eff}} \hat{\mathbf{n}}, \tag{2.14}$$

where $\mathbf{E}_{\mathrm{eff}} = -E_{\mathrm{eff}} \hat{\mathbf{n}}$ since by convention $\hat{\mathbf{n}}$ points from the negative (F) to the positive (Yb) nucleus, whereas the internal electric field points in the opposite direction. The energy shift of the $|F, m_F\rangle = |1, \pm 1\rangle$ states, in the presence of an electric field directed along $\hat{\mathbf{z}}$, is $\Delta_{\mathrm{edm}} = -d_e E_{\mathrm{eff}} m_F \langle \hat{\mathbf{n}} \cdot \hat{\mathbf{z}} \rangle = -d_e E_{\mathrm{eff}} m_F \eta$. The polarisation factor η projects the molecule-frame quantity onto the laboratory z-axis.

The combined effect of the Zeeman and EDM interactions is to shift the $|1, \pm 1\rangle$ levels in opposite directions, causing a splitting of magnitude $2(\Delta_{\mathrm{Z}} \mp \Delta_{\mathrm{edm}})$, where the $-$ sign is used when the applied fields **E** and **B** are pointing along the same direction, and $+$ is used when the fields are pointing in opposite directions. This will be crucial for measuring the eEDM, but before moving on to the measurement scheme I will first discuss the transitions between the states that we have described in this section.

2.1.5. Transitions

In this experiment, we are concerned with driving optical transitions between the ground vibrational states in the $\mathrm{X}^2\Sigma^+$ and $\mathrm{A}^2\Pi_{1/2}$ states in the absence of external fields. These optical transitions are shown as green lines in Fig. 2.5. These are electric dipole (E1) transitions and the selection rules are $\Delta F = 0, \pm 1$, $\Delta m_F = 0, \pm 1$ (but not $\Delta m_F = 0$ if $\Delta F = 0$), $\Delta J = 0, \pm 1$ and that the parity of the state must change. There is no selection rule for the vibrational quantum number v since the form of the vibrational potential is different for the two electronic states. The branching ratio from an excited vibrational state v' to a ground vibrational state v is proportional to the squared vibrational wavefunction overlap or Franck-Condon factor, $|\langle v'|v\rangle|^2$. For YbF, $|\langle v' = 0|v = 0\rangle|^2 = 0.928$ [96], so a molecule in $v' = 0$ has a probability of $\Gamma_{v>0} = 0.072$ of decaying into an unaddressed $v > 0$ state, shown as dashed lines in Fig. 2.5. Given these rules we can see from Fig. 2.5 that there are two groups of transitions which are closed apart from branching to other vibrational states. The first closed set of transitions is formed by the Q(0) transitions, which connect the $N = 0$ states to the f states, and the $^{\mathrm{O}}\mathrm{P}_{12}(2)$ transitions, which connect the $N = 2$ states to the f states. The second closed set of transitions are just the P(1) transitions, which connect the $N = 1$ states to the e states. As we will see later, the rotationally-closed nature of these transitions is crucial to the effectiveness of the state preparation and detection schemes.

The microwave transitions are shown as blue lines in Fig. 2.5. These are also E1 transitions and obey the selection rules $\Delta F = 0, \pm 1$, $\Delta m_F = 0, \pm 1$ (but not $\Delta m_F = 0$ if $\Delta F = 0$) and $\Delta N = \pm 1$. This last rule is equivalent to the requirement that the parity of the state must change after the transition. We use the microwave transitions to connect molecular population in the $F = 0, 1$ hyperfine levels in $N = 0$ to the $N = 1$ states.

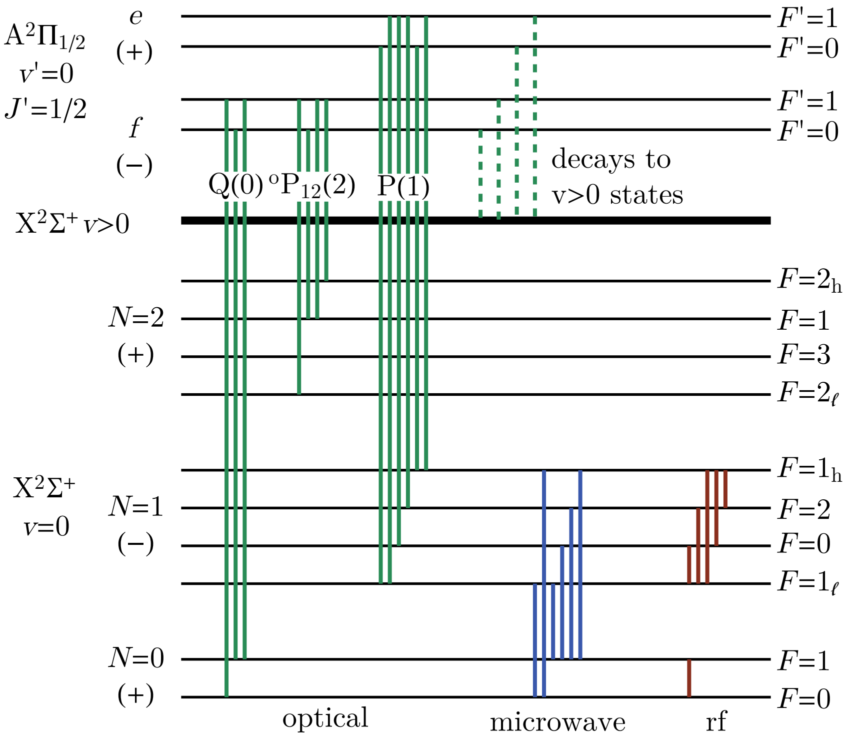

Figure 2.5.: Optical, microwave and rf transitions used in the YbF eEDM experiment.

Finally, the rf transitions are shown as red lines in Fig. 2.5. These are magnetic dipole (M1) transitions and the selection rules that apply are $\Delta F = 0, \pm 1$, $\Delta m_F = 0, \pm 1$ (but not $\Delta m_F = 0$ if $\Delta F = 0$), and that the parity of the initial and final states are the same. We use rf magnetic fields to drive transitions between hyperfine levels in $N = 0$ and $N = 1$.

2.2. Measurement scheme

This section aims to give an overview of our EDM measurement scheme, which is shown in Fig. 2.6. We start by describing a single experimental *shot*, which is a single traverse of the machine by the molecular beam.

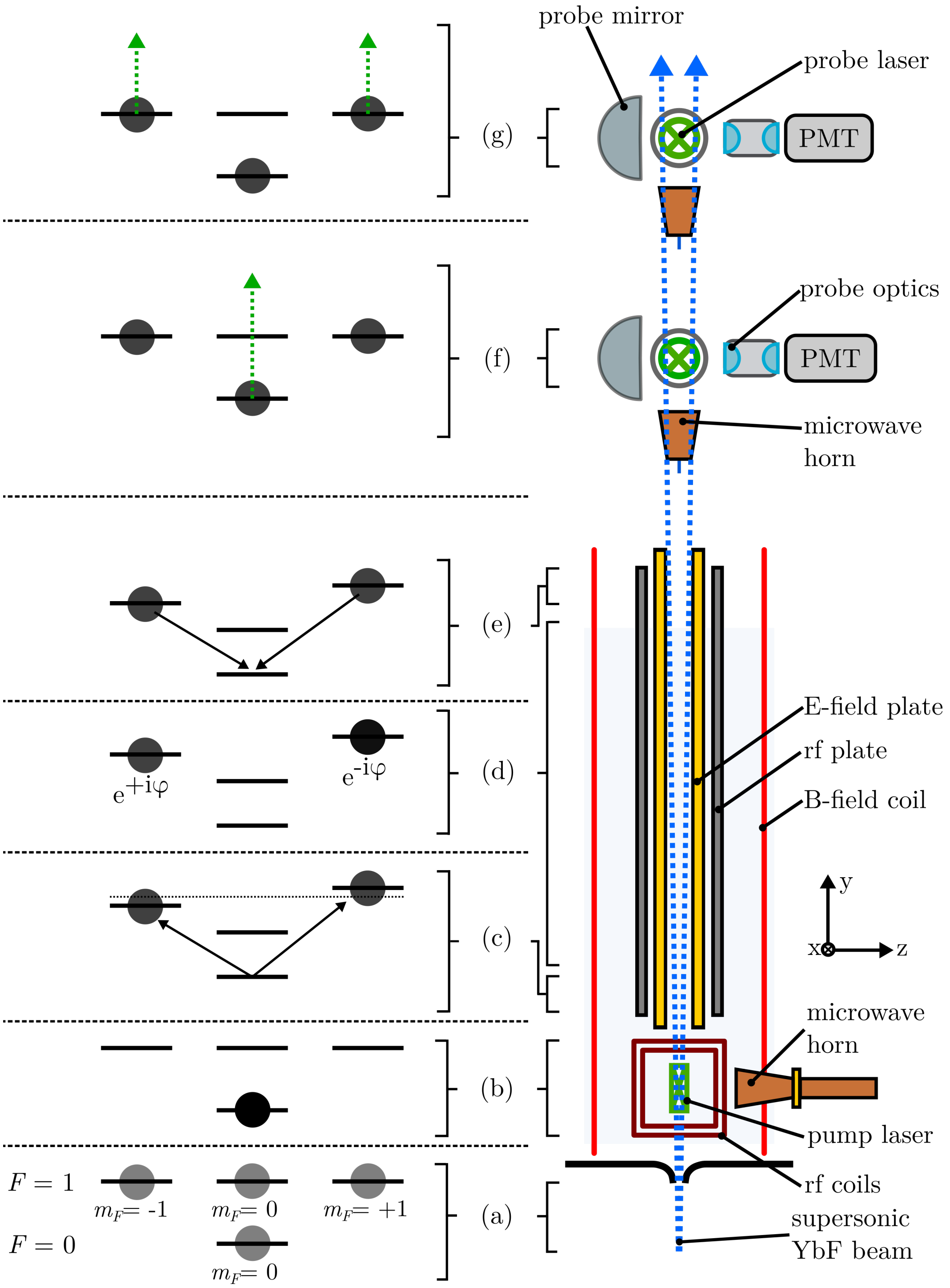

Figure 2.6.: Overview of the experiment and interferometer states. (a) Pulsed beams of YbF molecules are produced with equal populations in the four $N = 0$ sublevels. (b) Population is optically pumped using microwave, rf and optical fields into $F = 0$. (c) An equal superposition of $m_F = +1$ and $m_F = -1$ is created by an rf pulse. (d) The two populated levels accumulate a relative phase due to interaction with **E** and **B** fields. (e) Population in the original superposition is projected back into $F = 0$ by an rf pulse. (f) Population in $F = 0$ is detected. (g) Population in $F = 1$ is detected.

2.2.1. Shot sequence

(a) Molecular beam production

A pulsed supersonic beam of YbF molecules, which has a forward velocity of 600 m/s and a temperature of 2 K, is produced by ablating a Yb target with a pulsed Nd:YAG laser into a supersonically expanding gas jet of Ar and SF_6 [97]. The pulsed beam is produced at a rate of 25 Hz, which is the repetition rate of the experiment.

(b) State preparation

The initial state of the experiment is the $(N, F) = (0, 0)$ state of the ground electronic and vibrational state. The number of molecules participating in the experiment is increased by transferring population from the $N = 0, 1, 2$ states into $0, 0$, as shown in Fig. 2.7. We optically pump population from the even-parity states $(0, 1)$, $(2, 1)$, $(2, 2_\ell)$ and $(2, 2_\mathrm{h})$ into the $(0, 0)$ state via the odd-parity $\mathrm{A}^2\Pi_{1/2}(v' = 0, J' = 1/2, f)$ state. Since the $(2, 2_\mathrm{h})$ and $(2, 1)$ states are closely spaced in energy, we address them using a single laser frequency. Due to the selection rule $\Delta F = \pm 1$, the state $(2, 3)$ does not participate in optical pumping. As mentioned in Section 2.1.5, the set of Q(0) and $^{\mathrm{O}}\mathrm{P}_{12}(2)$ transitions is rotationally closed, so the only loss channels are decays to higher vibrational states. The $N = 1$ states have odd parity and therefore cannot be optically pumped into the even-parity $(0, 0)$ state. Instead, we couple all hyperfine states in $N = 1$ to the $(0, 1)$ state using one microwave field and two rf fields, as shown in Fig. 2.7, so that the population in $N = 1$ can then be optically pumped into $(0, 0)$ as well. This stage of the experiment takes around 40 µs.

(c) Prepare superposition

After being prepared in the $(N, F) = (0, 0)$ state, the molecules enter a region of uniform electric ($\mathbf{E}$) and magnetic ($\mathbf{B}$) fields which are directed along the z-axis. The fields shift the $N = 0$ hyperfine levels as shown in Fig. 2.3. Here, we take the energy of $|F, m_F\rangle = |0, 0\rangle$ to be zero, and the energies of $|1, \pm 1\rangle$ to be $\hbar(\omega \pm \Delta_z)$, where $\Delta_z = \Delta_\mathrm{Z} - \Delta_\mathrm{edm} = \mu_B B - \eta d_e E_\mathrm{eff}$.

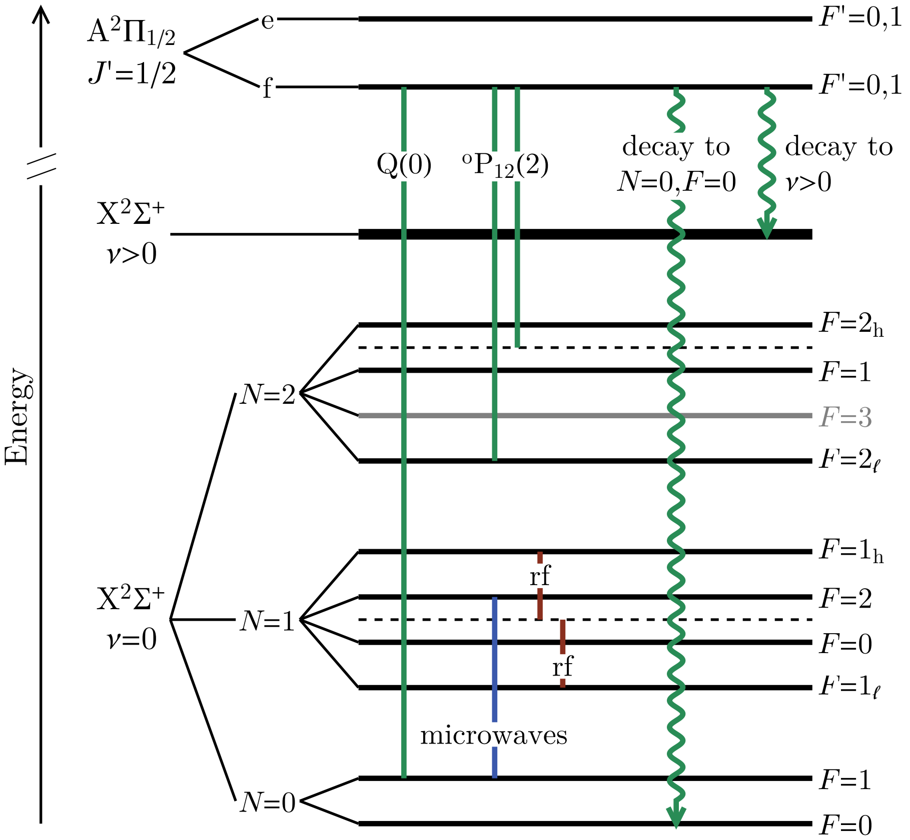

Figure 2.7.: Relevant transitions for state preparation.

A resonant π-pulse of rf magnetic field, at frequency $\omega_{\rm rf}$, with length $\tau_{\rm rf}$ and polarised along the x-axis, transfers population from $|0,0\rangle$ into the state $|x\rangle \equiv (|1,+1\rangle - |1,-1\rangle)/\sqrt{2}$. Typically, $\tau_{\rm rf} = 4\,\mu$s. The state $|x\rangle$ is the $m_F = 0$ state in the basis where the quantisation axis is along the x-axis. The action of the rf pulse can be written as

$$|0,0\rangle \to -\frac{i e^{-i\omega_{\rm rf}\tau_{\rm rf}}}{\sqrt{2}}\left(|1,+1\rangle - |1,-1\rangle\right). \tag{2.15}$$

(d) Evolution in electric and magnetic fields

The molecules then evolve in uniform **E** and **B** fields for an interferometer time $\tau = 800\,\mu\mathrm{s}$ and the superposition above develops a relative phase difference of $2\phi = 2(\Delta_{\mathrm{Z}} - \Delta_{\mathrm{edm}})\tau/\hbar \equiv 2(\phi_B - \phi_E)$, where ϕ_E and ϕ_B are the Zeeman and EDM phases, respectively. The state evolution is

$$i\mathrm{e}^{-i\omega_{\mathrm{rf}}\tau_{\mathrm{rf}}}\left|x\right\rangle \rightarrow -\frac{i\mathrm{e}^{-i\omega_{\mathrm{rf}}\tau_{\mathrm{rf}}}\mathrm{e}^{-i\omega\tau}}{\sqrt{2}}\left(e^{-i\phi}\left|1,+1\right\rangle - e^{i\phi}\left|1,-1\right\rangle\right) \tag{2.16}$$

The state now can be rewritten as:

$$-\frac{i\mathrm{e}^{-i\omega_{\mathrm{rf}}\tau_{\mathrm{rf}}}\mathrm{e}^{-i\omega\tau}}{\sqrt{2}}\left(e^{-i\phi}\left|1,+1\right\rangle - e^{i\phi}\left|1,-1\right\rangle\right) = -i\mathrm{e}^{-i\omega_{\mathrm{rf}}\tau_{\mathrm{rf}}}\mathrm{e}^{-i\omega\tau}\left(\cos\phi\left|x\right\rangle + \sin\phi\left|y\right\rangle\right), \tag{2.17}$$

where $\left|y\right\rangle = -i(\left|1,+1\right\rangle + \left|1,-1\right\rangle)/\sqrt{2}$ is the $m_F = 0$ state in the basis with y as the quantisation axis, and is orthogonal to $\left|x\right\rangle$.

(e) Recombine superposition

A second π-pulse of rf (identical to the first) is applied at the end of the interferometer, which projects the population in $\left|x\right\rangle$ back to the $\left|0,0\right\rangle$ state:

$$-i\mathrm{e}^{-i\omega_{\mathrm{rf}}\tau_{\mathrm{rf}}}\mathrm{e}^{-i\omega\tau}\left(\cos\phi\left|x\right\rangle + \sin\phi\left|y\right\rangle\right) \rightarrow -\cos\phi\left|0,0\right\rangle - i\mathrm{e}^{-2i\omega_{\mathrm{rf}}\tau_{\mathrm{rf}}}\mathrm{e}^{-i\omega\tau}\sin\phi\left|y\right\rangle. \tag{2.18}$$

The probabilities of finding a molecule in the $F = 0$ and $F = 1$ levels are given by $p_0 = \cos^2\phi$ and $p_1 = \sin^2\phi$ respectively.

(f, g) State-sensitive detection

The molecular populations in the $F = 0$ and $F = 1$ levels are then measured in two separate and sequential detectors. We label the detector that measures $F = 0$ population as A, and that which measures $F = 1$ population as B. The detection scheme is shown in Fig. 2.8. In detector A, a resonant microwave field couples the states $(N, F) = (0, 0)$ and $(1, 1_\ell)$. A probe laser together with sidebands, tuned to the P(1) transition, is used to detect the molecules. In detector B, the same is carried out except with resonant microwaves coupling the states $(0, 1)$ and $(1, 2)$ instead, which detects population in $F = 1$. The P(1) transition is rotationally closed, allowing each molecule to scatter, on

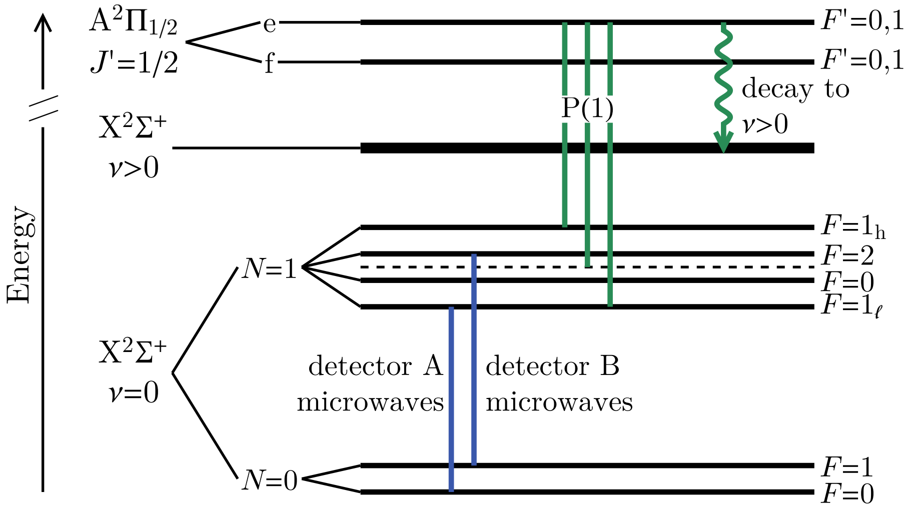

Figure 2.8.: Relevant transitions for state detection.

average, $1/(1-\Gamma_{v>0}) = 13.8$ photons before it decays to a higher vibrational state and becomes dark to the probe laser. In each detector, the molecules interact with the probe lasers for about 20 µs.

2.2.2. Asymmetry

We call the number of photons counted in each detector s_A and s_B, and combine them to form a quantity called the asymmetry, defined as

$$\mathcal{A} = \frac{s_\mathrm{A} - s_\mathrm{B}}{s_\mathrm{A} + s_\mathrm{B}}. \tag{2.19}$$

This quantity is immune to shot-to-shot fluctuations in the number of molecules from the source, N_mol. In the ideal detection case, we have

$$\begin{aligned} s_\mathrm{A} &= N_\mathrm{mol}\epsilon p_0 = N_\mathrm{mol}\epsilon\cos^2\phi, \\ s_\mathrm{B} &= N_\mathrm{mol}\epsilon p_1 = N_\mathrm{mol}\epsilon\sin^2\phi, \end{aligned} \tag{2.20}$$

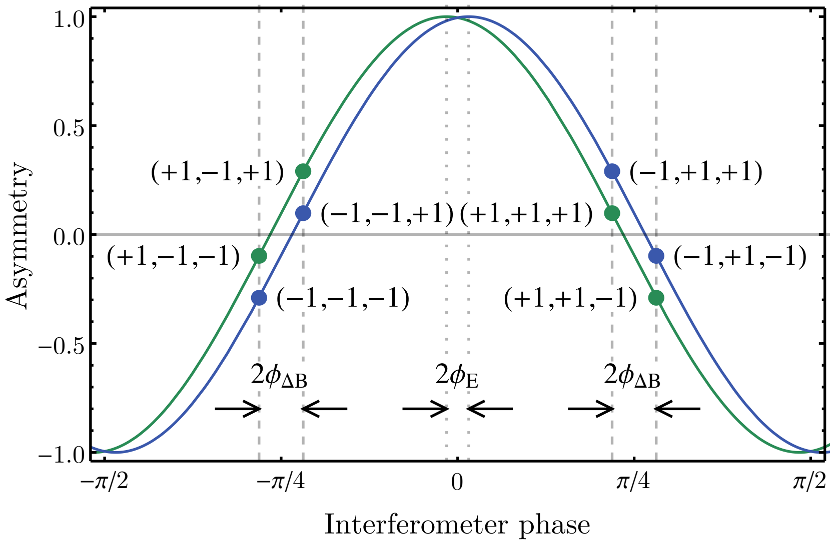

Figure 2.9.: A simple EDM experiment. The phase due to the EDM interaction, ϕ_E, has been exaggerated in this plot. The asymmetry curve is sampled at eight different points, here labelled by their switch state ($\mathtt{E}, \mathtt{B}, \delta\mathtt{B}$).

where ϵ is the number of photons detected per molecule, which we define to be the detection efficiency. The asymmetry is $\mathcal{A} = \cos 2\phi$ in this case. We define the contrast, $\mathcal{C}$, as the amplitude of the $\cos 2\phi$ term in the asymmetry,

$$\mathcal{A} = \mathcal{C} \cos 2\phi. \tag{2.21}$$

In the perfect experiment, we have $\mathcal{C} = 1$. We discuss imperfections which reduce $\mathcal{C}$ in Section 3.5.5.

2.2.3. A simple EDM experiment

The above is a description of a single shot, which by itself is insufficient for us to obtain a value for the eEDM. A simple way to measure the eEDM is to reverse the direction of the electric field and observe the resultant change in $\mathcal{A}$. This is an example of a switched parameter (or simply *switch*), which we define to be able to take on values of +1 and −1. The switch corresponding to the electric field direction is $\mathtt{E} \in \{-1, +1\}$. In practice, two other switches, $\mathtt{B}$ and $\delta\mathtt{B}$ are needed to obtain a physically meaningful measurement of the eEDM. $\mathtt{B} = \pm 1$ corresponds to setting the applied magnetic field such that the

Zeeman phase is $\phi_B = \pm\pi/4$, and $\delta\mathtt{B} = \pm 1$ corresponds to changing the magnitude of the applied magnetic field by a small amount $\mp B_{\delta B}$[3]. The asymmetry measured then depends on the values of these switches:

$$\mathcal{A}(\mathtt{E},\mathtt{B},\delta\mathtt{B}) = \mathcal{C}\cos\left[2\mathtt{B}\left(\frac{\pi}{4} - \delta\mathtt{B}\phi_{\delta B}\right) - 2\mathtt{E}\phi_E\right], \tag{2.22}$$

where $\phi_{\delta B} = \mu_B B_{\delta B}\tau/\hbar$ and $\phi_E = \eta d_e E_{\text{eff}}\tau/\hbar$. Expanding the above expression we get

$$\begin{aligned}\mathcal{A}(\mathtt{E},\mathtt{B},\delta\mathtt{B}) &= \mathcal{C}\cos\left(\mathtt{B}\frac{\pi}{2} - 2\mathtt{B}\delta\mathtt{B}\phi_{\delta B} - 2\mathtt{E}\phi_E\right)\\ &= \mathcal{C}\mathtt{B}\sin\left(2\mathtt{B}\delta\mathtt{B}\phi_{\delta B} + 2\mathtt{E}\phi_E\right)\\ &\approx 2\mathcal{C}\left(\delta\mathtt{B}\phi_{\delta B} + \mathtt{E}\mathtt{B}\phi_E\right),\end{aligned} \tag{2.23}$$

where in the last line we have taken the phases $\phi_{\delta B}$ and ϕ_E to be small and used the approximation $\sin\phi \approx \phi$. We measure $\mathcal{A}$ eight times, once in each of the eight possible permutations of $(\mathtt{E},\mathtt{B},\delta\mathtt{B})$, corresponding to the points highlighted in Fig. 2.9. For a switched parameter $\mathtt{X}$, we define the asymmetry correlated with the parameter as its *channel* $\{\mathtt{X}\}$:

$$\{\mathtt{X}\} = \frac{1}{N}\sum_{i=1}^{N}\mathtt{X}_i\mathcal{A}_i, \tag{2.24}$$

where $\mathtt{X}_i$ and $\mathcal{A}_i$ are the values of the switched parameter and asymmetry in the i^{th} shot. N is the total number of shots, which in this simple experiment is $N = 8$. We can also have channels of multiple parameters, for example,

$$\{\mathtt{X}\cdot\mathtt{Y}\} = \frac{1}{N}\sum_{i=1}^{N}\mathtt{X}_i\mathtt{Y}_i\mathcal{A}_i. \tag{2.25}$$

It is then straightforward to show that for the eight measurements of $\mathcal{A}$ made, $\{\mathtt{E}\cdot\mathtt{B}\} = 2\phi_E\mathcal{C}$ and $\{\delta\mathtt{B}\} = 2\phi_{\delta B}\mathcal{C}$. The eEDM can then be extracted as follows:

$$d_e = \frac{\hbar\phi_{\delta B}}{\eta E_{\text{eff}}\tau}\frac{\{\mathtt{E}\cdot\mathtt{B}\}}{\{\delta\mathtt{B}\}} = \frac{\mu_B B_{\delta B}}{\eta E_{\text{eff}}}\frac{\{\mathtt{E}\cdot\mathtt{B}\}}{\{\delta\mathtt{B}\}}. \tag{2.26}$$

We define a *block* to be a set of N continuous shots which give a single value of d_e when analysed. In the simple experiment described above, $N = 8$ and three parameters were switched. In the real experiment, a block contains $N = 4096$ shots and nine switched

---

[3] This definition is such that $\delta\mathtt{B} = +1(-1)$ moves the point on the interference curve up (down), as shown in Fig. 2.9.

parameters. These other switched parameters do not directly affect the measurement of d_e as described, but instead they help optimise the machine sensitivity and protect against systematic errors and noise. These will be discussed further in Section 3.7.2.

2.3. Sensitivity of the experiment

The sensitivity of the experiment to d_e ultimately depends on how well we can measure a change in the interferometer phase ϕ. Since $\phi_E = \eta d_e E_{\text{eff}}\tau/\hbar$, the uncertainty of the measurement is given by

$$\begin{aligned}\sigma_{d_e} &= \frac{\hbar}{\eta E_{\text{eff}}\tau}\sigma_\phi \\ &= \frac{\hbar}{\eta E_{\text{eff}}\tau}\left|\frac{\partial\phi}{\partial\mathcal{A}}\right|_{\phi=\pm\pi/4}\sigma_{\mathcal{A}} \\ &= \frac{\hbar\sigma_{\mathcal{A}}}{2\eta\mathcal{C}E_{\text{eff}}\tau}.\end{aligned} \tag{2.27}$$

To calculate $\sigma_{\mathcal{A}}$, we need to first consider the uncertainties in the measured photon counts s_{A} and s_{B}.

Let us first assume that the number of molecules N_{mol} is fixed. In the last stage of the interferometer, given by Eq. (2.18), the molecules are projected into the $F = 0$ and $F = 1$ states with probabilities $\cos^2\phi$ and $\sin^2\phi$ respectively, resulting in N_x and N_y molecules populating the respective states. There is inherent quantum projection noise in such a process which causes fluctuations in N_x and N_y [98]. The variances of N_x and N_y due to this are

$$\sigma^2_{N_x} = \sigma^2_{N_y} = N_{\text{mol}}\cos^2\phi\sin^2\phi. \tag{2.28}$$

In each detector, the N_x or N_y molecules are detected with efficiency ϵ. The detection can be separated into two parts: first, each molecule scatters some number of photons n_{sc}, and second, each of these photons are collected by the optics and photomultiplier tube (PMT) with a certain probability ϵ_{c}, giving an overall detection efficiency $\epsilon = n_{\text{sc}}\epsilon_{\text{c}}$. There is some uncertainty associated with the first process, as shown in Ref. [99], but for our experiment the collection efficiency of these photons is so low (this is estimated to be $\epsilon_{\text{c}} = 0.6\%$ [85]) that its effect is small. Nevertheless, we can write the mean and variance in the number of photons scattered by each molecule as $\langle n_{\text{sc}}\rangle$ and $\sigma^2_{n_{\text{sc}}}$. The second detection process can be modelled as a series of Bernoulli trials d_i where the probability of successful detection ($d_i = 1$) is ϵ_{c}.

The photon counts in each detector can then be written as the compound random variables[4]

$$\begin{aligned} s_{\mathrm{A}} &= \sum_{i=1}^{N_x} \sum_{j=1}^{n_{\mathrm{sc},i}} d_{ij} \\ s_{\mathrm{B}} &= \sum_{i=1}^{N_y} \sum_{j=1}^{n_{\mathrm{sc},i}} d_{ij}, \end{aligned} \tag{2.29}$$

whose expectations and variances can be shown to be [100, p. 102 and p. 113]

$$\begin{aligned} \langle s_{\mathrm{A}} \rangle &= \epsilon N_{\mathrm{mol}} \cos^2 \phi \\ \langle s_{\mathrm{B}} \rangle &= \epsilon N_{\mathrm{mol}} \sin^2 \phi \\ \sigma^2_{s_{\mathrm{A}}} &= \left[\epsilon (1 - \epsilon_{\mathrm{c}}) + \epsilon^2_{\mathrm{c}} \sigma^2_{n_{\mathrm{sc}}} \right] N_{\mathrm{mol}} \cos^2 \phi + \epsilon^2 N_{\mathrm{mol}} \cos^2 \phi \sin^2 \phi \\ \sigma^2_{s_{\mathrm{B}}} &= \left[\epsilon (1 - \epsilon_{\mathrm{c}}) + \epsilon^2_{\mathrm{c}} \sigma^2_{n_{\mathrm{sc}}} \right] N_{\mathrm{mol}} \sin^2 \phi + \epsilon^2 N_{\mathrm{mol}} \cos^2 \phi \sin^2 \phi. \end{aligned} \tag{2.30}$$

The two photon counts are clearly not independent of each other, and we can use the same methods as above to calculate their covariance. The result is

$$\mathrm{Cov}[s_{\mathrm{A}}, s_{\mathrm{B}}] = \langle s_{\mathrm{A}} s_{\mathrm{B}} \rangle - \langle s_{\mathrm{A}} \rangle \langle s_{\mathrm{B}} \rangle = -\epsilon^2 N_{\mathrm{mol}} \cos^2 \phi \sin^2 \phi. \tag{2.31}$$

We now define the difference and sum of the photon counts as $s_{\mathrm{D}} = s_{\mathrm{A}} - s_{\mathrm{B}}$ and $s_{\mathrm{T}} = s_{\mathrm{A}} + s_{\mathrm{B}}$. The expectation values and variances of these quantities are [101, p. 351]

$$\begin{aligned} \langle s_{\mathrm{D}} \rangle &= \langle s_{\mathrm{A}} \rangle - \langle s_{\mathrm{B}} \rangle = \epsilon N_{\mathrm{mol}} \cos 2\phi \\ \langle s_{\mathrm{T}} \rangle &= \langle s_{\mathrm{A}} \rangle + \langle s_{\mathrm{B}} \rangle = \epsilon N_{\mathrm{mol}} \\ \sigma^2_{s_{\mathrm{D}}} &= \sigma^2_{s_{\mathrm{A}}} + \sigma^2_{s_{\mathrm{B}}} - 2\,\mathrm{Cov}[s_{\mathrm{A}}, s_{\mathrm{B}}] = \epsilon N_{\mathrm{mol}} \left[1 + \frac{\epsilon}{2} \sin^2 2\phi + \frac{\epsilon}{n_{\mathrm{sc}}} \left(\frac{\sigma^2_{n_{\mathrm{sc}}}}{\langle n_{\mathrm{sc}} \rangle} - 1 \right) \right] \\ \sigma^2_{s_{\mathrm{T}}} &= \sigma^2_{s_{\mathrm{A}}} + \sigma^2_{s_{\mathrm{B}}} + 2\,\mathrm{Cov}[s_{\mathrm{A}}, s_{\mathrm{B}}] = \epsilon N_{\mathrm{mol}} \left[1 + \frac{\epsilon}{n_{\mathrm{sc}}} \left(\frac{\sigma^2_{n_{\mathrm{sc}}}}{\langle n_{\mathrm{sc}} \rangle} - 1 \right) \right], \end{aligned} \tag{2.32}$$

---

[4] A compound random variable S is defined as the sum of a random number N of i.i.d. variables X_i, i.e. $S = \sum_{i=1}^{N} X_i$ [100, p. 102].

while the covariance between these two quantities is

$$\begin{aligned}\mathrm{Cov}[s_\mathrm{D}, s_\mathrm{T}] &= \langle s_\mathrm{D} s_\mathrm{T}\rangle - \langle s_\mathrm{D}\rangle\langle s_\mathrm{T}\rangle \\ &= \langle s_\mathrm{A}^2 - s_\mathrm{B}^2\rangle - \langle s_\mathrm{D}\rangle\langle s_\mathrm{T}\rangle \\ &= \langle s_\mathrm{A}\rangle^2 + \sigma_{s_\mathrm{A}}^2 - \langle s_\mathrm{B}\rangle^2 - \sigma_{s_\mathrm{B}}^2 - \langle s_\mathrm{D}\rangle\langle s_\mathrm{T}\rangle \\ &= \epsilon N_\mathrm{mol}\left[1 + \frac{\epsilon}{n_\mathrm{sc}}\left(\frac{\sigma_{n_\mathrm{sc}}^2}{\langle n_\mathrm{sc}\rangle} - 1\right)\right]\cos 2\phi,\end{aligned} \tag{2.33}$$

where in the second-to-last line we have used the variance formula $\sigma_X^2 = \langle X^2\rangle - \langle X\rangle^2$. Finally, we are in a position to calculate the variance in the asymmetry $\mathcal{A} = s_\mathrm{D}/s_\mathrm{T}$. The variance of a ratio of two random variables is a standard result [101, p. 351], giving

$$\sigma_\mathcal{A}^2 = \left(\frac{\langle s_\mathrm{D}\rangle}{\langle s_\mathrm{T}\rangle}\right)^2\left(\frac{\sigma_{s_\mathrm{D}}^2}{\langle s_\mathrm{D}\rangle^2} + \frac{\sigma_{s_\mathrm{T}}^2}{\langle s_\mathrm{T}\rangle^2} - \frac{2\,\mathrm{Cov}[s_\mathrm{D}, s_\mathrm{T}]}{\langle s_\mathrm{D}\rangle\langle s_\mathrm{T}\rangle}\right). \tag{2.34}$$

Substituting Eqs. (2.30) to (2.33) into Eq. (2.34) yields the form

$$\sigma_\mathcal{A}^2 = \frac{\sin^2 2\phi}{\epsilon N_\mathrm{mol}}\left[1 + \epsilon\left(1 - \frac{1}{\langle n_\mathrm{sc}\rangle} + \frac{\sigma_{n_\mathrm{sc}}^2}{\langle n_\mathrm{sc}\rangle^2}\right)\right]. \tag{2.35}$$

Since the experiment is conducted at the phases $\phi = \pm\pi/4 + \delta\phi$, where $\delta\phi \ll 1$, substituting this into the above expression gives

$$\sigma_\mathcal{A}^2 = \frac{1}{\epsilon N_\mathrm{mol}}\left[1 + \epsilon\left(1 - \frac{1}{\langle n_\mathrm{sc}\rangle} + \frac{\sigma_{n_\mathrm{sc}}^2}{\langle n_\mathrm{sc}\rangle^2}\right)\right] + O(\delta\phi^2) \approx \frac{F_\mathrm{det}}{\langle s_\mathrm{T}\rangle}. \tag{2.36}$$

Since s_T is just the total photon count in both detectors, we are left with the simple result that the fundamental uncertainty in our measurement is limited by the Poissonian shot-noise from counting photons, modified by a small factor due to the optical cycling nature of the detection process, F_det. In Appendix B, I calculate this factor to be $F_\mathrm{det} = 1.15$. Substituting this result into Eq. (2.27) gives us the shot-noise-limited sensitivity of the experiment:

$$\xi_{d_e} = \frac{\hbar\sqrt{F_\mathrm{det}}}{2\eta E_\mathrm{eff}\tau\mathcal{C}\sqrt{\langle s_\mathrm{T}\rangle}}. \tag{2.37}$$

To maximise the sensitivity of the experiment, we should therefore maximise the polarisation factor η, interferometer time τ, contrast $\mathcal{C}$ and total photon count s_T. The polarisation factor has a maximum value of 1, and to achieve full polarisation requires much larger electric fields than we can currently support (see Section 3.4.3). The interferometer time τ is limited by the length of the plates and machine, which has not been changed for the work described in this thesis. The main upgrades to the experiment since the 2011 measurement are the new state preparation and detection techniques, which increase s_{T} while maintaining a high $\mathcal{C}$. These are described in Sections 3.3 and 3.5.

3. Experimental methods

This chapter describes the methods and apparatus used in the YbF eEDM experiment. I start by describing the vacuum system and computer control of the experiment. Then, I explain in detail each section of the beam machine, which has been sketched out in Fig. 2.6. Next, I give an overview of the newly-installed magnetometers. Finally, with all the necessary information provided, I outline the details of how we carry out the full eEDM measurement.

3.1. Common hardware

This section describes the infrastructure that is common to all the subsequent sections in the chapter. The beam machine is a 2 m-long vertical stainless steel vacuum chamber. It is made up of three parts: the source chamber at the bottom, followed by the main chamber where the interferometry is carried out, and then the detection chamber at the top. The main and detection chambers of the beam machine are shown in Fig. 3.1. All of the labelled parts will be discussed in this chapter.

3.1.1. Vacuum system

The source chamber is pumped by three turbomolecular pumps while the main and detection chambers are pumped by a single turbomolecular pump at the top of the machine. The pumping is separate since the source chamber is separated from the others by a skimmer with a 2 mm aperture. The turbomolecular pumps are backed by

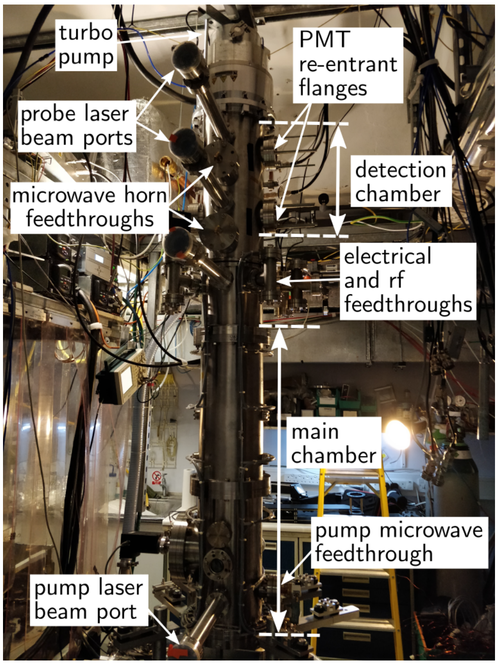

Figure 3.1.: Beam machine, showing the main and detection chambers. There is an inner magnetic shield inside of the main chamber. The two outer magnetic shields have been removed.

a dry scroll pump. The pressure in both chambers is typically around 2×10^{-7} mbar, which is low enough that we can neglect collisions with the background gas [61].

Importantly, all the turbomolecular pumps used have magnetically-levitated bearings. We found that using pumps that had grease-lubricated bearings caused the machine to vibrate, which in turn resulted in fluctuations in the magnetic field inside the machine that can be correlated to machine vibrations. This source of magnetic field noise disappeared once we switched over to magnetically-levitated pumps. We will discuss this further in Section 4.3.1.

3.1.2. Computer control

The main computer used in the experiment is an *NI PXIe-8130* embedded controller. To control the hardware and acquire data, we use a variety of data acquisition and analog and digital output modules from *National Instruments*. The embedded controller also has a serial port, several USB ports and a GPIB connector, which enables us to control a variety of instruments. One important aspect of our experimental control is the digital pattern generator, which is a digital output module tasked specifically with the output of TTL pulses. The pattern generator controls the timing of various experimental procedures during a single shot. A collection of custom software applications[1] is used to run all our experiments [84].

3.2. Molecule source

The molecule source used in our experiment produces a large, stable flux of molecules (about 10^5 detected molecules per pulse) at a repetition rate of 25 Hz. It requires only a small amount of regular maintenance to function reliably and as such, it has been virtually unchanged for many years. The source was built by M. Tarbutt [97] and installed on the experiment by P. Condylis [102] in 2006. A detailed description of the source can be found in [84]. I will give a brief description here for completeness.

A pulsed beam of YbF molecules is produced by laser ablation of Yb metal in the presence of SF_6 gas. A *Brilliant* Q-switched Nd:YAG pulsed laser is used for ablation. It receives two digital triggers from the pattern generator: one to trigger the flashlamp pulse and the second to trigger the Q-switch. The Yb is a 3 mm-wide strip of metal that is glued onto the rim of a stainless steel disc – this is called the target wheel. The target wheel can be rotated by a computer-controlled motor and drive shafts, and rotating this wheel (which we call target-stepping) allows the laser to hit a fresh spot of Yb. We find that the after a period of laser ablation (typically tens of minutes), a black substance builds up on the Yb which prevents further molecule formation. During extended periods of data-taking, the target-stepping procedure is automated. Typically, the entire rim is blackened after a week of constant use, and we then need to remove the target wheel in order to scrape off the black substance with a file. The SF_6 is mixed with argon[2] and the gas mixture is introduced into the source chamber via a pulsed solenoid valve. The release of the gas from the valve is also triggered by a TTL pulse from the pattern generator.

---

[1] `https://github.com/ColdMatter/EDMSuite/`

[2] We use a 2% SF_6, 98% Ar mixture.

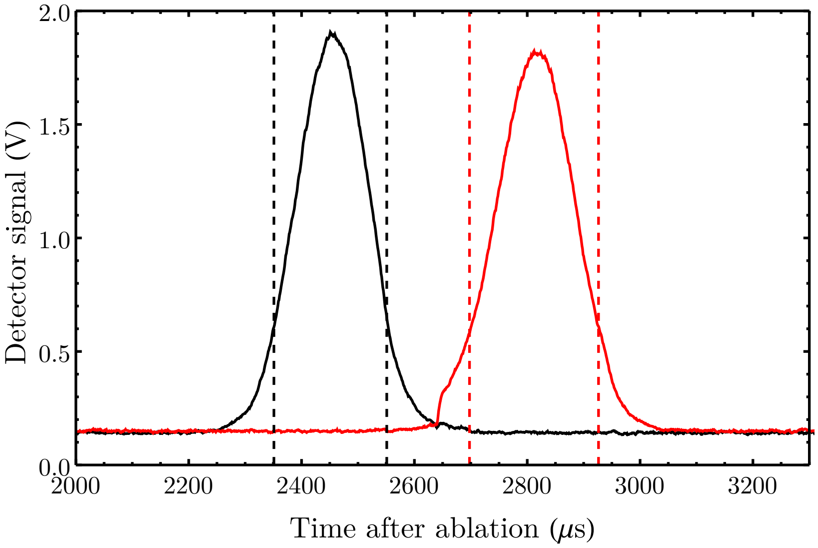

Figure 3.2.: A typical set of time-of-flight (TOF) curves showing the detection of molecules in the lower (black curve) and upper (red curve) detectors. The dashed lines show the integration ranges used for results presented in Section 3.5.

The gas mixture supersonically expands from a region of high pressure (inside the valve) to a region of low pressure (inside the source chamber), which cools it down to 4 K while increasing its forward velocity [97]. As YbF molecules are produced, they are entrained and cooled to 4 K by this gas mixture. A skimmer, with a 2 mm-diameter aperture, is used to separate the source chamber from the main experimental chamber. The skimmer is also designed to prevent shock waves from destroying the molecular beam as it passes through to the main chamber. The molecular beam that emerges has a mean forward velocity of 600 $\mathrm{m\,s^{-1}}$. A typical set of time-of-flight curves, showing the detection of molecules in both detectors, is shown in Fig. 3.2. Molecule detection is further discussed in Section 3.5.

As described in [84], the molecular flux can be maximised by scanning over three source parameters: the time the gas valve is held open, the time between opening the valve and triggering the Q-switch and the time between triggering the flashlamp and Q-switch in the laser. This optimisation is usually carried out once every few months as these parameters can change as the flashlamp in the laser degrades. We also find that day-to-day optimisation of the molecular flux can be done by adjusting the position of the laser ablation spot and the valve drive voltage[3]. The time of the Q-switch trigger is conventionally taken as $t = 0$ in a single shot, as this is the time that the molecules are formed by laser ablation.

3.3. State preparation

After producing a molecular beam, we prepare the YbF molecules in the initial state $(N, F) = (0, 0)$. This is done by optically pumping population in $(0, 1)$ as well as the $N = 2$ hyperfine levels, and coupling population in $N = 1$ into the optical cycle by microwaves and rf. The scheme was shown in Fig. 2.7 and it had already been successfully implemented by the time I joined the experiment, as reported in [86]. Here I will give a brief overview of the hardware and results.

3.3.1. Hardware and apparatus

Figure 3.3 shows the state preparation region. The molecular beam travels vertically along the y-axis. The pump lasers are a set of counter-propagating elliptical beams which travel along the x-axis. These beams have $1/\mathrm{e}^2$ diameters of $23.5 \times 2.2\,\mathrm{mm}$ along the y and z axes, providing an interaction time of $40\,\mu\mathrm{s}$ with the molecules. The peak laser intensities are approximately $120\,\mathrm{mW/cm^2}$, $340\,\mathrm{mW/cm^2}$ and $140\,\mathrm{mW/cm^2}$ for the frequency components addressing the $(N, F) = (0, 1)$ state, the $(2, 2_\mathrm{h})$ and $(2, 1)$ states, and the $(2, 2_\ell)$ state, respectively. A microwave horn delivers a maximum of 19 dBm of power at the frequency resonant with the $(0, 1) \to (1, 2)$ transition, $f_{F=1} = 14\,458\,057\,\mathrm{kHz}$. The horn was designed by J. Devlin and the details of their construction and installation can be found in [85]. A set of resonant rf coils, designed by B. Sauer, surround the molecular beam path [86]. Their resonances are tuned to 30.9 MHz, 155.7 MHz and 161.2 MHz. The rf is delivered via a drive coil which couples the rf to the resonant coils. The latter then generate rf radiation which drive M1 transitions between the hyperfine levels in $N = 1$.

---

[3] The valve drive voltage and the time the gas valve is held open are linked. The former controls how much the solenoid valve is opened and the latter controls how long it is open for, and so both control how much gas is let through per pulse.

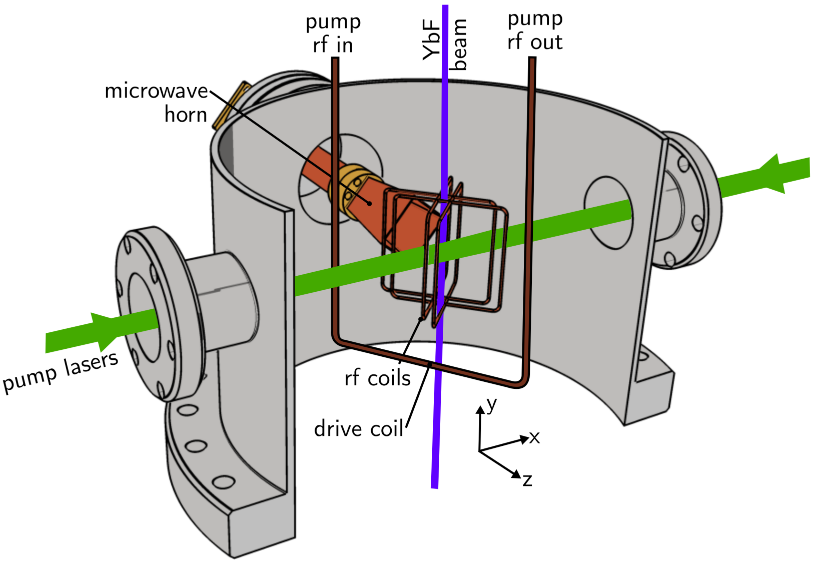

Figure 3.3.: The state preparation region. The radiation needed for the optical pumping scheme is provided by two counter-propagating laser beams, the microwave horn, and the rf coils. The rf coils are driven by a drive coil. There is also a clean-up beam that co-propagates with one of the pump laser beams.

An overview of the hardware used to generate the different forms of radiation is shown in Fig. 3.4. The laser addressing the $(0, 1)$ state is called the $N = 0$ pump laser. This laser is generated first by an IR seed laser – the *Toptica DL pro*, which is a grating-stabilised diode laser. The output of this seed laser is fibre-coupled to a Yb fibre amplifier from *Keopsys*, which increases the IR power to 5 W. The amplified IR is then frequency-doubled in free space using a periodically-poled lithium niobate (PPLN) crystal from *Covesion*, which is temperature-controlled in order to satisfy the phase-matching condition in the crystal. The power of the frequency-doubled output is usually around 400 mW. A second laser, tuned to the ${}^{O}P_{12}(2)$ transition, is called the $N = 2$ pump laser. This is a frequency-doubled solid state fibre laser: the *Menlo Orange One* equipped with a doubler head made by *NTT*, which has an output power of 200 mW. The frequency of this laser is tuned to the $F = 2_\ell$ component of the ${}^{O}P_{12}(2)$ transition. The output from this laser is split by a $\lambda/2$ waveplate and polarising beamsplitter (PBS), and recombined after an acousto-optic modulator (AOM) shifts the frequency of one of the beams downwards by 185.5 MHz to the middle of the $F = 2_\mathrm{h}$ and $F = 1$ components of the ${}^{O}P_{12}(2)$ transition. This allows us to address three of the four hyperfine components in $N = 2$, as described in Section 2.2.1. As Fig. 3.4 shows, both the $N = 0$ and $N = 2$ lasers are combined on a PBS, which produces two output beams, each containing an equal amount of power for each of the three frequency components. The two beams are shaped by cylindrical lenses to achieve the required beam dimensions and directed to the state preparation region.

Additionally, there is a clean-up beam that co-propagates with one of the pump beams. This beam comes from the detection lasers and contains the three frequencies needed to drive the P(1) transitions, as described later in Section 3.5. The beam is broadened to have a bandwidth of about 200 MHz using an overdriven EOM resonant at 25 MHz, as shown in Fig. 3.4. The purpose of the clean-up beam is to remove any molecular population from states which have transitions close to the P(1) transition so that the former transitions do not contribute to unwanted detector background. We will defer further discussion of the clean-up beam until we have discussed state detection in Section 3.5.

The pump lasers are locked, using a transfer cavity method [103], to a stabilised *Moglabs* reference laser that is in turn locked to a Rb atomic transition using Zeeman-modulated spectroscopy. A dichroic mirror (DM) is used to combine the pump and reference lasers into a scanning Fabry-Perot cavity. The cavity length is scanned using a triangle wave at a frequency of 26 Hz, with the scan range chosen such that the transmission peaks from the two pump lasers and the reference laser are visible in one scan. The cavity lengths at which the two pump lasers and reference laser are transmitted are L_{p1}, L_{p2} and L_{ref} respectively. The pump lasers are locked to the reference laser by keeping the differences $L_{\mathrm{p1}} - L_{\mathrm{ref}}$ and $L_{\mathrm{p2}} - L_{\mathrm{ref}}$ constant. We achieve a frequency stability of about 1 MHz using this locking method.

The microwaves are generated by an *Anapico APSYN420* synthesiser which can be controlled via GPIB. The same hardware is responsible for generating the microwave frequencies needed for state preparation, as well as those used in state detection (see Section 3.5). The microwave frequency can be adjusted within a single shot using the *List sweep* function of the synthesiser. The amplitude is controlled via a mixer and an analog multiplexer, which selects the appropriate input for the particular region that the microwaves are being sent to. The initial switch controls the microwave pulse time and duration, while the three-way switch is responsible for directing the microwaves to the correct region.

The rf fields are generated by home-built voltage-controlled oscillators (VCOs). It was found during testing that the radiation at 155.7 MHz has very little effect on the optical

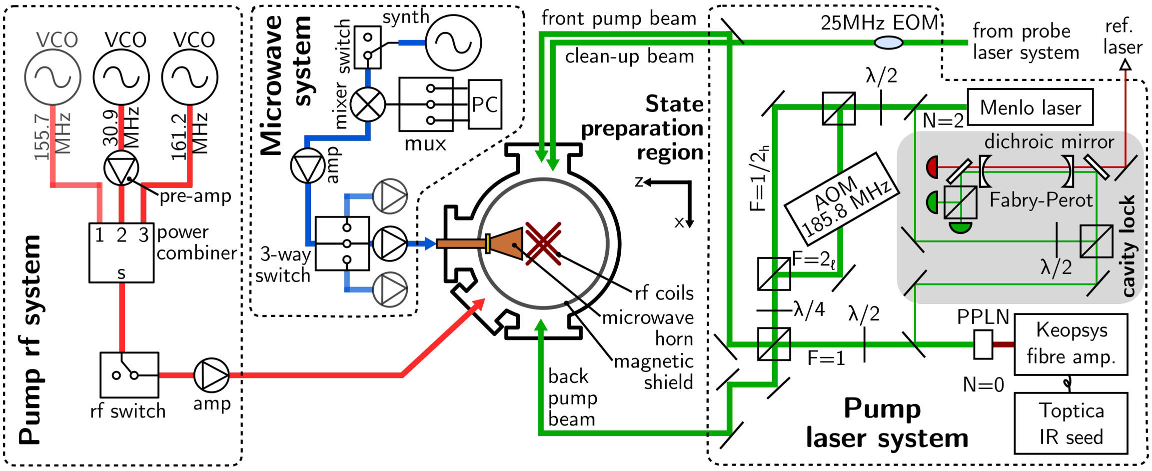

Figure 3.4.: Overview of hardware used to generate optical, microwave and rf radiation for state preparation. The 155.7 MHz VCO, although present, was not used for the experiment.

pumping [86], and we have therefore not used it. We adjust the rf amplitudes directly at the VCOs. The two rf fields are then combined, amplified and sent into the drive coil.

3.3.2. Results

Figure 3.5 shows the results of the state preparation scheme which were obtained by I. Rabey [86]. Using one of the two detectors, we measure the population in $(0, 0)$ by scanning the frequency of a weak probe laser around the $F = 0$ component of the Q(0) transition, and detecting the laser-induced fluorescence. When we add only the $N = 0$ pump laser, which was the method used in the previous eEDM measurement [57, 62], the signal increases by a factor 1.8 ± 0.2 over the signal from the thermal population in $F = 0$. The origin of the error bar is shot-to-shot fluctuations in the number of molecules. Numerical simulations using optical Bloch equations (OBEs), carried out by J. Devlin [85], predict a factor of 1.9, in good agreement with the measurement. When we add the $N = 2$ pump laser, the enhancement factor grows to 5.9 ± 0.6. Adding the microwave field increases this to 8.7 ± 0.8, and adding the rf fields increases this further to 11.8 ± 1.2. This last factor is again in agreement with OBE simulations which predict a signal increase of 10.5.

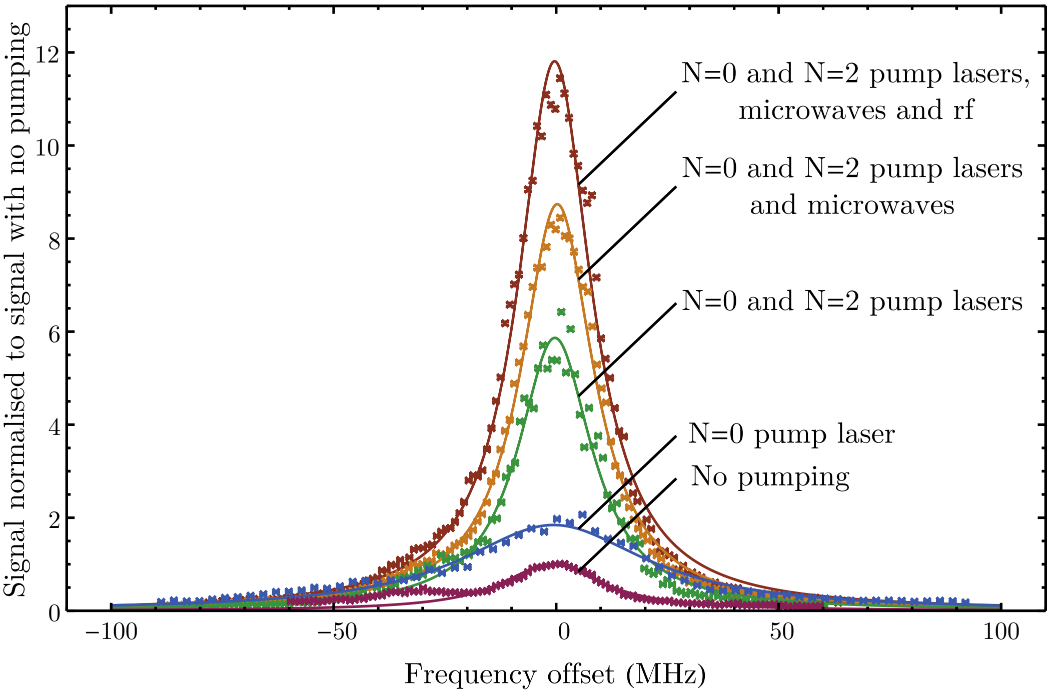

Figure 3.5.: Increase in molecule population in the $(N, F) = (0, 0)$ state due to optical, microwave and rf fields. The signal is normalised to the $F = 0$ signal with no optical pumping.

3.4. Interferometer

The molecules, now prepared in their initial state $|F, m_F\rangle = |0, 0\rangle$, travel into the interferometer region. We have already described the action of the interferometer with idealised rf π-pulses in Section 2.2.1, and the probabilities of finding a molecule in the $F = 0$ and $F = 1$ hyperfine states in $N = 0$ after the interferometer region are given by $p_0 = \cos^2 \phi$ and $p_1 = \sin^2 \phi$ respectively, as shown in Fig. 3.6(a). The unequal amplitudes for each detection are due to several imperfections which are discussed in Section 3.5. The signals are combined into the asymmetry defined in Eq. (2.19), as shown in Fig. 3.6(b).

I will first motivate some of the methods in this section by giving an overview of how imperfections in the rf pulses can lead to reduced sensitivity and potential systematic errors in the measurement. Then, I will give an overview of the interferometer apparatus before discussing why we replaced the electric field plates.

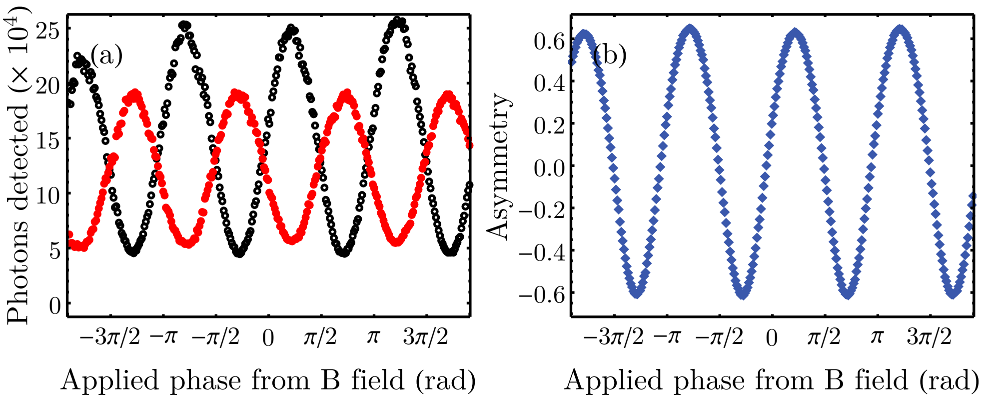

Figure 3.6.: (a) Interference curves for detector A, which detects $F = 0$ molecules (black), and detector B, which detects $F = 1$ molecules (red). (b) Asymmetry interference curve calculated from (a) and Eq. (2.19).

3.4.1. Imperfections in rf pulses

Let us consider imperfections in the rf pulses and their effect on the interferometer output. The amplitude of each rf pulse may not be optimised, such that the π-pulse condition $\Omega_i \tau_{\text{rf}} = \pi$ is not satisfied. Here, Ω_i is the Rabi frequency of the i^{th} rf pulse and τ_{rf} is the rf pulse length (same for both pulses). There may be some non-zero detuning of the rf from resonance, $\delta_i = \omega_{\text{rf},i} - \Delta_{\text{hyp},i}$, where ω_{rf} is the rf frequency and Δ_{hyp} is the hyperfine splitting between $|F, m_F\rangle = |0,0\rangle$ and $|1,\pm 1\rangle$ (see Fig. 2.3). We will also consider a possible rotation of the polarisation angle of the rf magnetic field in the x-y plane.

The z basis states for the $N = 0$ manifold are $(|0,0\rangle, |1,-1\rangle, |1,+1\rangle)$, where we have ignored the $|1,0\rangle$ level because it does not participate in the rf transitions. In this basis, the free evolution of the state in uniform electric and magnetic fields can be described by the propagator [84]

$$\Pi_{\text{free}}(\tau) = \begin{pmatrix} 1 & 0 & 0 \\ 0 & \mathrm{e}^{-i(\Delta_{\text{hyp}} - \Delta_z)\tau} & 0 \\ 0 & 0 & \mathrm{e}^{-i(\Delta_{\text{hyp}} + \Delta_z)\tau} \end{pmatrix}, \tag{3.1}$$

where $\Delta_z = \Delta_{\text{Z}} - \Delta_{\text{edm}}$ is the half the energy splitting between $|1,\pm 1\rangle$ due to the Zeeman and eEDM interactions.

To describe the rf transitions, it is more convenient to work in a rotated basis which we call the Cartesian basis, given by $\{|0,0\rangle, |x(\theta_{\mathrm{rf}})\rangle, |y(\theta_{\mathrm{rf}})\rangle\}$. The state $|x(\theta_{\mathrm{rf}})\rangle = (\mathrm{e}^{-i\theta_{\mathrm{rf}}}|1,+1\rangle - \mathrm{e}^{i\theta_{\mathrm{rf}}}|1,-1\rangle)/\sqrt{2}$ is the state excited by rf polarised along the polar angle θ_{rf} in the x-y plane. The state $|y(\theta_{\mathrm{rf}})\rangle = -i(\mathrm{e}^{-i\theta_{\mathrm{rf}}}|1,+1\rangle + \mathrm{e}^{i\theta_{\mathrm{rf}}}|1,-1\rangle)/\sqrt{2}$ is simply the state orthogonal to $|x(\theta_{\mathrm{rf}})\rangle$. The rotation from the z basis to Cartesian basis can be described by the transformation

$$\mathrm{U}(\theta_{\mathrm{rf}}) = \frac{1}{\sqrt{2}} \begin{pmatrix} \sqrt{2} & 0 & 0 \\ 0 & -\mathrm{e}^{i\theta_{\mathrm{rf}}} & -i\mathrm{e}^{i\theta_{\mathrm{rf}}} \\ 0 & \mathrm{e}^{-i\theta_{\mathrm{rf}}} & -i\mathrm{e}^{-i\theta_{\mathrm{rf}}} \end{pmatrix}. \tag{3.2}$$

A state in the z-basis can be transformed to the Cartesian basis as follows: $|\psi\rangle_{\mathrm{c},\theta} = \mathrm{U}^{\dagger}(\theta)\,|\psi\rangle_z$.

In the Cartesian basis, the evolution of a state when an rf pulse of length τ_{rf} and initial phase Φ_{rf} is applied can be described by the propagator [84]

$$\Pi_{\mathrm{rf}}(\tau_{\mathrm{rf}}, \Phi_{\mathrm{rf}}) = -i\mathrm{e}^{-\frac{i\Delta_{\mathrm{hyp}}\tau_{\mathrm{rf}}}{2}} \begin{pmatrix} (ic + \frac{\delta}{W}s)\mathrm{e}^{\frac{i\omega_{\mathrm{rf}}\tau_{\mathrm{rf}}}{2}} & \frac{\Omega}{W}s\mathrm{e}^{\frac{i\omega_{\mathrm{rf}}\tau_{\mathrm{rf}}}{2}}\mathrm{e}^{i\Phi_{\mathrm{rf}}} & 0 \\ \frac{\Omega}{W}s\mathrm{e}^{-\frac{i\omega_{\mathrm{rf}}\tau_{\mathrm{rf}}}{2}}\mathrm{e}^{-i\Phi_{\mathrm{rf}}} & (ic - \frac{\delta}{W}s)\mathrm{e}^{-\frac{i\omega_{\mathrm{rf}}\tau_{\mathrm{rf}}}{2}} & 0 \\ 0 & 0 & \mathrm{e}^{-i\frac{\Delta_{\mathrm{hyp}}\tau_{\mathrm{rf}}}{2}} \end{pmatrix}, \tag{3.3}$$

where $c = \cos\left(\frac{W\tau_{\mathrm{rf}}}{2}\right)$, $s = \sin\left(\frac{W\tau_{\mathrm{rf}}}{2}\right)$ and $W = \sqrt{\Omega^2 + \delta^2}$.

The initial state of the molecules in the z basis is $|\psi_0\rangle_z = (1, 0, 0)$, i.e. all the molecules are in $|0,0\rangle$. Let the two rf pulses, each of length τ_{rf}, be applied at times $t = 0$ and $t = \tau + \tau_{\mathrm{rf}}$. Then the state after the second rf pulse in the z basis is

$$\begin{aligned} |\psi\rangle_z = {} & \mathrm{U}(\theta_{\mathrm{rf},2}) \cdot \Pi_{\mathrm{rf},2}(\tau_{\mathrm{rf}}, \omega_{\mathrm{rf}}(\tau + \tau_{\mathrm{rf}}) + \phi_{\mathrm{rf}}) \cdot \mathrm{U}^{\dagger}(\theta_{\mathrm{rf},2}) \cdot \Pi_{\mathrm{free}}(\tau) \cdot \mathrm{U}(\theta_{\mathrm{rf},1}) \\ & \cdot \Pi_{\mathrm{rf},1}(\tau_{\mathrm{rf}}, 0) \cdot \mathrm{U}^{\dagger}(\theta_{\mathrm{rf},1}) \cdot |\psi_0\rangle_z . \end{aligned} \tag{3.4}$$

We are able to add an additional phase shift of ϕ_{rf} between the two rf pulses, which will prove to be very useful. Writing the amplitudes in the final state as $|\psi\rangle_z = (a_0, a_-, a_+)$, the probabilities that the molecule can be found in $F = 0$ and $F = 1$ are given by

$p_0 = |a_0|^2$ and $p_1 = 1 - |a_0|^2$. Evaluating Eq. (3.4), we can show that

$$\begin{aligned} p_0 &= A_\mathrm{I}\cos^2(\phi - \Delta\theta_\mathrm{rf}) + A_\mathrm{R}\cos(\phi - \Delta\theta_\mathrm{rf}) + A_0, \\ p_1 &= A_\mathrm{I}\sin^2(\phi - \Delta\theta_\mathrm{rf}) - A_\mathrm{R}\cos(\phi - \Delta\theta_\mathrm{rf}) + A_1, \end{aligned}$$

$$\begin{aligned} A_\mathrm{I} &= s_1^2 s_2^2 \beta_1^2 \beta_2^2, \\ A_\mathrm{R} &= 2 s_1 s_2 \beta_1 \beta_2 \left[(s_1 s_2 \alpha_1 \alpha_2 - c_1 c_2)\cos\vartheta + (s_1 c_2 \alpha_1 + s_2 c_1 \alpha_2)\sin\vartheta\right], \\ A_0 &= (c_1^2 + s_1^2\alpha_1^2)(c_2^2 + s_2^2\alpha_2^2), \\ A_1 &= 1 - A_0 - A_\mathrm{I} \end{aligned} \tag{3.5}$$

where $\alpha_i = \delta_i/W_i$ and $\beta_i = \Omega_i/W_i$. The relative phase accumulated between the rf and the molecules is $\vartheta = \delta_2(\tau + \tau_\mathrm{rf}) - \delta_1\tau_\mathrm{rf} + \phi_\mathrm{rf}$, and the relative angle between the polarisation direction of the two rf pulses is $\Delta\theta_\mathrm{rf} = \theta_\mathrm{rf,2} - \theta_\mathrm{rf,1}$. A_I is the amplitude of the main interference signal, A_R is a term due to the Ramsey interference between $|0,0\rangle$ and the $|1,\pm1\rangle$ states, and $A_{0/1}$ are constant terms.

Substituting these expressions into the expression for the asymmetry in Eq. (2.19), we see that

$$\mathcal{A} = A_\mathrm{I}\cos(2\phi - 2\Delta\theta_\mathrm{rf}) + 2A_\mathrm{R}\cos(\phi - \Delta\theta_\mathrm{rf}) + (2A_0 + A_\mathrm{I} - 1). \tag{3.6}$$

Any imperfections in the rf amplitude and frequency will therefore reduce interferometric contrast since $A_\mathrm{I} < 1$. They also lead to the appearance of a Ramsey term and a constant term. The Ramsey term is a potential source of systematic error since it depends strongly on the detuning δ, which can depend on the switch state `E` if there is any asymmetry in switching the electric field which leads to a different Stark shift of the hyperfine splitting Δ_hyp. A combination of an `E`-dependent detuning and a non-reversing magnetic field can thus lead to a false eEDM. We minimise the effect of this systematic error by introducing a `PI` switch, which changes ϕ_rf between ϕ_0 and $\phi_0 + \pi$, where ϕ_0 is an arbitrary phase. Doing so ensures that the Ramsey term averages to zero over a block. Furthermore, we randomise ϕ_0 between blocks so that the long-term average of the Ramsey term also vanishes.

Apart from the Ramsey term, another potential source of systematic error arises from the rotation of the polarisation direction between the two rf pulses, $\Delta\theta_\mathrm{rf}$, as it directly adds to the interferometer phase. A change in the electric field direction could lead to slightly different rf transmission line properties which can lead to a different $\Delta\theta_{\mathrm{rf}}$, giving an `E`-dependent phase which appears as an EDM signal. This was already observed in the past when the rf was coupled strongly to the high-voltage lines that generated the electric field, and although this has been suppressed by the methods discussed in [85], the systematic effect remains difficult to characterise because $\Delta\theta_{\mathrm{rf}}$ is indistinguishable from the Zeeman phase due to a background magnetic field.

3.4.2. Hardware and apparatus

The interferometer region is surrounded by three passive magnetic shields, one of which is inside the vacuum chamber and pictured in Fig. 3.7. A pair of electric field plates provide a uniform electric field $\mathbf{E}$ along the z-axis. These field plates were originally a gold-tape-on-glass design [86], but these were replaced with the previous gold-coated aluminium plates [84] in June 2018. We will explain the reason for this change at the end of this section. Two current coils, attached to the magnetic shield, are set up in a Helmholtz configuration to apply a uniform magnetic field $\mathbf{B}$ along the z-axis. A pair of parallel aluminium plates serves as an rf transmission line [84], which enables us to apply an oscillating magnetic field directed along the x-axis to the molecules anywhere within this region. We also have several magnetometers placed around the interferometer region, which we discuss in detail in Section 3.6.

The main hardware used to generate the required fields is shown in Fig. 3.8. The high voltage used for the electric field is generated by a pair of unipolar *Applied Kilovots* supplies. A bleed box enables the field plates to be discharged to ground; this is done when reversing the direction of the electric field. The reversal is done automatically by a set of relays [104]. A set of rf chokes are placed close to the machine and these suppress coupling of rf into the high voltage lines [85]. We monitor leakage currents, another potential source of systematic error, using a set of ammeters that float at high voltage and have nA precision [105] – these are labelled NL (north leakage) and SL (south leakage) in Fig. 3.8 as we conventionally label the two plates North and South. We can manually reverse the direction of the electric field as well by swapping the cables just before the leakage monitors.

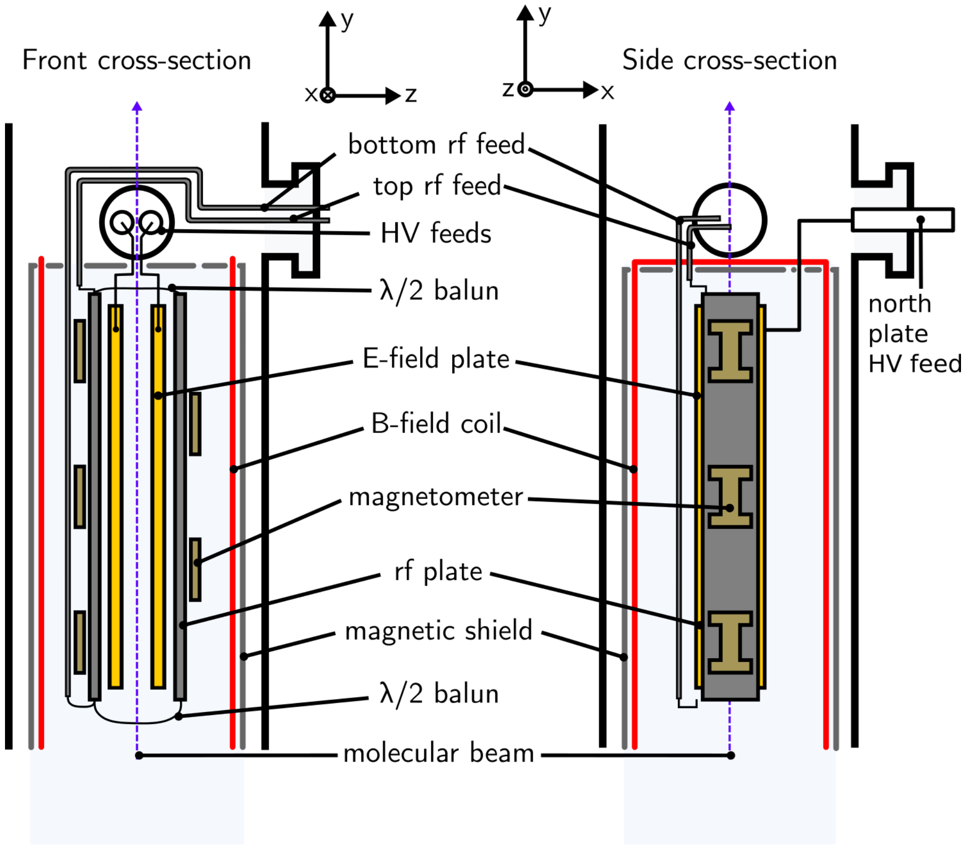

Figure 3.7.: Schematic of the interferometer region of the beam machine.

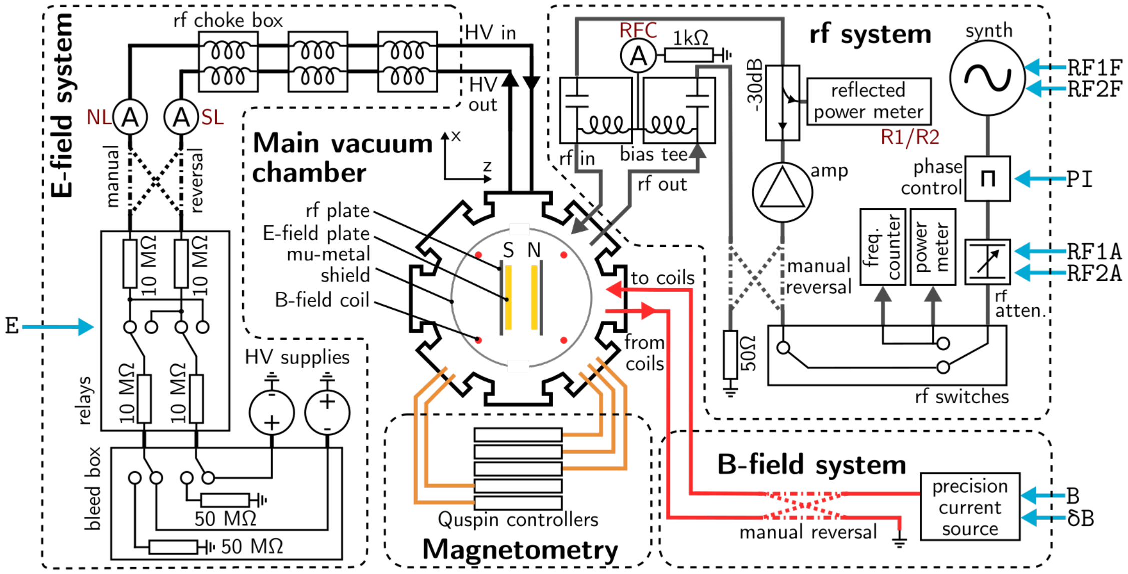

Figure 3.8.: Overview of hardware used to generate the electric field, magnetic field and rf pulses in the interferometer region, and to control the *Quspin* magnetometers. Several switches are shown using blue arrows, and several detectors are highlighted with red text.

The currents that generate the uniform magnetic field are supplied by a home-built precision current source [84], which is able to switch quickly between four current outputs. These correspond to the four different values of the magnetic field we need to run the experiment, which is controlled by the switch states `B` and δ`B`. The magnetic field inside the machine can be switched in less than 350 µs using this current source [84].

The rf is generated by a *HP 8657A* synthesiser. A pair of rf switches control the timings and lengths of the two rf pulses. We are able to control the frequencies of the rf in the two pulses using the onboard DCFM of the synthesiser. The individual pulse amplitudes can be adjusted using a voltage-controlled rf attenuator. The relative phase between the two rf pulses can also be changed using the onboard DCFM and a bi-phase modulator that can apply a π phase change. The first method of changing the relative phase is called the "phase scrambler" and is used to change ϕ_0 between blocks. The second is called the "pi-flipper" and is used to switch `PI`. The resultant rf pulses are amplified and sent to the rf transmission line. We monitor the rf leakage current (RFC) and reflected rf power (RF1/RF2) from the transmission line, which guard against systematic errors arising from rf multipactor discharges and reflected rf power from the high-voltage lines, respectively [85].

3.4.3. Electric field plates

When I first joined the experiment, the electric field plates used were made of glass, with a thin 90 nm layer of gold foil adhered to the surface, as described in [86]. The reason for this design was to have as thin a conductive layer as possible in order to minimise magnetic Johnson noise [106]. The Johnson noise of these glass plates corresponds to an eEDM uncertainty of 1.1×10^{-31} e cm over 4×10^{7} measurements. By contrast, the magnetic Johnson noise of the previously used field plates, which were entirely made of aluminium, is equivalent to an eEDM uncertainty of 1.2×10^{-29} e cm over a dataset of 4×10^{7} measurements [106]. This does not limit the current experiment, which was predicted to have a shot-noise sensitivity of 5×10^{-29} e cm over a dataset of the same size [86], but is not negligible either. However, these aluminium plates are unsuitable for any future experiments such as a laser-cooled fountain of YbF molecules [79], which has a projected eEDM sensitivity at the 10^{-31} e cm level.

The problems with the glass field plates started when we tried to increase the strength of the electric field that can be supported on the plates by a method known as high-voltage conditioning [107]. The voltage applied to the plates was slowly increased in steps of 0.1 kV while reversing the polarity of the plates every minute. A leakage monitor was used to ensure that we stopped the process as soon as we saw any large currents that tended to increase exponentially — a sign of electrical breakdown. Often, current spikes are observed, which we attribute to foreign particles or imperfections on the conducting surface being removed as a result of the discharge. Initial conditioning when the glass plates were first installed resulted in the plates being able to comfortably support an electric field of 8.3 kV cm^{-1} [86].

However, their performance slowly degraded over time. Re-conditioning the plates did not seem to help as any breakdown that occurred caused the plates to deteriorate back to a lower threshold field than prior to the breakdown. We also noticed a low constant leakage current in the region of tens of nA that increased with increasing voltage applied to the plate, which we attribute to field emission [108], often seen as a precursor to breakdown. In March 2018, we could only support an electric field of 3.3 kV cm^{-1}, which would have reduced the polarisation factor by a factor of 2 when compared to running at the desired field of 10 kV cm^{-1}.

After several months of investigation, we eventually found the source of these discharges to be one of the rf plates that was directly behind the electric field plates. As shown in Fig. 3.9(a), the rf plate in question had graphite tape going around the face and edges, which was placed there in order to prevent rf multipactor discharges [85, 86]. The graphite tape around the edges had frayed, causing sharp whiskers of graphite to form. These sharp, conducting edges have high surface charge density, which causes electrons to be easily emitted from such points. When the local electric field is sufficiently high, these points can cause large discharges that damage the extremely thin gold tape we have on the plates. Unfortunately, the damage had already been done to our plates in the form of small tears along the edge of the gold tape where the discharges occurred, as shown in Fig. 3.9(b). This suggests that usual high-voltage conditioning, which works by removing localised charge emitters on the field plates via destructive discharge events, will not work for our gold-taped plates as the tape is too thin.

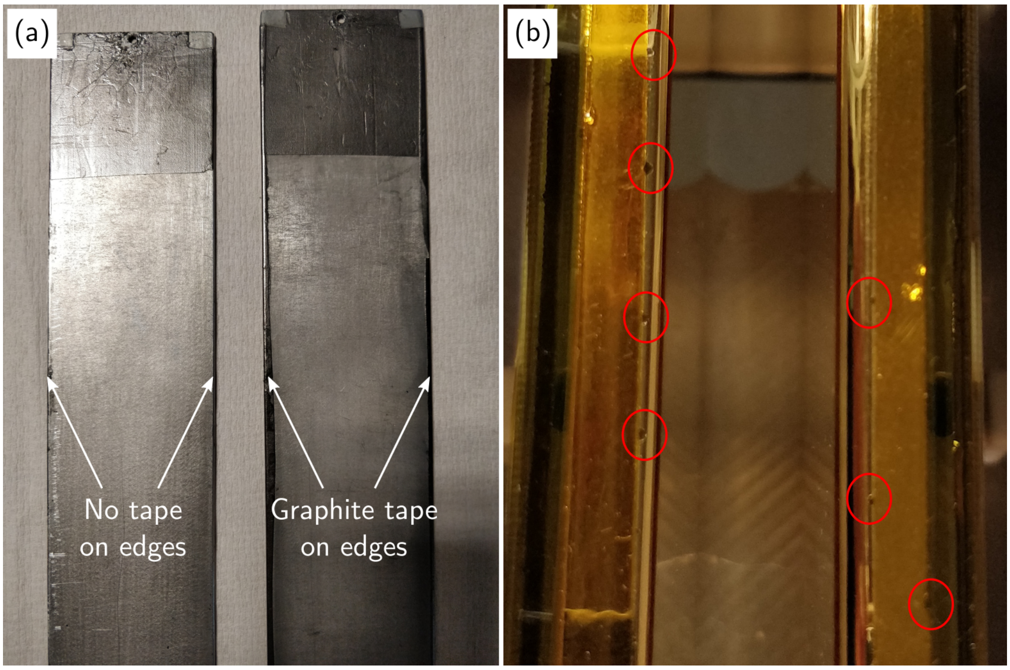

Figure 3.9.: (a) Rf plates, with graphite tape going over the edge of one of them. (b) Edge-on view of the gold-taped glass field plates. The spots where discharge events have damaged the gold tape are circled.

We have removed the graphite tape on the edges of the rf plate and replaced the field plates with the previous gold-coated aluminium plates, measuring 750 mm by 70 mm, which were described in [84][4]. We are now able to support an electric field of ±8 kV with these plates without any significant leakage current, though we usually run at ±6 kV, corresponding to an electric field of $10\,\mathrm{kV\,cm^{-1}}$. Although the gold-tape-on-glass plates have been repaired, it was decided that we continue the experiment with the aluminium plates since the magnetic Johnson noise is not expected to increase the projected sensitivity by more than 10%.

3.5. State detection

After the interferometer region, the molecules in $(N, F) = (0, 0)$ and $(0, 1)$ are detected by coupling either one of the state populations to the $N = 1$ hyperfine levels and

---

[4] The one difference is that the high-voltage feeds are now inserted at the top of the plates instead of the middle.

measuring the fluorescence induced by lasers tuned to the P(1) transition. Using this scheme, each molecule scatters up to 13.9 photons on average and both interferometer quadratures are detected. These are major improvements over the previous method where each molecule scattered about one photon and only one quadrature could be detected [57, 62]. In this section, I will first give an overview of the detector hardware and highlight some results showing the increase in detection efficiency due to optical cycling. Next, I will explain methods that we use to ensure that the detectors are identical. I will then highlight how detector crosstalk was discovered to be a problem and show how imperfections in the detectors lead to reduced interferometric contrast and measurement sensitivity. Finally, I present methods and results from our efforts to maximise the contrast.

3.5.1. Hardware and apparatus

The molecular population in each state is detected in two sequential detectors, which are illustrated in Fig. 3.10. Each detector includes two microwave horns, although only one is used when detecting the molecules. The other horn is included so that the standing wave pattern of the microwave field can be changed, allowing us to test for systematic effects in the experiment. In each detector, we can apply either microwave frequency, so the order of detecting the $F = 0$ and $F = 1$ populations can be reversed to check for systematic effects. The microwaves are generated from the same system as that for state preparation which was described in Section 3.3.

The probe lasers come from a *Toptica DLC TA-SHG pro* solid state system, which combines a seed laser, tapered amplifier and frequency-doubling resonant cavity. This high-power system provides 1 W of 552 nm light. As Fig. 3.10 shows, the laser output is first double-passed through an AOM operating at around 350 MHz, which blue-shifts the light by 700 MHz. The purpose of this AOM is to allow the laser frequency to be stepped by a small amount when taking data – this is a switch in the experiment, which we call `LF1`. To ensure that the optical cycling due to the rotationally-closed nature of the P(1) transition is maximised, we use three probe laser frequencies so that we excite molecules from all of the $N = 1$ hyperfine levels. Thus, the probe laser is split into three components, one of which is unshifted and the other two red-shifted in frequency by 158.5 MHz and 192.1 MHz. These three frequencies address the $F = 1_\ell$, $F = 0/2$ and

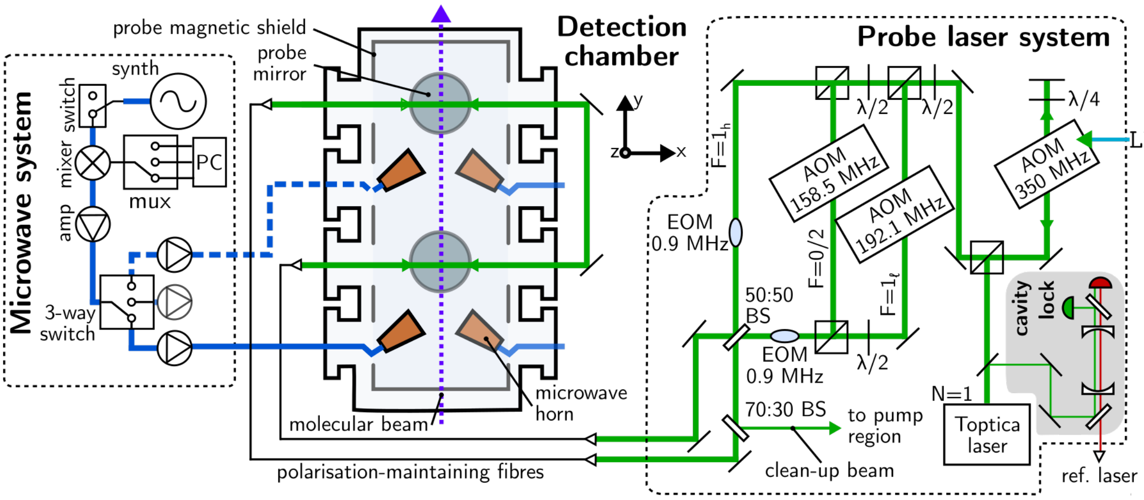

Figure 3.10.: The detection chamber and an overview of the hardware used to generate the lasers and microwaves that are used for state detection.

$F = 1_\mathrm{h}$ components of $N = 1$, respectively, and are combined on a 50:50 beamsplitter, which produces two output beams. One of the output beams is carried by an optical fibre to the upper detector and this same light is routed to pass through the lower detector to ensure some common-mode rejection of fluctuations in the light. A second fibre delivers the second output beam to the lower detector, which counter propagates along the same path. Each beam has a circular Gaussian profile and a $1/\mathrm{e}^2$-radius of 6 mm. The combined peak intensities of the two beams are $80\,\mathrm{mW/cm^2}$, $160\,\mathrm{mW/cm^2}$ and $80\,\mathrm{mW/cm^2}$ for the three frequencies listed above, respectively.

Some of the P(1) transitions have $F \geq F'$, where F, F' are the total angular momenta of the hyperfine states in the ground and excited electronic states. It is well known that if the driving laser has a static polarisation, such a configuration has dark states, which will significantly reduce the number of photons scattered per molecule [109]. We destabilise these dark states by modulating the polarisation of the probe beams between y and z (with circular in between) using electro-optic modulators (EOMs) [86]. We use a rate of 0.9 MHz because our simulations using optical Bloch equations show that dark-state destabilization has a broad optimum around this frequency for various beam intensities, as shown in Fig. 3.11. We also counter-propagate the probe beams as shown in Fig. 3.10 as we found that this also increases the detected photon signal. We hypothesise that counter-propagating the laser beams creates polarisation gradients in the x-direction. The molecules then experience a further varying laser polarisation as they fly through the detection region since they have non-zero transverse velocity.

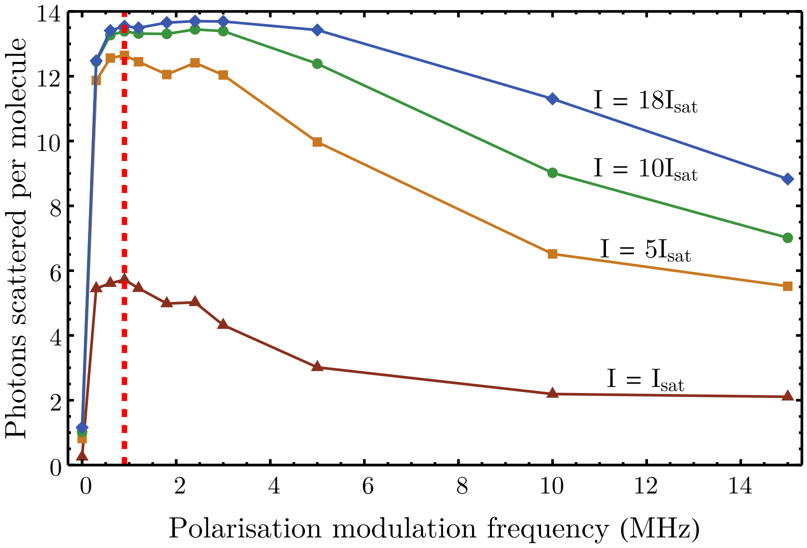

Figure 3.11.: A numerical simulation, using optical Bloch equations, of the number of photons scattered for a molecule that interacts with a Gaussian beam (in one dimension) for different polarisation modulation frequencies and peak beam intensities I. The peak intensities are quoted in units of the two-level saturation intensity for the A–X transition in YbF, $I_{\mathrm{sat}} = \pi hc/(3\lambda^3) = 4.4\,\mathrm{mW/cm^2}$. A molecule traversing through the centre of the detection region would interact with a (one-dimensional) Gaussian beam with peak intensity $I = 18I_{\mathrm{sat}}$, whereas molecules that travel off-axis would interact with beams of lower intensities. The red dashed line shows the frequency of polarisation modulation used in the experiment, which is 0.9 MHz.

The laser-induced fluorescence from the molecules is collected by an aspheric lens on one side of the molecular beam and a large spherical mirror on the opposite side and imaged onto a photomultiplier tube (PMT) by a second aspheric lens. We direct 6% of the scattered photons onto the PMT in this way, and the quantum efficiency of the PMTs at 552 nm is 0.1, thus the overall collection efficiency is 0.6% [85]. With such a high laser power in the detection region, it is imperative that we minimise the background signal due to laser scatter. Although this background can be measured[5] and subtracted away, there is still the increase in uncertainty due to the noise in the laser scatter. We minimise this background in a few ways. As described in [86], the input and output arms of the laser ports were extended outwards by 30 cm away from the main chamber, a scatter-blocking shield was constructed around the detection region, and all the surfaces were blackened using soot from an acetylene flame. Furthermore, we have now also installed

---

[5] This is done by measuring the PMT signal when the molecules are not in the detection region, see Section 3.7.

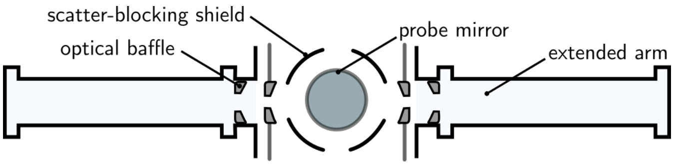

Figure 3.12.: Schematic showing the optical baffles, scatter-blocking shield and extended arms that help reduce the laser scatter in the detector.

several optical baffles along the input and output arms of the laser ports which aim to minimise the amount of off-axis scattering paths available for the lasers, as shown in Fig. 3.12. There are two baffles on each laser port, and the inner baffle which is closer to the machine has an aperture with a smaller diameter (18 mm) than the outer baffle (20 mm). Each baffle is a tapered knife edge, with the wider part of the taper facing towards the centre of the machine. These help increase the acceptance angle of any scattered light directed away from the detection region while minimising the angle for any scattered light directed towards it. We also notice that it is important to use Viton rubber gaskets to connect the main chamber to the extended arms instead of copper gaskets, as the reflective surfaces of the copper that protrude into the machine was found to increase the laser scatter. With these measures, the scatter comes down to about 50 (100) photons in 1 μs in the lower (upper) detection region, equivalent to 5% (10%) of the molecular signal averaged over the time window used in the data analysis. The increase in uncertainty in the measurement due to noise in the laser scatter is then negligible (see Section 4.2.1).

The photoelectron current signals generated by the two PMTs are converted into voltage signals by transimpedance amplifiers, which are then sampled by the data acquisition board. A typical set of time-of-flight (TOF) curves from the two detectors has been shown in Fig. 3.2. We typically integrate these TOF curves to obtain a total photon count, and the dashed lines in Fig. 3.2 indicate the limits used when integrating the TOFs for results presented in this section. For the lower detector these are 200 µs-wide centred on the peak of the TOF curve, and for the upper detector they are about 230 µs-wide[6] to account for the added spread in the molecular beam pulse due to the velocity distribution of the molecules.

---

[6] This is a factor of L_u/L_ℓ larger than the integration gates for the lower detector, where L_u and L_ℓ are the distance of the source to the upper and lower detectors, respectively.

Table 3.1.: Comparison of signal increase due to detection techniques with that predicted by simulations using optical Bloch equations.

Detection method	Signal increase (experiment)	Signal increase (simulation)	Average number of photons scattered per molecule (simulation)
Single-frequency probe laser	1	1	2.3
Probe laser with sidebands	2.3 ± 0.3	2.0	4.6
Sidebands and polarisation modulation	3.8 ± 0.4	5.2	11.9
Sidebands, polarisation modulation and counter-propagating beams	4.9 ± 0.7	5.2	11.9

3.5.2. Optical cycling

Figure 3.13 shows the improvement in the signal from one of the detectors when we use the methods described above to increase the optical cycling of the molecules. In all the cases, the total laser power is 100 mW. For the counter-propagating case, we have used 50 mW per beam. The results are summarised in Table 3.1, where the optical Bloch equation (OBE) simulations used to theoretically predict the optical cycling efficiency were done by J. Lim following the methods presented in [85]. When sidebands are added to the probe laser, the signal detected increases by a factor of 2.3 ± 0.3, in agreement with our simulations. When we also modulate the polarisation of the probe lasers, the signal detected is a factor of 3.8 ± 0.4 higher than in the single-frequency case. This is lower than the OBE simulation prediction of 5.2, suggesting that the polarisation of the probe light is not being fully modulated after passing through the optical fibres. When the light counter-propagates through the machine (keeping the total power constant), the increase in signal is 4.9 ± 0.7, which agrees with the predicted increase when the dark states are fully destabilised. The OBE simulations show that even with full polarisation modulation, we have yet to reach the maximum. This is due to insufficient interaction time of the molecules with the probe lasers in the detection region. A larger probe beam diameter could have been used, but it would have resulted in an unacceptably large amount of laser scatter in the detectors, and also made it more challenging to image all the signal photons onto the PMTs.

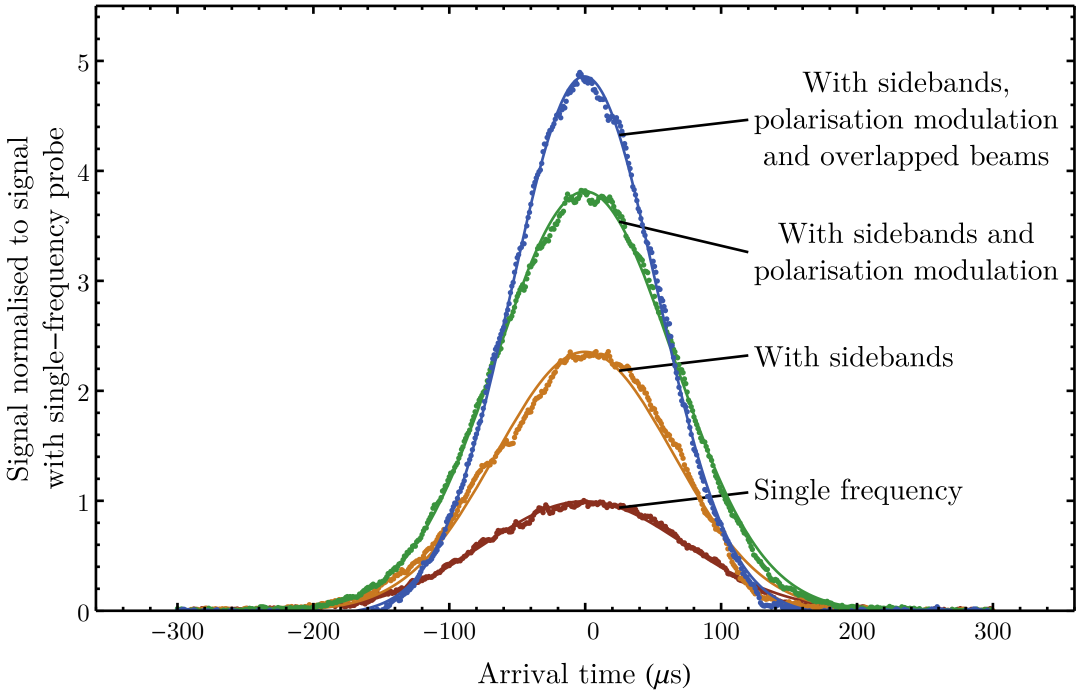

Figure 3.13.: Increase in the detected signal using P(1) detection due to methods that improve the optical cycling of the molecules. The signals are normalised to the peak signal when only a single frequency is used in the probe laser and the backgrounds are subtracted.

The average of 11.9 photons scattered per molecule using this detection method is an order of magnitude higher than the 1.2 photons scattered per molecule using the previous detection method, which simply measured population in one of the ground hyperfine states by optically exciting the Q(0) transition [57, 62]. Moreover, the current detection method allows us to detect both $F = 0$ and $F = 1$ molecules independently, which doubles the number of useful molecules in the experiment compared to the previous detection method, further improving our sensitivity.

3.5.3. Balancing detector efficiencies

Since we are now detecting $F = 0$ and $F = 1$ molecules in separate detectors, we need to ensure that their detection efficiencies are equal. First, we calibrated the lower and upper detector PMTs by operating at a set of (low) light signals and comparing the output

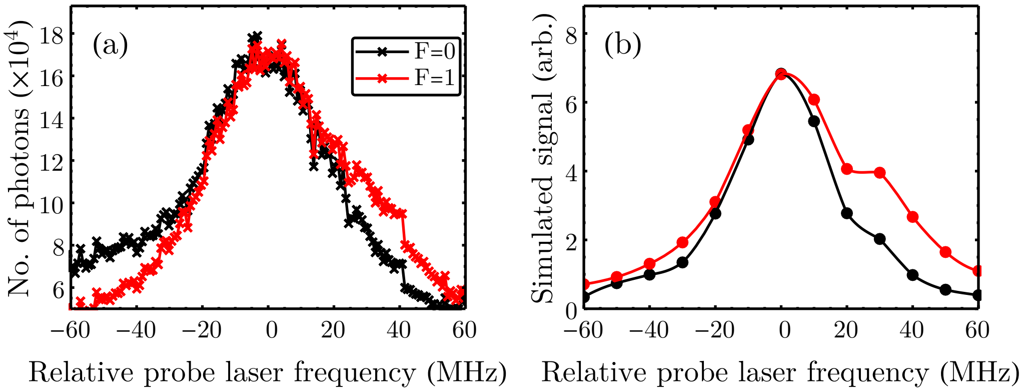

Figure 3.14.: (a) Laser-induced fluorescence observed when scanning the probe laser over the P(1) transition frequency. In the lower (upper) detector, we measure molecular population in $F = 0$ ($F = 1$). For this scan, the populations in both states were equal. (b) An OBE numerical simulation of the dependence of detected signals on the probe laser frequency.

voltage of the transimpedance amplifier with the count rate measured using a pulse discriminator followed by a frequency counter. The result is that for every volt of signal measured, the photon count rate is 510 MHz. Next, we aligned the probe lasers carefully so that the angle with which the probe lasers intersect the molecular beam in the x-z (horizontal) plane is the same in both detector regions. This is because a non-zero angle will cause the k-vector of the photons to have some component along the direction of travel of the molecular beam, resulting in a Doppler shift. A difference in this angle for the two detectors will therefore result in different Doppler shifts and therefore unequal scattering rates. This then gives us a simple way of checking the probe laser beam alignment: by scanning the frequency of the probe laser and detecting the fluorescence. Figure 3.14(a) shows a typical scan taken to ensure that the laser alignment is correct. Here, we have applied an rf $\pi/2$-pulse so that the molecular populations in $F = 0$ and $F = 1$ are equal when the molecules reach the detector region. The lower detector measures $F = 0$ population, and the upper detector measures $F = 1$ population.

The coincidence of the fluorescence peak positions in Fig. 3.14(a) tells us that the lasers are sufficiently well-aligned. The different lineshapes reflect the fact that the microwaves connect molecular population in $F = 0$ and $F = 1$ to different hyperfine states in $N = 1$. For example, the sideband that addresses the $(N, F) = (1, 1_\mathrm{h})$ level is ∼ 30 MHz away from the sideband that addresses the $(1, 2)$ and $(1, 0)$ levels. Since the $F = 1$ detection connects population to $(1, 2)$, we expect that when the probe lasers are blue-detuned

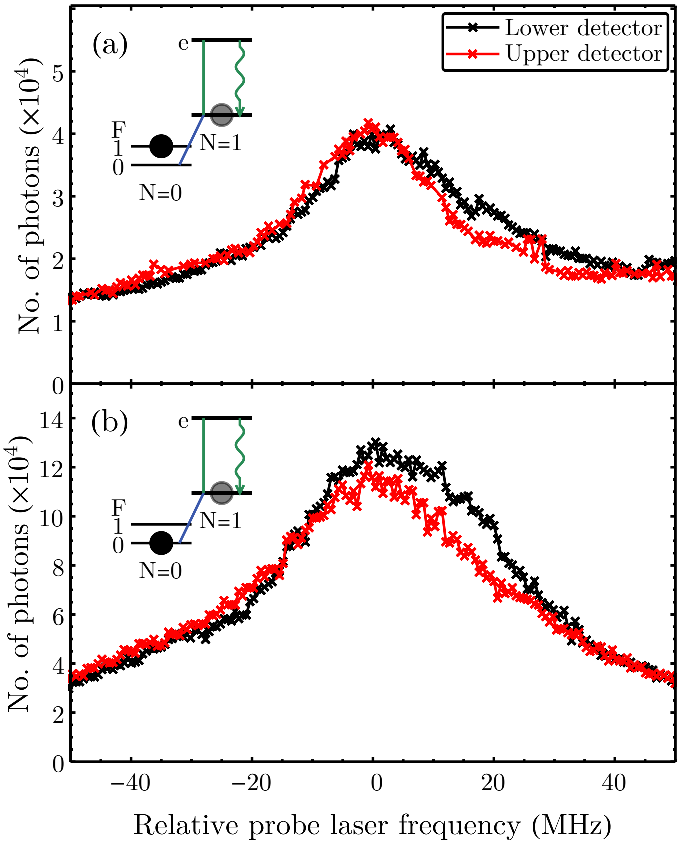

Figure 3.15.: For each scan, only either the lower or upper detector was active, and in both cases the detector was set up to measure $F = 0$ population. (a) Molecular population moved to $F = 1$, so only leftover $N = 1$ population detected. (b) Molecular population remains in $F = 0$, so this and the leftover $N = 1$ population is detected.

by ~ 30 MHz, there would be an increase in the number of photons scattered compared to $F = 0$ detection. This is seen both in the experimental data and the numerical simulations using optical Bloch equations in Fig. 3.14(b).

In order to check how equal the detection efficiencies of the two detectors are, we carry out the same scan as above but measuring $F = 0$ population using only the lower or only the upper detector. The results are shown in Fig. 3.15. In the first panel, the molecular population is moved to $F = 1$ using an rf π-pulse, and we simply detect the leftover population in $N = 1$ from the optical pumping step. The fluorescence peaks coincide, indicating that we are able to detect $N = 1$ population with equal efficiency in both detectors. In the second panel, the molecular population remains in $F = 0$ and we detect this together with the leftover $N = 1$ population. Here, the peak of the fluorescence is smaller in the upper detector by 17% compared to the lower detector. The microwave powers were set to be the same, so this might indicate different resonant properties or different standing wave patterns produced by the microwave horns in the two detectors. As we show later, a small difference in detection efficiencies will not affect the contrast of the interferometer.

3.5.4. Detection crosstalk

A more serious problem arises in the form of crosstalk between our detection regions. An obvious source of crosstalk occurs when the lower detector leaves some population in $N = 1$ which is then detected at the upper detector. We have already discussed above how to destabilise any dark states in $N = 1$ which can contribute to the leftover population. With the $N = 1$ dark states destabilised, we expect that by increasing the probe laser intensity and the microwave power sufficiently, we should be able to pump all the molecules into the higher vibrational states. We investigated this by detecting $F = 0$ population in both lower and upper detectors. The upper detector should not measure any $F = 0$ molecules if we have completely pumped out the molecules in the lower detector. In order to distinguish between $F = 0$ population and other background (such as background from other isotopes), we obtained interference curves by operating the interferometer in the way described at the start of Section 3.5 and scanning the applied magnetic field.

Figure 3.16 shows that as we increase either the laser or microwave power, the amplitude of the interference curve in the upper detector decreases, suggesting that we are able to pump out $F = 0$ better. However, we observe that as we increase the laser or microwave power further, an interference signal returns but with a π phase shift. This signal can only originate from molecular population in $F = 1$, thus indicating that as the laser or microwave power increases, the power broadening increases which then off-resonantly couples $F = 1$ population with the $N = 1$ hyperfine levels. This is plausible since the $(N, F) = (0, 0) \rightarrow (1, 1_\ell)$ and $(0, 1) \rightarrow (1, 2)$ transitions are only 9 MHz apart. Indeed, we confirmed experimentally that the amplitude of the π-phase-shifted interference curve increases when we further increase the powers.

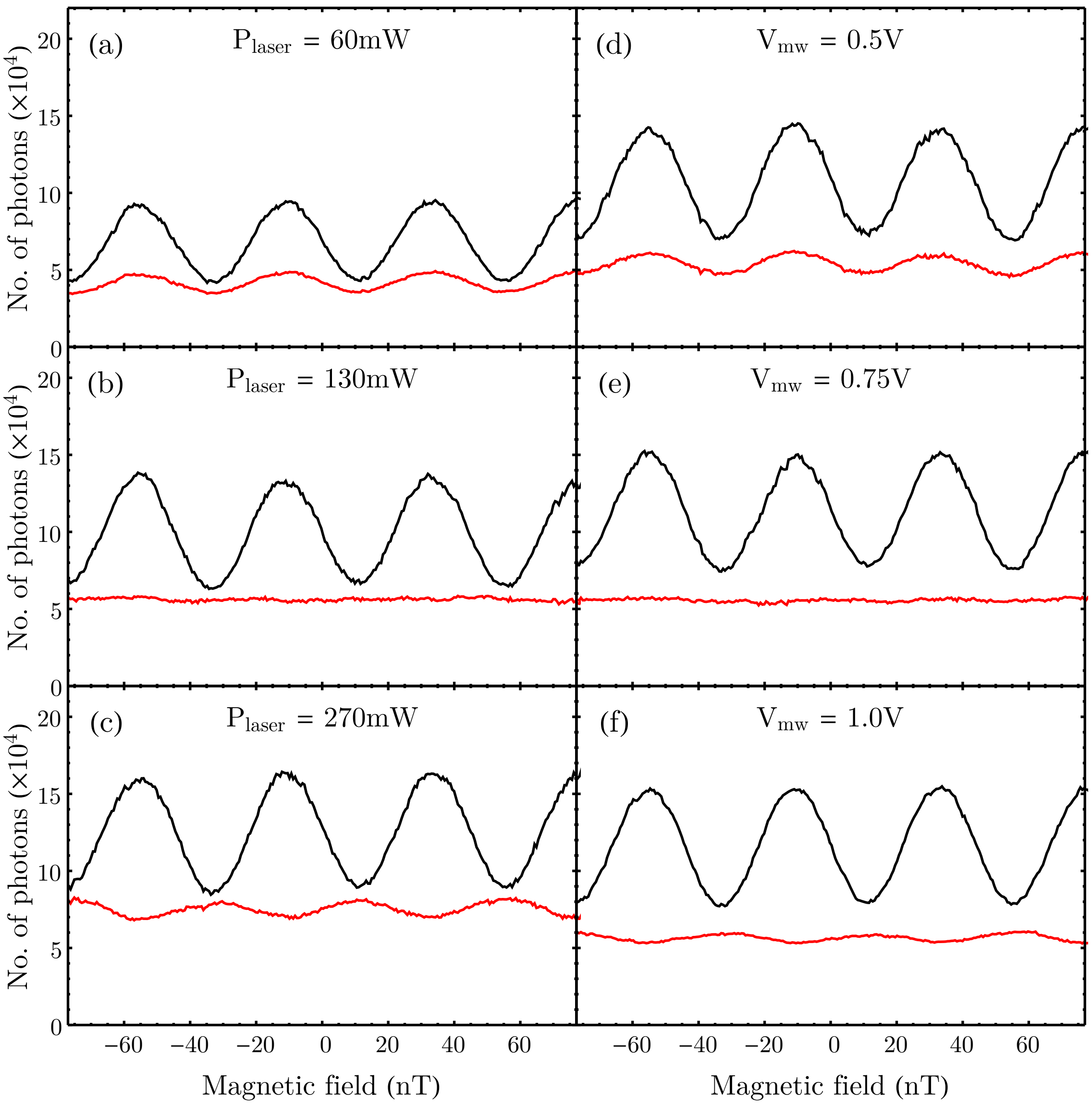

Figure 3.16.: Interference curves obtained by scanning the applied magnetic field. We detect $F = 0$ population in both the lower and upper detectors, shown as black and red lines respectively. For panels (a)-(c), we kept the microwave power constant and varied the total probe laser power P_{laser}. For panels (d)-(f), we kept the P_{laser} constant and varied the microwave power by changing the voltage sent to the microwave mixer, V_{mw}. A higher V_{mw} indicates more microwave power.

Therefore, we have to achieve a compromise between reducing the leftover population (and increasing the number of scattered photons) and minimising this off-resonant coupling of the unwanted hyperfine state in $N = 0$ with the $N = 1$ levels. The best way to do this is to maximise the interferometric contrast. From Fig. 3.16, we can already see that the optimum values for the laser power and microwave mixer voltage are close to 130 mW and 0.75 V respectively.

3.5.5. Maximising contrast

I will first derive the expected signal in the presence of imperfections and show how these imperfections reduce the contrast and therefore sensitivity of the experiment. Let the lower detector be A, i.e. the one that detects population in $F = 0$. First, the optical cycling process does not completely deplete the population in $N = 1$, and so we write the fraction of population left in $N = 1$ after the lower detector as f_{left}. Next, we include the observation that there is some off-resonant driving of the $F = 1$ state when driving the $F = 0$ microwave transition, and vice-versa, and denote the fraction of population that is off-resonantly driven as f_{or}. We account for the difference in detection efficiencies of the two regions by a fraction f_ϵ, so that the detection efficiencies are $(1 \pm f_\epsilon)\epsilon$ in the two regions. In addition to the background due to laser scatter from the apparatus which can be subtracted away, we have another constant background term due to photon scattering from molecules in other states. We represent the latter as a fraction of the total number of molecules, $f_{\text{bg},\ell}$ and $f_{\text{bg,u}}$, for the lower and upper detectors respectively. The measured photon counts can then be written as

$$\begin{aligned} s_{\text{A}} &= N_{\text{mol}}\epsilon A_I(1+f_\epsilon)(\cos^2\phi + f_{\text{R}}\cos\phi + f_{\text{or}}\sin^2\phi + f_{\text{bg},\ell}), \\ s_{\text{B}} &= N_{\text{mol}}\epsilon A_I(1-f_\epsilon)((1-f_{\text{or}})(\sin^2\phi - f_{\text{R}}\cos\phi) + f_{\text{left}}\cos^2\phi + f_{\text{bg,u}}), \end{aligned} \tag{3.7}$$

where we have omitted terms with products of small fractions. Here $f_{\text{R}} = A_{\text{R}}/A_{\text{I}}$ is the Ramsey term amplitude as a fraction of the signal amplitude. The asymmetry, as defined in Eq. (2.19), can now be written as

$$\begin{aligned}
\mathcal{A} &= \frac{s_{\mathrm{A}} - s_{\mathrm{B}}}{s_{\mathrm{A}} + s_{\mathrm{B}}} \\
&\approx \left(\frac{f_\epsilon}{2} + f_{\mathrm{or}} - \frac{3f_{\mathrm{left}}}{4} + f_{\mathrm{bg},\ell} - f_{\mathrm{bg,u}}\right) + 2f_R \cos\phi \\
&+ \left(1 - f_{\mathrm{left}} - f_{\mathrm{or}} - f_{\mathrm{bg},\ell} - f_{\mathrm{bg,u}}\right)\cos 2\phi - \frac{1}{4}\left(2f_\epsilon + f_{\mathrm{left}}\right)\cos 4\phi \\
&\equiv \mathcal{A}_{\mathrm{c}} + \mathcal{A}_{\mathrm{R}}\cos\phi + \mathcal{C}\cos 2\phi + \mathcal{A}_{\mathrm{d}}\cos 4\phi,
\end{aligned} \tag{3.8}$$

where again we have neglected all terms proportional to a product of two or more small quantities. If the order of detecting the molecules is reversed, we obtain a very similar expression to Eq. (3.8).

We have set $\mathcal{C}$ to be the coefficient of the $\cos 2\phi$ term in the expression for $\mathcal{A}$. In addition, there is a constant term $\mathcal{A}_c$, a Ramsey term with amplitude $\mathcal{A}_{\mathrm{R}}$ and a frequency-doubled term with amplitude $\mathcal{A}_{\mathrm{d}}$. The Ramsey component can be removed by methods discussed in Section 3.4, and if all the other imperfections are small, then the $\cos 2\phi$ term dominates. The sensitivity of the experiment depends on how well we can measure a change in $\mathcal{A}$ from a corresponding change in the phase ϕ, which is given by

$$\begin{aligned}
\left|\frac{\partial\mathcal{A}}{\partial\phi}\right|_{\phi=\pi/4} &= \left|\left(-2\mathcal{C}\sin 2\phi - 4\mathcal{A}_d \sin 4\phi\right)\right|_{\phi=\pi/4} = 2\mathcal{C} \\
&= 2\left(1 - f_{\mathrm{left}} - f_{\mathrm{or}} - f_{\mathrm{bg},\ell} - f_{\mathrm{bg,u}}\right),
\end{aligned} \tag{3.9}$$

where we have set $\mathcal{A}_{\mathrm{R}} = 0$ and ϕ is set to $\pi/4$. The sensitivity of the experiment can therefore be maximised by minimising the imperfection terms.

We have already seen that modulating the polarisation of the probe lasers also reduces the leftover population term f_{left}. We have tried to avoid the off-resonant term f_{or} entirely by trying out different detection schemes, such as coupling $(N, F) = (0, 1)$ to $(1, 1_{\mathrm{h}})$ instead of $(1, 2)$ so that when driving this transition we are less likely to off-resonantly drive population from $(0, 0)$ since the microwave transition frequencies are further apart. However, as was shown in [86], the other transitions are too weak for it to be a practical scheme. Recall that increasing the power of the probe lasers and microwaves would also help to decrease leftover population, but we should be careful that any off-resonant driving of the other hyperfine state does not result in an overall decrease in contrast. In

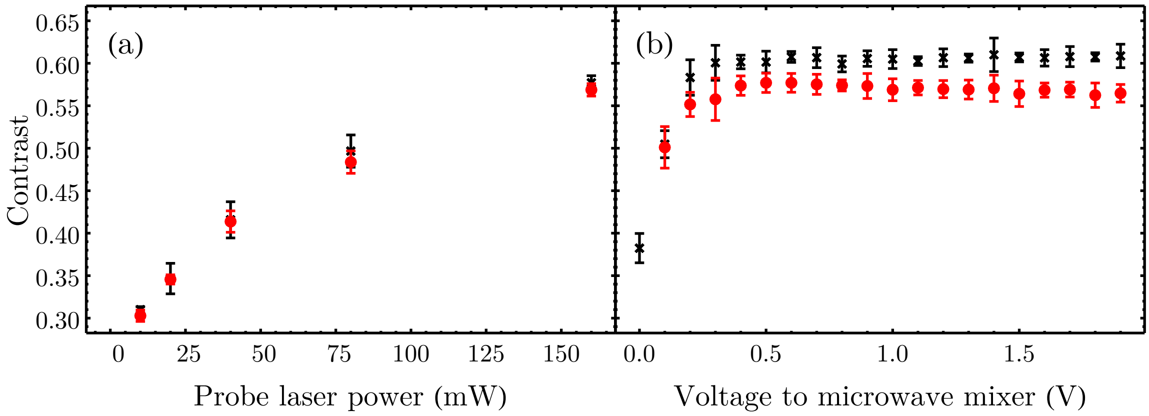

Figure 3.17.: The change in contrast when the probe laser power is varied in (a), and when the microwave power in the detectors is varied via the mixer voltage in (b). The black crosses indicate detection where $F = 0$ ($F = 1$) population is detected in the lower (upper) detector, whereas the red circles indicate detection where the order is reversed.

order to check this, we measured our interferometer contrast while varying the probe laser and microwave powers, and the results are shown in Fig. 3.17. The contrast increases up till our maximum probe laser power of 160 mW and is flat for microwave mixer voltages of more than 0.5 V. We run the experiment at laser and microwave powers of 160 mW and 0.7 V (sent to mixer) respectively[7].

The background scatter from the molecular beam, which is responsible for f_{bg}, mainly comes from two sources. The first source is molecular population in $N = 1$ that remained after the optical pumping step. We show this in Fig. 3.18(a), where we operated the usual optical pumping scheme, but scanned a weak probe laser in the detection region around the ^{174}P(1) transitions[8]. The red data show the spectrum after optical pumping is applied. The important frequencies are the ones shown by the blue dashed lines, since these are the frequencies used in the detection scheme. Any residual population at these frequencies will contribute to the background. We see that there remains a significant amount of population (about 17%) in the $F = 0/F = 2$ hyperfine levels of $N = 1$ in ^{174}YbF.

---

[7] The maximum laser power we have now is 160 mW because the introduction of the 350 MHz AOM in the probe laser system shown in Fig. 3.10 reduced the total amount of power available at the detectors.

[8] Here, we use the superscript to denote the relevant isotope of Yb that the transition refers to.

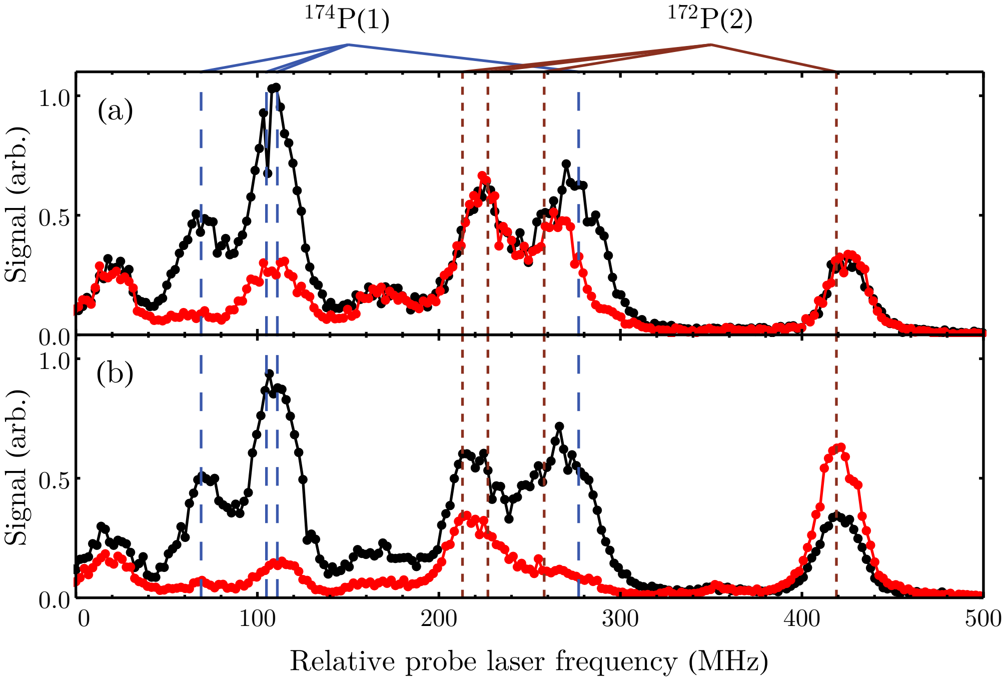

Figure 3.18.: Spectral lines around the ^{174}P(1) transitions, obtained by using a weak probe laser (400 μW) in the detection region. The ^{174}P(1) and ^{172}P(2) transitions are indicated by the dashed lines. The blue dashed lines, labelled ^{174}P(1) are the frequencies used in the detectors, so any remaining population at these frequencies contributes to the background signal. Black: no optical pumping was carried out. Red: (a) regular optical pumping is done; (b) The detection light (^{174}P(1)) was used to pump the molecules, in place of the regular optical pumping, in order to show the origin of the background signal in the detection region.

The other isotopologues of YbF are the second source of background from molecular scattering. We show this in Fig. 3.18(b). In the figure, we note that the ^{174}P(1) lines overlap with the ^{172}P(2) lines, so the latter can contribute to background scatter since our detection method requires high laser power, leading to very large power broadening. The natural abundances of ^{174}YbF and ^{172}YbF are 32% and 22% respectively, so this is a significant source of background. We demonstrate this by applying a pump laser tuned to the ^{174}P(1) transitions (the same laser frequencies as the probe lasers). The $N = 1$ levels are depleted, though not completely, and there are other peaks in the vicinity that are also pumped out. This result shows that the detection light interacts with molecules in other states as well as the $N = 1$ states of interest. These other molecules also contribute to the background we observe in the detectors.

Table 3.2.: Improvements in contrast. We show the contrast for the cases where either $F = 0$ or $F = 1$ population is detected first. Unless stated, the total laser power is 100 mW (if using counter-propagating beams, this corresponds to 50 mW per beam).

	Contrast ($F = 0$ first)	Contrast ($F = 1$ first)
No improvements	0.35	0.37
Clean-up beam (CU)	0.44	0.45
Counter-propagating beams (CP)	0.39	0.40
Polarisation modulation (PM)	0.45	0.43
PM + CU	0.56	0.53
PM + CP + CU	0.58	0.55
PM + CP + CU at 80 mW per beam	0.62	0.61

Table 3.3.: List of experiments used to determine the sizes of the imperfection terms. s_0 is the measured signal due to the $F = 0$ molecules, and is used here to normalise the other quantities.

Experiment	Microwaves in lower detector	Microwaves in upper detector	Signal in lower detector, s_ℓ	Signal in upper detector, s_u
1	None	None	$f_{\mathrm{bg},\ell} s_0$	$f_{\mathrm{bg,u}} s_0$
2	$F = 0$	None	$f_{\mathrm{bg},\ell} s_0 + s_0$	$f_{\mathrm{bg,u}} s_0 + f_\mathrm{left} s_0$
3	$F = 1$	$F = 0$	$f_{\mathrm{bg},\ell} s_0 + f_\mathrm{or} s_0$	$f_{\mathrm{bg,u}} s_0 + (1 - f_\mathrm{or}) s_0$

This background due to other molecules can be minimised by introducing some "clean-up" light into the optical pumping region. As described in Section 3.3, this clean-up light is obtained by picking off a small amount of probe laser light, broadening its frequency spectrum with an overdriven EOM such that its bandwidth is about 200 MHz, and directing this light into the optical pumping region. Since the ^{172}P(2) transitions are not rotationally-closed, whereas the ^{174}P(1) transitions are, we remove the background without adversely affecting the efficiency of the regular optical pumping scheme. In Table 3.2, we show the improvement in contrast after applying the methods described above: (i) polarisation modulation of the probe lasers (PM), (ii) counter-propagating beams in the detector (CP) and (iii) clean-up beam in the optical pumping region (CU). The contrast was measured by fitting interference curves, obtained by scanning the magnetic field, to Eq. (3.8). We have achieved a contrast of $|\mathcal{C}| = 0.62$ for the detector configuration where we measure $F = 0$ population first, and a contrast of $|\mathcal{C}| = 0.61$ for the opposite configuration that measures $F = 1$ population first.

Table 3.4.: Measured imperfection terms for detector configurations where $F = 0$ or $F = 1$ molecules are detected first in the lower detector.

Imperfection term	$F = 0$ first	$F = 1$ first
f_{left}	0.15 ± 0.03	0.19 ± 0.03
f_{or}	0.03 ± 0.03	0.03 ± 0.03
$f_{\text{bg},\ell}$	0.17 ± 0.03	0.20 ± 0.03
$f_{\text{bg,u}}$	0.06 ± 0.02	0.07 ± 0.02

In order to check that we fully understood our detection method, we carried out additional experiments as shown in Table 3.3 to determine the imperfection terms f_{left}, f_{or}, $f_{\text{bg},\ell}$ and $f_{\text{bg,u}}$. In these experiments, the interferometer was not active so all molecular population was in $F = 0$, and the probe lasers were present. The detection microwaves were either absent, or when present they either couple $F = 0$ or $F = 1$ population to the $N = 1$ levels. From the signals written down in Table 3.3, the imperfections terms can be derived as

$$\begin{aligned}
f_{\text{left}} &= \frac{s_{\text{u},2} - s_{\text{u},1}}{s_{\ell,2} - s_{\ell,1}}, \\
f_{\text{or}} &= \frac{x}{1+x} \text{ where } x = \frac{s_{\ell,3} - s_{\ell,1}}{s_{\text{u},3} - s_{\text{u},1}}, \\
f_{\text{bg},\ell} &= \frac{s_{\ell,1}}{s_{\ell,2} - s_{\ell,1}}, \\
f_{\text{bg,u}} &= f_{\text{left}} \frac{s_{\text{u},1}}{s_{\text{u},2} - s_{\text{u},1}},
\end{aligned} \tag{3.10}$$

where $s_{\ell,i}$ and $s_{\text{u},i}$ are the signals from the lower and upper detector in the experiment labelled i. The same experiments were carried out for the case where $F = 1$ molecules are detected by using an rf π-pulse to transfer all the molecules to $F = 1$ before the detection region, and changing the $F = 0$ microwaves in the detection regions to $F = 1$, and vice versa. The results are shown in Table 3.4 and the errors come from shot-to-shot fluctuations in molecule number which we estimate to be about 10%. From these results, we can calculate that the interferometer contrast for the detector configuration where $F = 0$ molecules are detected first is $\mathcal{C}_0 = 0.58 \pm 0.05$, and for the configuration where $F = 1$ molecules are detected first $\mathcal{C}_1 = 0.52 \pm 0.06$. These agree with the measured final contrast values in Table 3.2.

Figure 3.19 shows the interference curves with maximum contrast, with lines representing fits to Eq. (3.8). We have added a phase offset ϕ_{b} to account for the ambient background magnetic field. The fit parameters are shown in Table 3.5, with the fit residuals plotted

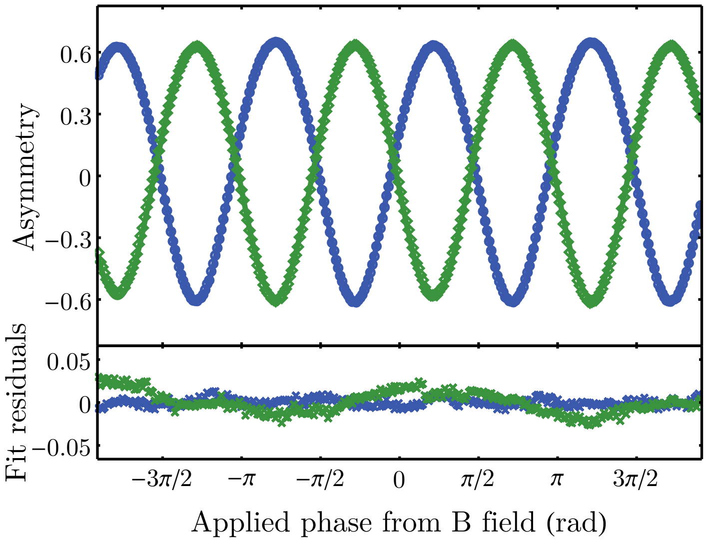

Figure 3.19.: Interference curves obtained by detecting population in $F = 0$ first, then $F = 1$ (blue open circles), and the other way round (green open diamonds). Solid lines are fits to Eq. (3.8), with fit residuals shown below.

Table 3.5.: Fit parameters for the data shown in Fig. 3.19.

Measuring	$\mathcal{C}$	$\mathcal{A}_c$	$\mathcal{A}_R$	$\mathcal{A}_d$	ϕ_b (rad)
$F = 0$ population first	0.623	0.054	-0.012	-0.041	-0.21 π
$F = 1$ population first	-0.609	0.045	0.001	-0.026	0.29 π

as well. The fit residuals for the configuration where $F = 1$ molecules are detected first (in green) show a $\cos\phi$ behaviour. This is due to the Ramsey component which changes for different molecular velocities, while these interference curves are obtained by integrating over all velocities, so there is a residual Ramsey component that is not fit to. In the full experiment, the Ramsey component is averaged to zero, so we will not need to worry about this. The other terms in the asymmetry, $\mathcal{A}_\mathrm{c}$ and $\mathcal{A}_\mathrm{d}$, are small compared to the contrast.

3.6. Magnetometers

The control of ambient magnetic fields is crucial to the experiment because these fields contribute directly to the interferometer phase. We note here that the experiment is only sensitive to the component of the magnetic field that lies along the electric field direction as the effect of the other components are suppressed by the tensor Stark shift of the $F = 1$ levels.

First, random magnetic field noise directly results in phase noise, which reduces the sensitivity of the experiment. We reduce this by enclosing the experiment in three layers of mu-metal shielding and phase-locking the experiment to the mains frequency [85]. As mentioned earlier, although we have reverted to the aluminium field plates, the magnetic Johnson noise generated by these plates should still be negligible for the present experiment. Furthermore, by switching the electric field (see Section 3.7.2), we are able to suppress noise up to the switching frequencies.

Second, any magnetic field that is correlated with the direction of the electric field will generate an `E`-correlated phase, which presents a serious systematic effect. This field can plausibly be generated by leakage currents on the field plates, charging currents that magnetise parts of the inner magnetic shield during an electric field reversal, or an asymmetry in the amount of current drawn by the high-voltage supplies in the two electric field states. Previously, we have placed limits on this systematic by measuring the leakage currents from the field plates and using worst-case models for how the current could flow on the plates [57, 86]. Offline measurements were also carried out to investigate magnetic fields resulting from shield magnetisation that could be caused by charging currents during an electric field switch [85]. However, these are not direct methods of measuring the magnetic field inside the machine, and are often based on pessimistic, worst-case models [85]. Therefore, we decided to install a set of optical atomic magnetometers inside the machine in order to improve our limits on these systematic effects.

The optical atomic magnetometers used are the first-generation zero-field magnetometers manufactured by *QuSpin*. Their operation is described in [110]. Each magnetometer consists of a vapour cell of rubidium atoms and a circularly-polarised laser is used to both optically pump and detect the atoms. In zero field, the rubidium atoms are spin-polarised by the laser and are therefore mostly transparent to the laser. In a non-zero magnetic field perpendicular to the direction of the laser beam, the atoms' spins precess due to the field which causes absorption of the laser. The field strength is then measured by detecting the transmitted laser light. Low-frequency noise is reduced by applying a modulated magnetic field at a known frequency and demodulating the photodetector signal against it.

Atomic magnetometers have become competitive with other forms of magnetometry (such as superconducting devices, known as SQUIDs) due to the realisation of the spin-exchange relaxation-free (SERF) regime. The sensitivity of atomic magnetometers was previously limited by spin-exchange collisions between the atoms. However, as first demonstrated by Happer and Tang [111], when the atomic densities are sufficiently high "the spin-exchange broadening vanishes". The first operational atomic magnetometer using this principle was demonstrated by Romalis and coworkers [112], where a sensitivity of $0.5\,\mathrm{fT}/\sqrt{\mathrm{Hz}}$ was achieved. Similarly, the *QuSpin* magnetometer operates in the SERF regime by increasing the density of rubidium atoms by heating the vapour cell to around 150 °C [110]. These magnetometers have been shown to achieve a sensitivity of $10\,\mathrm{fT}/\sqrt{\mathrm{Hz}}$ in the 1–100 Hz frequency band [110].

These atomic magnetometers were chosen because they did not have any magnetic components which could affect regular operation of the experiment, unlike fluxgate magnetometers. They also do not require cryogenic conditions like SQUID magnetometers do, and are able to achieve sufficient sensitivities for the requirements of our experiment, as will be explained further in this section. Furthermore, their small measurement volume of $27\,\mathrm{mm}^3$ allows some rudimentary mapping of the magnetic field in our interferometer region. I will now explain how we installed these magnetometers and their noise performance, but leave the analysis of their implications for the experimental sensitivity and systematic effects to later chapters.

3.6.1. Hardware

We have installed five of these *QuSpin* magnetometers. The original outer casing of the magnetometers, which had a high outgassing rate in vacuum, was replaced with a

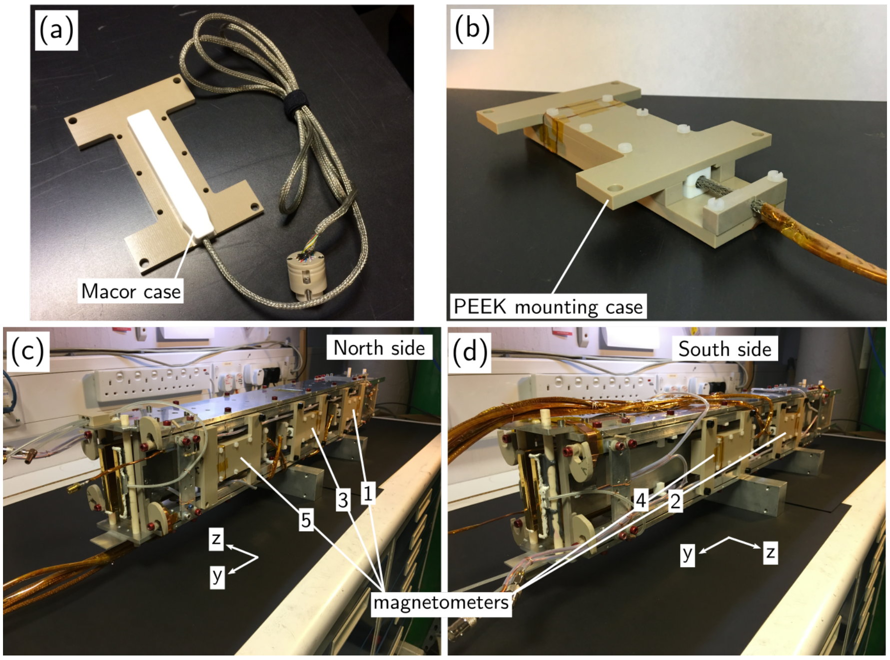

Figure 3.20.: (a) The QuSpin magnetometer in a ceramic Macor case placed in the lower half of the mounting case. (b) The PEEK mounting case that holds the magnetometer securely. (c) Magnetometers mounted on the North side of the aluminium structure holding the plates together. (d) Same as (c) but on the South side. The magnetometers are labelled from 1 to 5 based on their vertical position in the machine.

low-outgassing Macor ceramic casing, which we designed and machined for this purpose. They are as shown in Fig. 3.20(a). We placed the magnetometers in a mounting case made from a polymer called polyether ether ketone (PEEK), shown in Fig. 3.20(b), which allowed us to attach the magnetometers onto the aluminium frame that also held the electric field plates and rf plates. The mounting case was also designed to protect the brittle ceramic cases from being damaged. The magnetometers were placed in a staggered fashion on both sides of the field plates, as shown in Fig. 3.20(c) and Fig. 3.20(d). For ease of reference we will number the magnetometers from 1 to 5 from the bottom to the top of the machine. The magnetometers each have two sensitive axes of measurement which correspond to the y and z axes of our experiment.

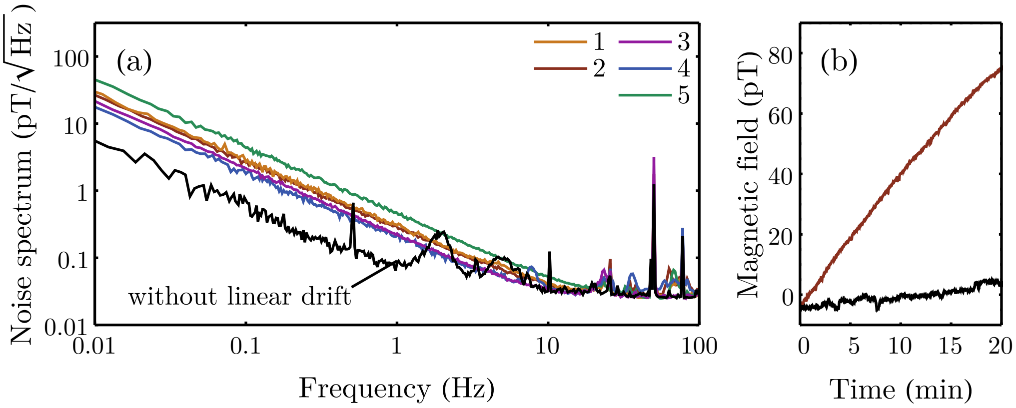

Figure 3.21.: (a) Noise spectra of the magnetometers in the test shield setup. The coloured lines show the spectra before we fixed the linear drift issue. The black line shows the noise spectra of magnetometer 2 after we eliminated the linear drift. (b) Time-series plot showing the output of magnetometer 2 before (red) and after (black) fixing the linear drift.

3.6.2. Magnetic field noise

First, we characterised the sensitivity of the *QuSpin* magnetometers to magnetic fields by placing it in a test setup: a three-layer, cylindrical mu-metal shield with end caps. The coloured lines in Fig. 3.21(a) show the noise spectra for the five magnetometers in the test shields. The strong $1/f$ dependence was initially thought to be a characteristic of the magnetometer. Later, it was realised that it was characteristic of a constant linear drift in the magnetometers' output as shown by the red curve in Fig. 3.21(b). This was discovered to be caused by charge build-up on the analog inputs of the data acquisition board, and by grounding these input connectors via 1 MΩ resistors, we were able to remove the linear drift as shown by the black curve in Fig. 3.21(b). The resultant noise spectrum of magnetometer 2 was measured and shown in Fig. 3.21(a), which still displays a $1/f$ behaviour at sub-Hz frequencies, though the noise is lower than before. The noise floor above 10 Hz was found to be 30 fT/$\sqrt{\text{Hz}}$, which is about thrice that of the quoted specifications from *QuSpin*. This may be because the shielding factor of the test shields is not high enough for the remnant magnetic field noise to be below the true noise floor of the magnetometers.

The magnetometers were then installed onto the aluminium structure inside the machine as described above. Their noise spectra were measured and shown in Fig. 3.22. We also

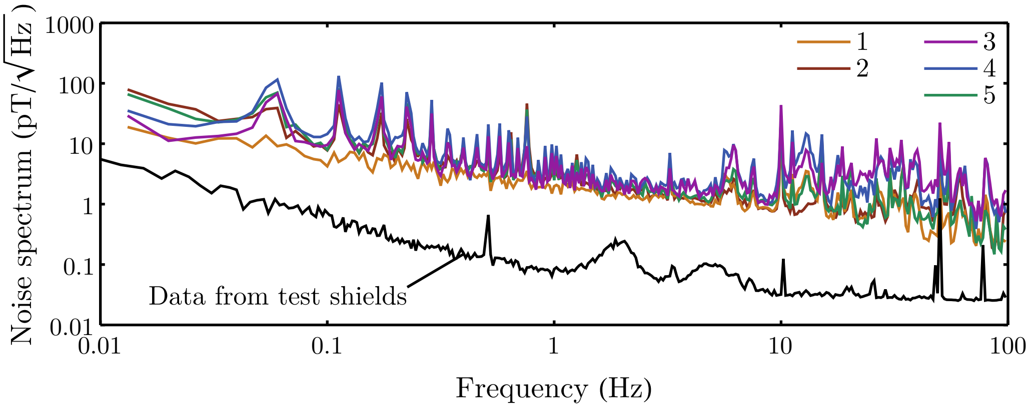

Figure 3.22.: Noise spectra of the magnetometers inside the experiment chamber, shown by the different coloured lines. The black curve is the noise spectrum from magnetometer 2 in the test shields, plotted here for comparison.

plot, in the same figure, the magnetometer noise spectrum inside the test shields for comparison. First, we see that the noise floor is a factor of 10 higher in the main chamber than the test shields. This is to be expected since the radii of the cylindrical magnetic shields of the main chamber are much larger than that of the test shields, and the shielding factor is roughly inversely proportional to the radius of such a shield [113]. We estimate that based on the radii alone, the test shields have a shielding factor 4 times greater than that of the main chamber. Furthermore, the middle and outer shields on the main chamber lack end-caps while the test shields all have end-caps, which would also increase the shielding factor for the latter. Second, there are many peaks present in the noise spectra at sub-Hz frequencies. The origin of these have yet to be investigated.

3.7. Data acquisition and analysis

We have presented an overview of the apparatus used to run the experiment. I will now discuss how a full eEDM measurement is carried out.

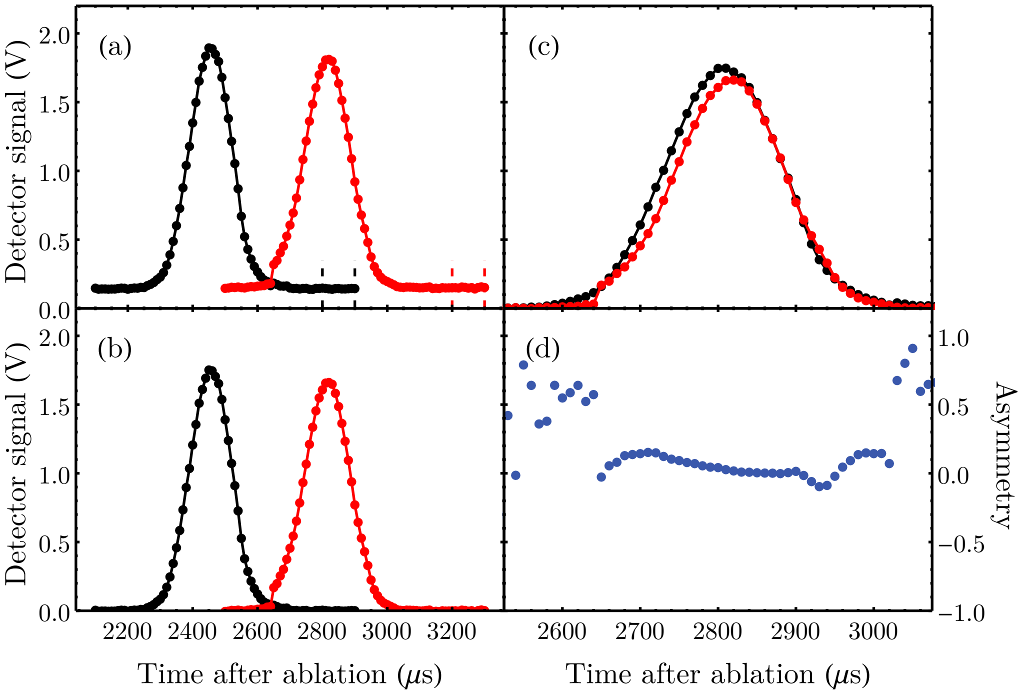

Figure 3.23.: (a) The time-dependent detector signals for the lower (black) and upper (red) detectors, $s_\ell(t)$ and $s_\mathrm{u}(t)$. The laser scatter backgrounds b_ℓ and b_u are obtained by averaging the signals between the dashed lines. (b) The background-subtracted detector signals, $s'_\ell(t)$ (in black) and $s'_\mathrm{u}(t)$ (in red). (c) The stretched lower detector signal, $s'_\ell(t')$, along with the upper detector signal. (d) The time-dependent asymmetry signal, $\mathcal{A}(t)$.

3.7.1. Detectors

For each experimental shot, we record data with several detectors. We distinguish between two types of detectors: single-point detectors and time-dependent detectors. Single-point detectors record only one value per shot, whereas time-dependent detectors record a series of points during a certain time interval. The PMTs for the lower and upper molecule detectors are examples of time-dependent detectors, where the time interval is defined so that we only record data when the molecules are flying through the detectors. A list of detectors can be found in Tables 3.6 and 3.7. Most of these detectors have been discussed in earlier sections. It is worth noting that we use the “short” and “battery” detectors as dummy detectors to ensure that the data acquisition board does not introduce any systematic errors in the data.

There are a few detectors listed in the tables which are not actual physical detectors. These are the asymmetry time-dependent detector and the two laser scatter background single-point detectors. Figure 3.23 illustrates how we obtain the signals for these detectors. We start with the PMT signals from the lower and upper molecule detectors, $s_\ell(t)$ and $s_\mathrm{u}(t)$, as shown in Fig. 3.23(a). The laser scatter background detected by each PMT is measured by averaging the signal in the last 100 µs of the signal, when the molecules have left the detection region. These backgrounds, b_ℓ and b_u, are recorded as single-point detectors. They are also subtracted from the PMT signals to give the signals $s'_\ell(t)$ and $s'_\mathrm{u}(t)$ shown in Fig. 3.23(b). The molecules reaching the upper detector at time t arrive in the lower detector at the earlier time $t' = (L_1/L_2)t$, so we calculate the time-dependent asymmetry as

$$\mathcal{A}(t) = \frac{s'_\ell(t') - s'_\mathrm{u}(t)}{s'_\ell(t') + s'_\mathrm{u}(t)}. \tag{3.11}$$

The signal $s'_\ell(t')$ is shown in Fig. 3.23(c). The resultant asymmetry detector signal $\mathcal{A}(t)$, which represents the asymmetry for molecules with different arrival times and hence different velocities, is shown in Fig. 3.23(d).

3.7.2. Blocks, switches, channels

As discussed in Section 2.2.3, in order to obtain a physically meaningful measurement of the eEDM, d_e, we need to obtain eight values of the asymmetry in different switch states. The switch states were defined as (`E`, `B`, δ`B`). In the simple example discussed in that section, a collection of these eight shots is called a *block*, and each block gives a single measurement of d_e. In the full experiment, we switch six other parameters for a total of nine switches, as listed in Table 3.8. This gives $2^9 = 512$ unique switch states. A full experimental block consists of 4096 measurements such that each switch state is visited eight times.

A switch will take on values $+1$ and -1 during a block. The sequence of values for each shot in a block is called its *waveform*, $W_\mathtt{X}$, where `X` represents an arbitrary switch. The waveforms contain an equal number of $+1$ and -1 and are generated before each block according to the partial randomisation method presented in [114]. The waveforms are chosen such that they are all mutually orthogonal and contain sufficient high-frequency

Table 3.6.: Single-point detectors that record a single value per shot.

Detector	Name	Measures
North leakage monitor	NL	Leakage current on cable connected to the North field plate
South leakage monitor	SL	Leakage current on cable connected to the South field plate
Top photodiode	TPD	Power of the probe laser beam from the higher optical fibre
Bottom photodiode	BPD	Power of the probe laser beam from the lower optical fibre
Miniflux 1 magnetometer	M1	Magnetic field along z axis close to high voltage supplies
Miniflux 2 magnetometer	M2	Magnetic field along z axis over the optical table
Miniflux 3 magnetometer	M3	Magnetic field along z axis above the computer and electronics control rack
rf1 reflected power	R1	Power of rf reflected out of machine during first rf pulse
rf2 reflected power	R2	Power of rf reflected out of machine during second rf pulse
Pi-flip monitor	PF	Phase applied by pi-flipper
Valve voltage monitor	VV	Magnitude of pulsed voltage used to drive solenoid valve for the source
Phase lock frequency	PLF	Clock frequency which is phase-locked to the mains
Phase lock error	PLE	Phase error between the mains cycle and the clock cycle
Lower detector PMT background	BLB	Laser scatter background detected by PMT in the lower detector
Upper detector PMT background	TLB	Laser scatter background detected by PMT in the upper detector

components to reject low-frequency noise. The partial randomisation is needed to minimise bias in the measurement due to any reproducible backgrounds. The one exception to this is the waveform for the electric field switch, W_{E}. We impose a 14 s waiting time during an electric field reversal to allow the charging currents to settle [104], and it would be impractical if this were done many times over the course of a block. Therefore, W_{E} is chosen to be relatively slow and is also fixed apart from an overall multiplication by -1, which is randomly applied before each block.

Table 3.7.: Time-dependent detectors that record a series of data points within a defined time interval at a specified resolution.

Detector	Name	Measures	Time interval (µs)	Resolution (µs)
Lower detector PMT	BOT	Laser-induced fluorescence from molecules in the lower detector	2100–2900	10
Upper detector PMT	TOP	Laser-induced fluorescence from molecules in the upper detector	2500–3300	10
Bartington magnetometer	MAG	Magnetic field along z axis between vacuum chamber and middle magnetic shield	700–3500	200
Short	GND	Voltage across a $50\,\Omega$ resistor to ground	700–3500	200
Battery	BAT	Voltage across a 9 V battery	2100–3300	10
rf ammeter	RFC	DC current flowing onto the rf plates	700–3500	100
Asymmetry	ASY	Asymmetry signal calculated from BOT and TOP	2500–3300	10

Table 3.8.: Switches in a block. The meaning of the parameters in the third column can be found in Table 3.10.

Switch name	Description	Step
`E`	Direction of the electric field	$\pm 10\,\mathrm{kV\,cm^{-1}}$
`B`	Direction of the magnetic field	$B_{\mathrm{bias}} \pm 11.2\,\mathrm{nT}$
δ`B`	Small step in magnetic field	$1.4\,\mathrm{nT}$
`RF1A`	Amplitude of the first rf pulse	$a_{\mathrm{rf1}} \pm 5\%$
`RF2A`	Amplitude of the second rf pulse	$a_{\mathrm{rf2}} \pm 5\%$
`RF1F`	Frequency of the first rf pulse	$\nu_{\mathrm{rf1}} \pm 7.8\,\mathrm{kHz}$
`RF2F`	Frequency of the second rf pulse	$\nu_{\mathrm{rf2}} \pm 7.8\,\mathrm{kHz}$
`LF1`	Frequency of the probe lasers	$\nu_{\mathrm{probe}} \pm 0.9\,\mathrm{MHz}$
`PI`	A relative π phase shift between the rf pulses	$\Phi_0 \pm \pi/2$

We can now generalise the definition of a *channel*, first defined for the asymmetry in Eq. (2.24), to other detectors. A channel is just the detector signal that is correlated with a particular combination of switches, over a block:

$$\{\mathtt{X}\cdot\mathtt{Y}\cdot\mathtt{Z}\cdots\}_{\mathrm{det}} = \frac{1}{N}\sum_{i=1}^{N}\left(W_{\mathtt{X},i}W_{\mathtt{Y},i}W_{\mathtt{Z},i}\cdots\right)s_{\mathrm{det},i}, \tag{3.12}$$

Table 3.9.: Some interesting channels and their physical interpretations.

Channel	Physical interpretation
$\{\delta\mathtt{B}\}$	Slope of the interference curve at the working points of the experiment, equal to twice the contrast of the interferometer. The value of this channel converts other channels from units of asymmetry to units of interferometer phase.
$\{\mathtt{0}\}$	Average asymmetry offset from zero, indicating imperfections as shown in Eq. (3.8).
$\{\mathtt{0}\}_{\mathrm{BOT}}$	Average PMT signal from the lower molecule detector.
$\{\mathtt{B}\}/\{\delta\mathtt{B}\}$	Phase due to the background magnetic field which is not fully cancelled by B_{bias}.
$\{\mathtt{E}\cdot\mathtt{B}\}/\{\delta\mathtt{B}\}$	The most important channel, whose value is proportional to d_e.
$\{\mathtt{E}\}_{\mathrm{MAG}}$	Magnetic field along z, measured by the Bartington, which reverses with `E`.
$\{\mathtt{E}\}_{\mathrm{NL}}$	Leakage current from the North plate correlated with the electric field direction.
$\{\mathtt{E}\cdot\delta\mathtt{B}\}$	Change in contrast correlated with the electric field direction.
$\{\mathtt{RF1A}\cdot\delta\mathtt{B}\}$	Change in contrast between the stepped values of the amplitude of the first rf pulse. A non-zero value is proportional to the detuning of the centre amplitude, a_{rf1} from the π-pulse condition.
$\{\mathtt{PI}\}$	Proportional to the Ramsey component of the interference curve as shown in Eq. (3.8).

where $N = 4096$ is the number of points in a block, and `X`, `Y`, `Z` are switches. The channel with none of the switches is called $\{\mathtt{0}\}_{\mathrm{det}}$ – this just gives the average detector signal over the block. Since the asymmetry detector and its channels are referred to so often, we will drop the detector subscript when referring to the asymmetry channels. The channels retain the time-dependence of the detector signals if the latter are time-dependent. Some important channels for the experiment are listed in Table 3.9. Note that combinations of time-dependent detector channels also retain their time-dependence.

One key aspect of our experiment is the ability to optimise parameter values from block to block by analysing certain combinations of channels. For example, the combination $\{\mathtt{RF1A}\cdot\delta\mathtt{B}\}/\{\delta\mathtt{B}\}$ is proportional to the detuning of the first rf pulse amplitude from its ideal value, which maximises the contrast. By using the value of this combination of channels as an error signal, we are able to servo the amplitude of the first rf pulse to its optimal value using an integral lock. This is done for six different parameters in our experiment, as shown in Table 3.10. This allows the experiment to be automatically

Table 3.10.: Parameters held constant within a block, but changed between blocks.

Parameter	Description	Servo error channel
a_{rf1}	Centre amplitude of the first rf pulse	$\frac{\{\mathtt{RF1A}\cdot\delta\mathtt{B}\}}{\{\delta\mathtt{B}\}}$
a_{rf2}	Centre amplitude of the second rf pulse	$\frac{\{\mathtt{RF2A}\cdot\delta\mathtt{B}\}}{\{\delta\mathtt{B}\}}$
ν_{rf1}	Centre frequency of the first rf pulse	$\frac{\{\mathtt{RF1F}\cdot\delta\mathtt{B}\}}{\{\delta\mathtt{B}\}}$
ν_{rf2}	Centre frequency of the second rf pulse	$\frac{\{\mathtt{RF2F}\cdot\delta\mathtt{B}\}}{\{\delta\mathtt{B}\}}$
ν_{probe}	Centre frequency of the probe lasers	$\frac{\{\mathtt{LF1}\cdot\delta\mathtt{B}\}}{\{\delta\mathtt{B}\}}$
B_{bias}	Bias z magnetic field used to cancel the ambient background field	$\frac{\{\mathtt{B}\}}{\{\delta\mathtt{B}\}}$
ϕ_0	Relative phase between the rf pulses chosen randomly from $(0,\,10\pi)$	–

optimised and to run continuously for more than a day. Fully automated data-taking is typically only prevented by the unlocking of the laser from the transfer cavity lock, which happens a few times per week.

Most of the channel values are expected to be zero if our experiment is working well. Some notable exceptions include the $\{\delta\mathtt{B}\}$ channel, which we want to maximise since it is proportional to the contrast, and the average PMT signals in each detector, $\{\mathtt{0}\}_{\mathrm{BOT}}$ and $\{\mathtt{0}\}_{\mathrm{TOP}}$. Apart from a few channels like these, a non-zero channel often points to an imperfection in the experiment that could potentially lead to a systematic error.

3.7.3. Clusters and manual state reversals

The origin of a non-zero channel can be narrowed down by performing “manual state” reversals. These manual states refer to switches that are performed manually, external to the machine. We have encountered some of these already in Fig. 3.8: we can reverse the connections between the field plates and the high voltage supplies, the connections between the magnetic field coils and precision current source, and input and output cables that deliver the rf pulses. The manual states are represented by booleans $M_{\mathtt{E}}$, $M_{\mathtt{B}}$ and $M_{\mathtt{RF}}$ respectively, where they are either $+1$ (true) or -1 (false). A detailed description of what these manual states refer to can be found in [84, § 3.5]. A new, fourth manual reversal switches the order in which we detect the molecules in the detector; this is done by switching the order of the microwave frequencies produced by the *Anapico* synthesiser. We call this manual state $M_{\texttt{MW}}$, and it is *true* when we detect $F = 0$ molecules in the lower detector, and $F = 1$ molecules in the upper detector, and *false* when their order is reversed. By reversing these manual states and observing the behaviour of the non-zero channels, we can often deduce whether the latter is caused by something inside the main chamber or outside it (more precisely, before or after the point where we perform the manual reversal).

A set of blocks taken continuously with the same set of manual states is called a *cluster*. Thus, channel values for blocks in each cluster are usually signed by the appropriate manual state. For example, the channel containing the eEDM value, $\{\texttt{E} \cdot \texttt{B}\}$, is signed by $M_{\texttt{E}}$, $M_{\texttt{B}}$ and $M_{\texttt{MW}}$, while the contrast channel $\{\delta\texttt{B}\}$ is signed only by $M_{\texttt{MW}}$.

3.8. Summary

In this chapter, I have given a comprehensive overview of the eEDM experiment in its current form. During my time with the experiment, I replaced the electric field plates, refined the detection scheme and proposed and implemented the techniques used to maximise the contrast of the interferometer. I also modified the data acquisition and analysis to accommodate the new detection scheme. Finally, I installed and characterised the optical atomic magnetometers. In the next chapter, I will discuss how we have overcome various sources of noise in the experiment in order to attain an experimental sensitivity close to the shot-noise limit.

4. Noise and sensitivity

This chapter focuses on the characterisation and suppression of noise sources in the experiment, in order to fully leverage the gains in sensitivity from the methods described in the preceding chapter. As shown in Section 2.3, the eEDM sensitivity is directly proportional to the uncertainty in measuring the asymmetry, $\sigma_{\mathcal{A}}$, at the interferometer phase $\phi = \pi/4$. We therefore often refer to $\sigma_{\mathcal{A}}$ instead of σ_{d_e} when discussing the effect of noise.

Moreover, we can distinguish between whether the noise we observe is amplitude or phase noise of the interferometer by measuring the asymmetry at different phases. At $\phi = \pi/4$, we are most sensitive to phase noise (although amplitude noise still comes in), whereas at $\phi = 0$ we are only sensitive to amplitude noise. These are referred to as "side-of-fringe" and "top-of-fringe" measurements of the asymmetry noise. However, one can see that at $\phi = 0$, the populations in each of the hyperfine states of the $N = 0$ ground state are very different (in the ideal case, we would detect all the molecules in one detector and none in the other), whereas at $\phi = \pi/4$ the populations are equal. Some properties of the detection, such as the detection efficiency, could depend on the number of molecules in the detection state. Therefore, in order to make a fairer comparison, we instead apply a single rf $\pi/2$-pulse in the interferometer region, which transfers half the population in the $F = 0$ initial state to the $F = 1$ states. The detectors should now detect equal populations in $F = 0$ and $F = 1$, but any noise on the asymmetry is insensitive to the phase since there is no interferometer.

We typically take 1000 consecutive asymmetry measurements (shots) at 25 Hz, and for each shot, we calculate the asymmetry $\mathcal{A}$ by Eq. (2.19), where the photon counts s_{A} and s_{B} are integrated time-of-flight curves over appropriate gates, as we have described when discussing Fig. 3.2. I will now describe the various sources of noise in the experiment.

4.1. Photodetector noise

The photomultiplier tubes used to detect the photons have noise associated with the statistical nature of the secondary electron emission process at each dynode [115]. This increases the variance in the number of photons detected by an excess noise factor F_e: $\sigma^2 = F_e\sigma_{\mathrm{sn}}^2$, where σ_{sn}^2 is the shot-noise limit. For a PMT with equal gain δ across each dynode stage, the excess noise factor can be approximated as $F_e \approx \delta/(\delta-1)$ [115]. The *Hamamatsu R669* PMTs we use have $m = 10$ dynode stages and we operate at a gain of $G = \delta^m = 10^5$. This gives $\delta \approx 3$ and an excess noise factor of approximately 1.5.

We have measured the noise performance of the PMT by measuring typical laser scatter background in each detector. We measure the variance in the number of photons detected in both detectors to be 1.5 times that of the shot-noise variance expected from a Poissonian process, which agrees with the calculated estimate above. By replacing $\sigma_{s_{\mathrm{A/B}}}^2$ with $F_e\sigma_{s_{\mathrm{A/B}}}^2$ in Eq. (2.32) and proceeding with the calculation, one can show that $\sigma_{\mathcal{A}}^2 \approx F_e/\langle s_{\mathrm{T}}\rangle$. Thus, this noise increases the uncertainty in the asymmetry, and therefore that of the eEDM, by $\sqrt{F_e} = 1.2$ above the shot-noise limit.

4.2. Noise due to probe lasers

The probe lasers are central to the detection of the molecules and as such, fluctuations in any of their aspects can lead to noise in our measurement. Here, we investigate four sources of noise related to the probe lasers: the background laser scatter and fluctuations in the laser beam pointing, frequency and power.

4.2.1. Laser scatter background

The laser scatter background comes from the probe laser scattering off the interior surfaces of the detection chamber and being detected by the PMTs. Let b_ℓ and b_{u} be the number of laser scatter background photons detected in the lower and upper detectors. We subtract these backgrounds from the total measured signals $s_{\mathrm{m},\ell}$ and $s_{\mathrm{m,u}}$, as described in Section 3.7.1, in order to obtain the signals $s_{\ell/\mathrm{u}} = s_{\mathrm{m},\ell/\mathrm{u}} - b_{\ell/\mathrm{u}}$. As the signal s_{m} and background b are measured at different times, the background entering s_{m} is a different random variable b' drawn from the same distribution that b was drawn from, so we write $s_{\mathrm{m},\ell/\mathrm{u}} = s_{\mathrm{mol},\ell} + b'_{\ell/\mathrm{u}}$, where s_{mol} is the true signal coming from photons scattering off the molecular beam. We can now write an expression for the variance in the signals s (dropping the ℓ/u subscript temporarily):

$$\sigma_s^2 = \sigma_{s_{\mathrm{mol}}}^2 + \sigma_{b'}^2 + \sigma_b^2 - 2\,\mathrm{Cov}[b, b'], \tag{4.1}$$

where we have assumed the molecular and background signals are independent, but b and b' are not. We find experimentally that $\mathrm{Cov}[b, b'] \approx 0.4\sigma_b\sigma_{b'} = 0.4\sigma_b^2$. We can then define, similarly to the excess noise factor, a "background noise factor" $F_b = \sigma_s^2/\sigma_{s_{\mathrm{mol}}}^2 \approx 1 + 1.2\langle b\rangle/\langle s_{\mathrm{mol}}\rangle$, where we have assumed Poissonian distributions for both b and s_{mol}.

Typically, within the integration gates used in the experiment, this laser scatter background is 7% and 20% of the molecular signal in the lower and upper detectors, respectively. Thus, we find that $F_{b,\ell} = 1.08$ and $F_{b,\mathrm{u}} = 1.24$. Their effect on the asymmetry signal can be similarly derived, and we find that typically $F_{b,\mathcal{A}} \approx 1.23$ (as expected, this is dominated by $F_{b,\mathrm{u}}$). Thus, the increase in the uncertainty $\sigma_{\mathcal{A}}$ due to the laser scatter background is $\sqrt{F_{b,\mathcal{A}}} = 1.1$.

4.2.2. Beam pointing fluctuations

During a systematic investigation of potential noise sources associated with the probe lasers, we discovered that their beam pointing was fluctuating in the z-axis, as shown by the blue curve in Fig. 4.1(a). The fluctuations have a strong frequency component at 14 Hz, which was found to be a mechanical resonance of the optical cage-mount system used to deliver the probe beams to the machine. We also find that the amplitude of these fluctuations is 7 µm as shown by the blue histogram plot in Fig. 4.1(b). We estimate their effect on the asymmetry noise by exaggerating the change in beam pointing and measuring the change in the asymmetry, as shown in Fig. 4.1(c), from which we find that $\sigma_{\mathcal{A},\mathrm{pointing}} = 0.0023$. This is at the same level as the shot-noise-limited asymmetry noise from detecting 2×10^5 photons, which is $\sigma_{\mathcal{A},\mathrm{sn}} = 0.0022$.

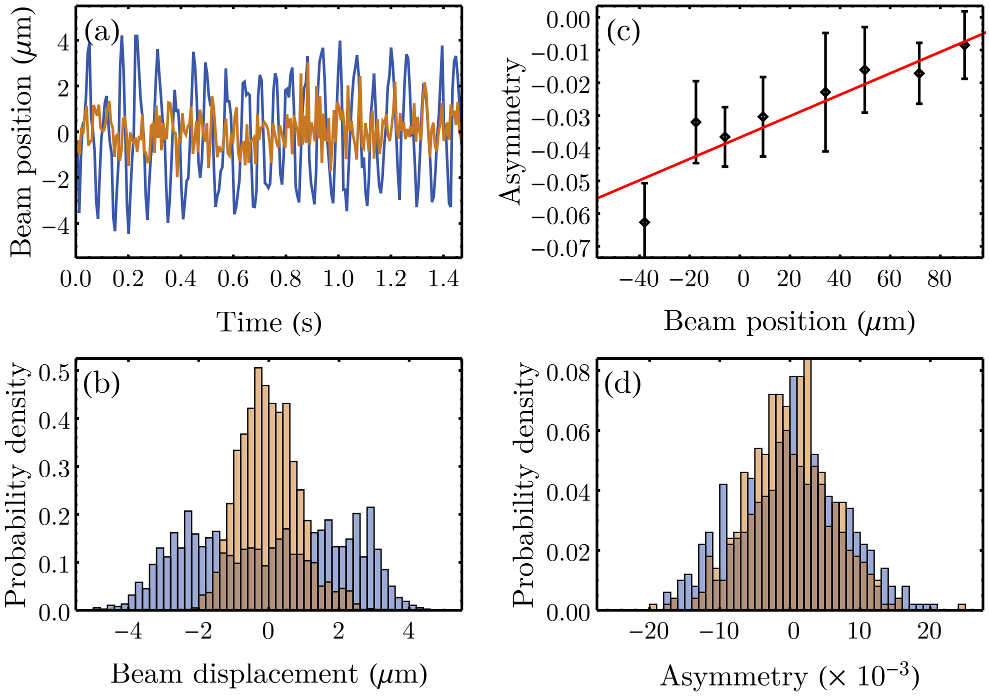

Figure 4.1.: The data in blue and orange represent measurements taken before and after shock-absorbing bushings were installed on the cage-mount system for the probe laser beams. (a) Fluctuations in the beam position along the z-axis. (b) Histograms of the beam pointing fluctuations. (c) The change in asymmetry as a function of greatly exaggerated beam position deviations. (d) Histograms of 1000 asymmetry measurements.

We reduced the beam pointing fluctuations by installing cross-bars with shock-absorbing bushings on the cage-mount posts in order to dampen the mechanical resonances. Their effect is shown by the orange curves in Fig. 4.1(a)-(b), where we have reduced the fluctuations to about 2 μm, corresponding to $\sigma_{\mathcal{A},\text{pointing}} = 0.0006$, which is negligible compared to the shot-noise limit. In Fig. 4.1(d), we plot histograms of 1000 top-of-fringe asymmetry measurements done before (blue) and after (orange) the bushings were installed. We find that the uncertainty in the asymmetry decreased from 0.0074 to 0.0059 after we reduced the fluctuations in the beam pointing.

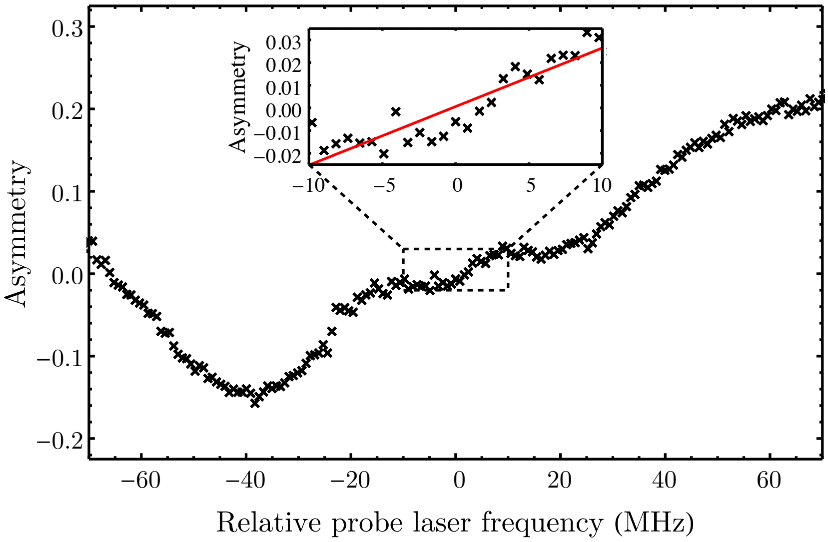

Figure 4.2.: The asymmetry as a function of probe laser frequency. Inset: asymmetry data close to the resonance frequency is fit to a straight line, giving a gradient of 0.0026 MHz^{-1}.

4.2.3. Frequency noise

Fluctuations in the laser frequency can also cause fluctuations in the asymmetry because, as seen in Fig. 3.14, the lineshapes for the signals detected in the two detectors are slightly different. The asymmetry as a function of frequency is shown in Fig. 4.2. We estimate the sensitivity of the asymmetry to laser frequency by fitting a straight line to the data points close to the resonance frequency, as shown in the inset, and find $\partial\mathcal{A}/\partial f = 0.0026\,\mathrm{MHz}^{-1}$. To achieve the shot-noise limit of $\sigma_{\mathcal{A},\mathrm{sn}} = 0.0022$, we therefore have to keep the laser frequency stable to significantly less than 0.8 MHz.

As described in Section 3.3, we lock the lasers to a reference laser which is in turn locked to an atomic transition in Rb by a transfer cavity method. We estimate the frequency noise amplitude to be about 0.7 MHz using the error signal from this locking scheme, so the resultant noise should be a factor of 1.3 above the shot-noise level $\sigma_{\mathcal{A},\mathrm{sn}}$ quoted above. The linewidth of the reference laser is about 0.2 MHz, so the frequency noise can be decreased further by improving the performance of our transfer cavity lock. Currently, we are using a digital implementation of transfer cavity lock: the determination of the transmission peaks' positions and the calculation of the error signals are carried out on a computer. This limits the bandwidth of the lock to about 10 Hz. We can improve

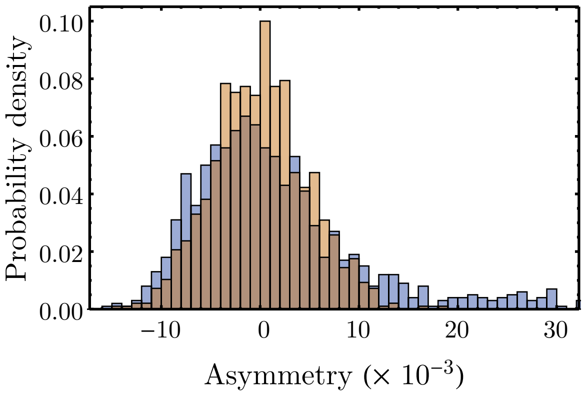

Figure 4.3.: Histograms of “top-of-fringe” asymmetry measurements carried out before (blue) and after (gold) an issue with the reference laser, which was causing larger frequency fluctuations, was corrected.

this by switching to an analog-based implementation of transfer cavity lock, which is currently being tested.

To show how even a small increase in frequency noise can increase the noise in the asymmetry, I show in Fig. 4.3 results from top-of-fringe asymmetry measurements carried out before and after we corrected a problem with the reference laser[1] which increased the frequency noise to a few MHz. After correcting the issue, the noise in the asymmetry decreased from 0.0075 to 0.0049.

4.2.4. Power fluctuations

Finally, to round off the investigation of the probe laser, we tested whether laser power fluctuations could contribute to asymmetry noise. We do not expect this to have a large impact as ideally we are driving the transitions near saturation. Figure 4.4 shows the asymmetry as a function of total probe laser power and a third-order polynomial fit. We find that the gradient at 160 mW, the laser power that we operate at, is $0.000\,26\,\mathrm{mW}^{-1}$. Using a power meter, we find that the fluctuations in the probe laser power are at most 3 mW in size, and so we expect that the fluctuations in laser intensity to contribute negligibly to the asymmetry noise.

---

[1] The problem was that we had accidentally flipped a switch which modulated the current to the diode in the reference laser, which caused the reference laser frequency to be modulated.

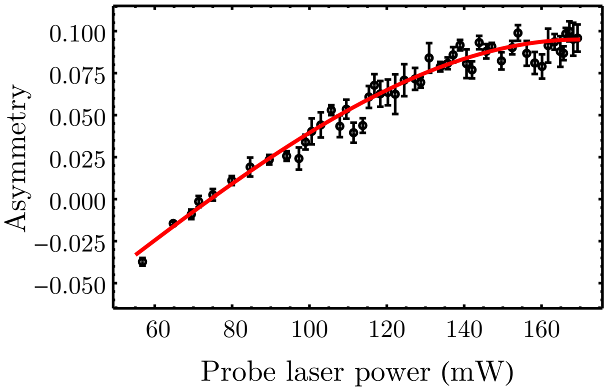

Figure 4.4.: Asymmetry as a function of laser power. The red line is a third-order polynomial fit to the data.

4.3. Magnetic noise

So far, we have mainly discussed sources of amplitude noise on the interferometer. Now, we turn to phase noise caused by fluctuations in the magnetic field. As described in the previous chapter, we reduce the magnetic field noise that the molecules experience by enclosing the experiment in three layers of mu-metal shielding. Furthermore, we phase-lock the experiment to the mains frequency, thus suppressing any magnetic noise arising from the mains. Any further sources of magnetic noise can be tracked down with the help of the newly-installed optical atomic magnetometers, as we shall see.

4.3.1. Turbo pump vibrations

Using the *QuSpin* magnetometers, we found that one large source of magnetic noise was vibrations of the turbo pumps attached to the main chamber. This can be understood as follows: the innermost magnetic shield is attached rigidly to the main chamber, and when the latter vibrates, it causes the magnetic shield (and the dipoles therein) to vibrate as well, which causes the magnetic field inside the chamber to fluctuate.

We measured the chamber vibrations by reflecting a weak laser off one of the windows on the chamber and using a photodiode with a thin slit formed with two knife edges to detect the reflected laser beam. The spot size of the laser beam was larger than the thin

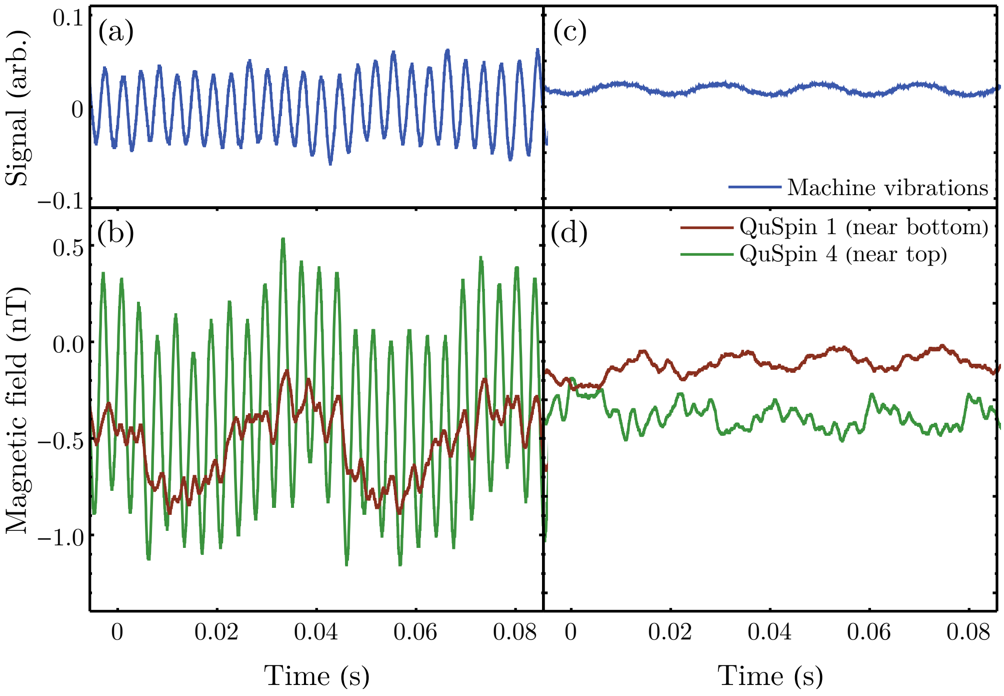

Figure 4.5.: The vibrations of the main chamber before and after the ceramic-bearing turbo was replaced are plotted in (a) and (c). The vibrations were measured using a photodiode and a laser beam reflected off a chamber window, as described in the main text. The magnetic field before and after the top turbo was replaced was measured by two *QuSpin* magnetometers, one placed closer to the top of the chamber, and the other placed closer to the bottom, and are plotted in (b) and (d).

slit, so we were able to detect vibrations by looking at the fluctuations in the detected power. Figure 4.5(a) shows such a measurement – we see a strong oscillation at 278 Hz, which we attribute to a mechanical resonance of the turbo pumps (we confirmed this by spinning down the turbo pumps and the observing the disappearance of these oscillations). Furthermore, we found that the magnetic field measured by the magnetometers, shown in Fig. 4.5(b), also oscillated at this same frequency, in phase with the vibrations of the chamber. The stronger fluctuations seen in the magnetometer near the top of the chamber indicated that the culprit was likely to be the turbo pump attached to the top of the machine. The turbo pump at the top had greased ceramic bearings, whereas the turbo pumps at the bottom (attached to the source chamber) had magnetically-levitated bearings. This led us to replace the former with a magnetic-bearing turbo, which reduced the vibrations and the magnetic noise immediately, as shown in Fig. 4.5(c)-(d).

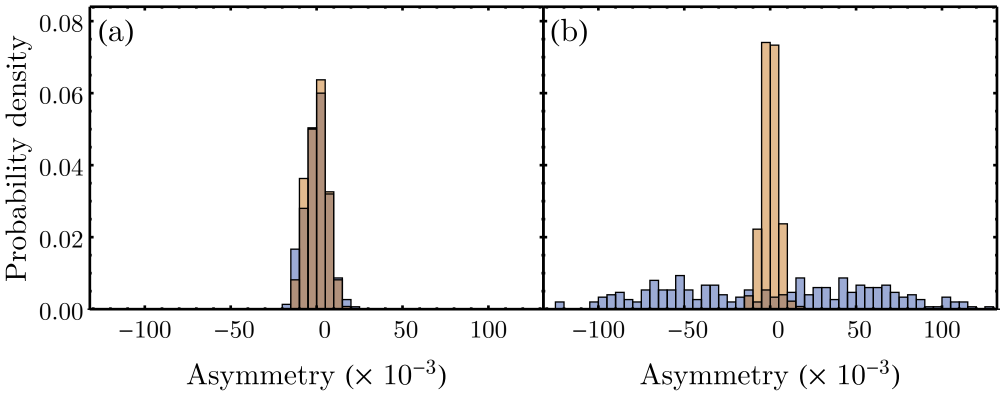

Figure 4.6.: (a) Top-of-fringe asymmetry measurements before (in blue) and after (in gold) the replacement of the ceramic-bearing turbo. (b) Same as (a) but showing side-of-fringe asymmetry measurements instead.

The effect of magnetic noise can be clearly seen in Fig. 4.6, where the top-of-fringe and side-of-fringe measurements of the asymmetry are plotted in (a) and (b), respectively. The blue histograms show asymmetry measurements before the replacement of the turbo, and the gold histograms show the measurements after the replacement. Before the turbo was replaced, the large spread of asymmetry values in the side-of-fringe measurements, but not in the top-of-fringe measurements, indicates phase noise caused by the magnetic field fluctuations. After the turbo was replaced, both types of asymmetry measurements show $\sigma_{\mathcal{A}} \approx 0.005$.

4.3.2. Slow magnetic field noise

In Fig. 4.6, after we had replaced the turbo pump, we see that the side-of-fringe and top-of-fringe measurements of the asymmetry give similar levels of uncertainty. We find that this is about twice as large as the expected shot-noise level, but the excess noise is not dominated by phase noise. From the measurements of the excess noise due to the PMTs, background scatter and laser frequency, we find that we expect to be at 1.7 times the shot-noise limit, which is close to our observations.

Although this is true for the asymmetry measurements, it may not be true when we run the full experiment with blocks, as described in Section 3.7.2. We usually only take 40 s of asymmetry data to determine their noise, whereas the eEDM values are determined from block-to-block, where each block takes about six minutes to complete. Thus, the eEDM measurement is much more sensitive to slow magnetic field noise than the asymmetry measurements. We discuss this in Section 4.5.3 when looking at the sensitivity of the full experiment. However, before that, I will point out a useful method that we have used to identify localised sources of magnetic field inside the machine.

4.3.3. Molecules as magnetic field probes

While searching for magnetic noise sources, we realised that the YbF molecules could also act as magnetic field probes of localised regions in the machine. This could be done because the interferometer region is defined by the times of the two rf pulses, and so we can run experiments where the interferometer region is a short portion of the main chamber, as long as it is within the length of the rf transmission line. Thus, we are able to probe the average magnetic field within such short regions, in effect producing a map of the magnetic field along the length of the interferometer. Similar maps of the electric field uniformity and rf polarisation and amplitude standing wave pattern have been previously demonstrated in our experiment [116], and these also make use of the fact that we can apply these rf pulses anywhere within the interferometer region.

The magnetic field mapping is illustrated in Fig. 4.7. A total of eight overlapping interferometers, each of duration 220 µs corresponding to a distance of approximately 13 cm in the machine, were used to construct the magnetic field maps. For each interferometer, we scan the magnetic field to obtain interference curves, from which we can determine the background field by the phase offset. Since this phase is proportional to the average background magnetic field of the interferometer region, we obtain a moving average of the magnetic field in the entire chamber in this way[2]. Furthermore, within each interferometer measurement, we can time-bin the molecules arriving at the detector and separate them into groups of different velocities. Since the different velocity groups of molecules sample slightly different regions of the interferometer, this allows us to increase the resolution of the field map (although it should be noted that it is still a moving average of the field that is measured).

---

[2] More precisely, it is the magnetic field along the z-direction that we measure.

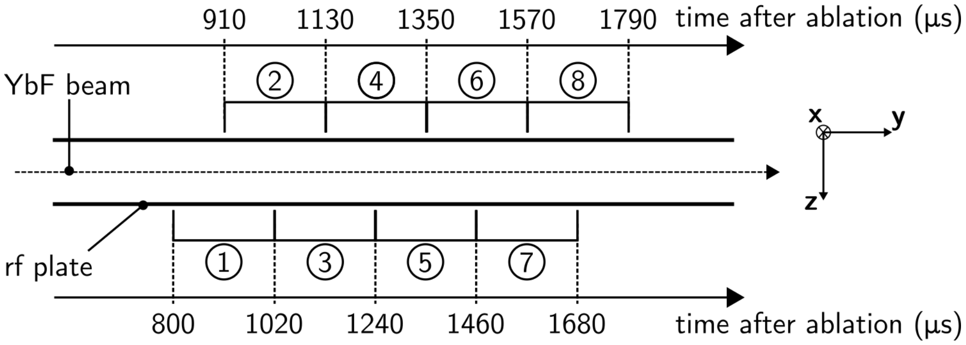

Figure 4.7.: Illustration of the approximate positions of the short interferometer regions, labelled 1 to 8, that we use to map out the magnetic field.

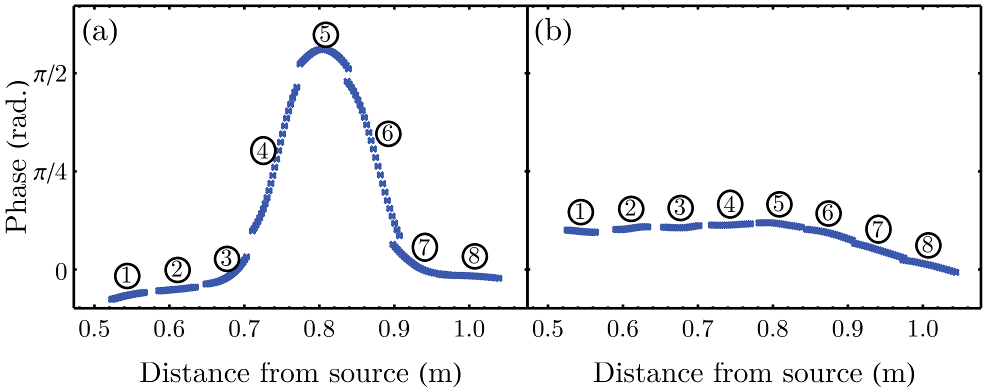

Figure 4.8.: Magnetic field maps of the full interferometer region, where we have labelled the groups of data by the corresponding interferometer as shown in Fig. 4.7. The phase was determined by fitting to the asymmetry interference curve obtained for each point. (a) A magnetic component present in the center of the machine gives rise to a $\pi/2$ phase shift. (b) The field map after the magnetic component was removed, showing no large phase shifts.

The magnetic field map can then be used to search for magnetic components inside the inner magnetic shield. We typically use this method to check for magnetic components after every rebuild of the machine. One example of this is shown in Fig. 4.8, where in (a) we found that the phase of the interferometer changed by almost $\pi/2$ in the center of the machine. This helped us to identify a highly magnetic piece of a drill bit that was embedded in a non-magnetic screw that we used inside the machine. All the screws are vacuum-relieved by drilling through their centers and a shard of a drill bit must have lodged in this screw during this process. When this was later removed, we obtained the graph shown in (b) of the same figure.

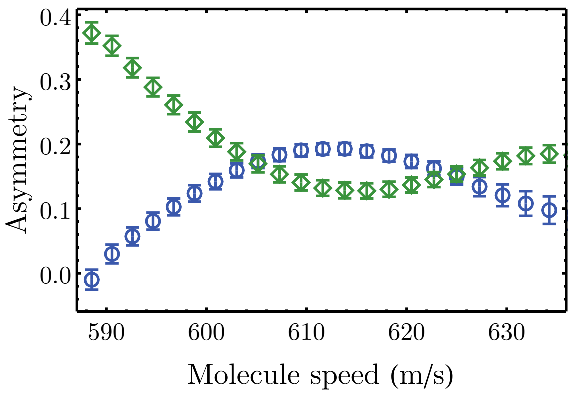

Figure 4.9.: Asymmetry as a function of molecule speed, where we detect population in $F = 0$ first, then $F = 1$ (blue open circles), and the other way round (green open diamonds).

4.4. Molecule source fluctuations

The final source of noise that we considered was fluctuations of the molecule source. At first glance, the asymmetry as defined in Eq. (2.19) should be insensitive to any fluctuations in the number of molecules, N_{mol}. However, various imperfections such as those described in Section 3.5.5 can vary depending on the forward speed of the molecules, which can in turn cause the asymmetry to vary across a single molecular beam pulse. We will first show measurements of this asymmetry variation, before discussing our investigation of how source fluctuations could combine with this and lead to asymmetry noise.

4.4.1. Asymmetry variation with molecule speed

We can quantify the asymmetry variation with molecule speed by binning the detector signals by arrival time. Each time bin corresponds to a narrow group of molecule speeds. Figure 4.9 shows the result of applying this procedure to side-of-fringe asymmetry measurements, where the time bins were chosen to be 10 µs-wide. We show measurements where $F = 0$ population is detected in the lower detector and $F = 1$ detected in the upper detector in blue, and measurements where the detection order is reversed in green.

We can expand Eq. (3.8) around $\phi = \pi/4$ to obtain, for the case where we detect $F = 0$ molecules first,

$$\mathcal{A}(\phi = \frac{\pi}{4} + \delta\phi) \approx \left(\mathcal{A}_{\mathrm{c}} - \mathcal{A}_{\mathrm{d}} + \frac{\mathcal{A}_{\mathrm{R}}}{\sqrt{2}}\right) - \left(2\mathcal{C} + \frac{\mathcal{A}_{\mathrm{R}}}{\sqrt{2}}\right)\delta\phi. \tag{4.2}$$

Similarly, for the case where we detect $F = 1$ molecules first, the asymmetry is

$$\mathcal{A}(\phi = \frac{\pi}{4} + \delta\phi) \approx \left(\mathcal{A}_{\mathrm{c}} - \mathcal{A}_{\mathrm{d}} - \frac{\mathcal{A}_{\mathrm{R}}}{\sqrt{2}}\right) + \left(2\mathcal{C} + \frac{\mathcal{A}_{\mathrm{R}}}{\sqrt{2}}\right)\delta\phi. \tag{4.3}$$

All the parameters in Eqs. (4.2) and (4.3), including the phase deviation $\delta\phi$, have a dependence on molecule speed as shown in Fig. 4.10. The parameter variations were measured by scanning the magnetic field to obtain interference curves similar to those shown in Fig. 3.19. We time-bin the detector signals in the same way as above and for each bin, we obtain an interference curve which we fit to Eq. (3.8) to obtain the parameters.

There are three main reasons for the parameter variations we measure. First, the rf transmission line is not perfect due to an impedance mismatch between the transmission line plates and the semi-rigid coaxial cables that deliver the rf to the plates, causing a standing wave of rf amplitude across the transmission line. Thus, when the π-pulses of rf are applied to the molecules, the π-pulse condition cannot be simultaneously satisfied for all the molecules since their position along the transmission line is different for different speeds. Second, the electric field is also not completely uniform across the length of the field plates. Molecules at different positions therefore have slightly different hyperfine Stark shifts, which cause the rf detuning to vary across the molecular pulse. These two effects combine to cause a variation in the contrast $\mathcal{C}$ and constant term $\mathcal{A}_{\mathrm{c}}$ with molecule speed, shown in Fig. 4.10(a) and Fig. 4.10(c). The Ramsey component $\mathcal{A}_{\mathrm{R}}$, shown in Fig. 4.10(d), can also vary with molecule speed as a result of rf imperfections, although this is less important for the full experiment as we average this term to zero. Third, magnetic field gradients along the length of the interferometer cause molecules of different speeds to sample different magnetic fields in the interferometer, resulting in a variation in the phase of the interferometer as shown in Fig. 4.10(b).

The frequency-doubled term $\mathcal{A}_{\mathrm{d}}$ does not vary much compared to the other terms. Since $\mathcal{A}_{\mathrm{d}}$ depends on f_{ϵ} and f_{left} (see Eq. (3.8)), this suggests that the imperfections related to

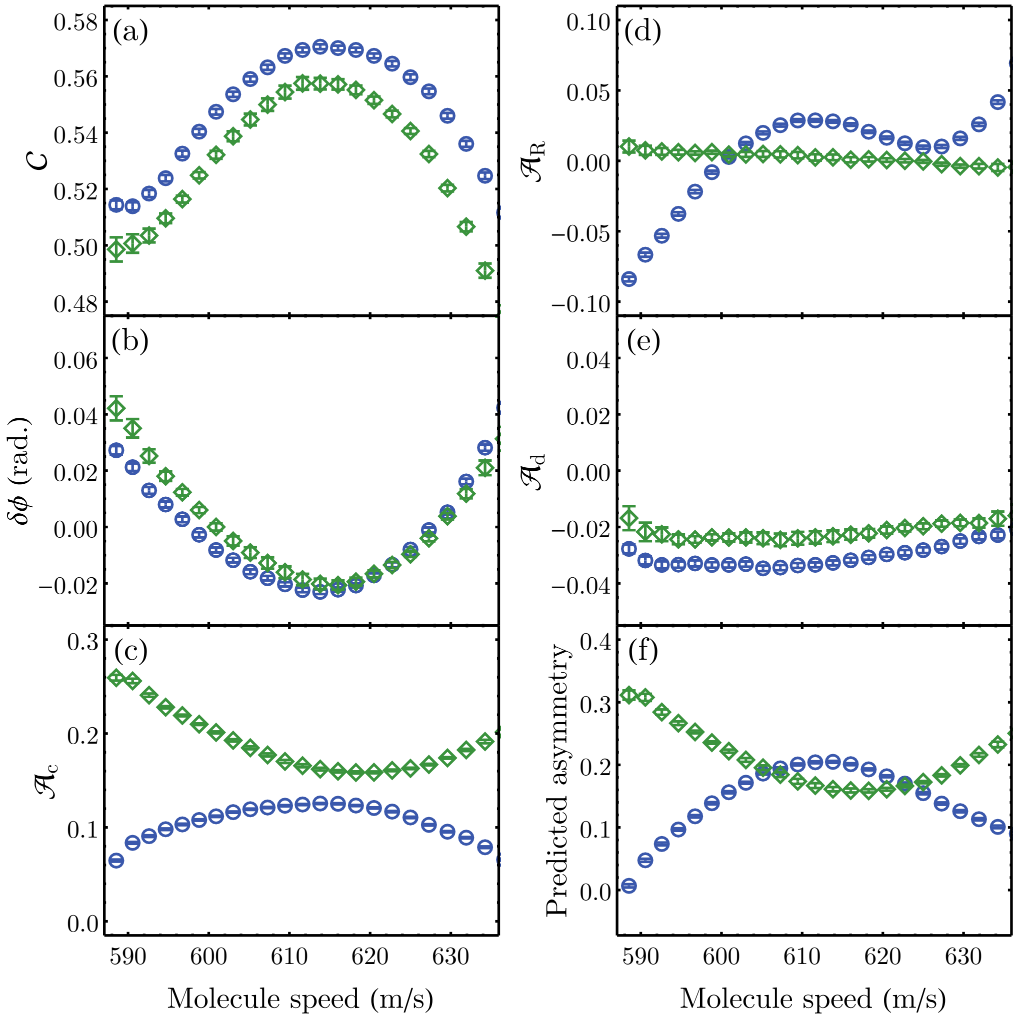

Figure 4.10.: Various parameters, defined in Eq. (3.8), that contribute to the asymmetry, as a function of molecule speed. The data in blue corresponds to the case where we detect population in $F = 0$ first, then $F = 1$, and the data in green corresponds to the reversed detection order. (a) Contrast (b) Phase offset from $\phi = \pi/4$ (c) Constant term $\mathcal{A}_c$ (d) Ramsey term $\mathcal{A}_R$ (e) Frequency-doubled term $\mathcal{A}_d$ (f) Calculated variation in asymmetry from the parameters according to Eqs. (4.2) and (4.3).

the detection efficiency and leftover population do not vary much with molecule speed. This might be expected since these are imperfections in the detector rather than the interferometer, and all molecules regardless of speed should be detected in the same way apart from differences in interaction time with the probe lasers. The latter should be a small effect as we are driving the transitions near saturation. Finally, the variation in asymmetry can be calculated from the parameter variations using Eqs. (4.2) and (4.3), which is shown in Fig. 4.10(f). We see that this agrees with the measured asymmetry variation in Fig. 4.9.

4.4.2. Fluctuations in the speed distribution of the molecule beam

We now discuss how asymmetry variations can combine with fluctuations in the forward speed distribution of the molecule beam, $N_{\mathrm{mol}}(v)$, to produce excess noise. We first consider the asymmetry as a function of molecule speed, i.e.

$$\mathcal{A}(v) = \frac{s_\ell(v) - s_{\mathrm{u}}(v)}{s_\ell(v) + s_{\mathrm{u}}(v)} = \frac{s_\ell(v) - s_{\mathrm{u}}(v)}{\epsilon N_{\mathrm{mol}}(v)}, \tag{4.4}$$

where the dependences of s_ℓ and s_{u} on the speed v are made explicit, and we assume the detection efficiency ϵ is the same for all v, such that $s_\ell(v) + s_{\mathrm{u}}(v) = \epsilon N_{\mathrm{mol}}(v)$. Typically, we integrate the asymmetry over a range of molecule speeds (v_1, v_2):

$$\begin{aligned} \mathcal{A} &= \frac{\int_{v_1}^{v_2} s_\ell(v)dv - \int_{v_1}^{v_2} s_{\mathrm{u}}(v)dv}{\int_{v_1}^{v_2} s_\ell(v)dv + \int_{v_1}^{v_2} s_{\mathrm{u}}(v)dv} \\ &= \frac{\int_{v_1}^{v_2} \left[s_\ell(v) - s_{\mathrm{u}}(v)\right] dv}{\int_{v_1}^{v_2} \left[s_\ell(v) + s_{\mathrm{u}}(v)\right] dv} \\ &= \frac{\int_{v_1}^{v_2} N_{\mathrm{mol}}(v)\mathcal{A}(v)dv}{\int_{v_1}^{v_2} N_{\mathrm{mol}}(v)dv}, \end{aligned} \tag{4.5}$$

where in the last line we have used Eq. (4.4). The final asymmetry is effectively a weighted average of the asymmetries at different speeds, where the weights are given by the number of molecules at that speed. Writing the total number of molecules within the integration gates as $N_{\mathrm{t}} = \int_{v_1}^{v_2} N_{\mathrm{mol}}(v)dv$, we can show that the fluctuations in $\mathcal{A}$ are given by

$$\sigma_{\mathcal{A}}^2 = V_1 + V_2 + V_3 \tag{4.6}$$

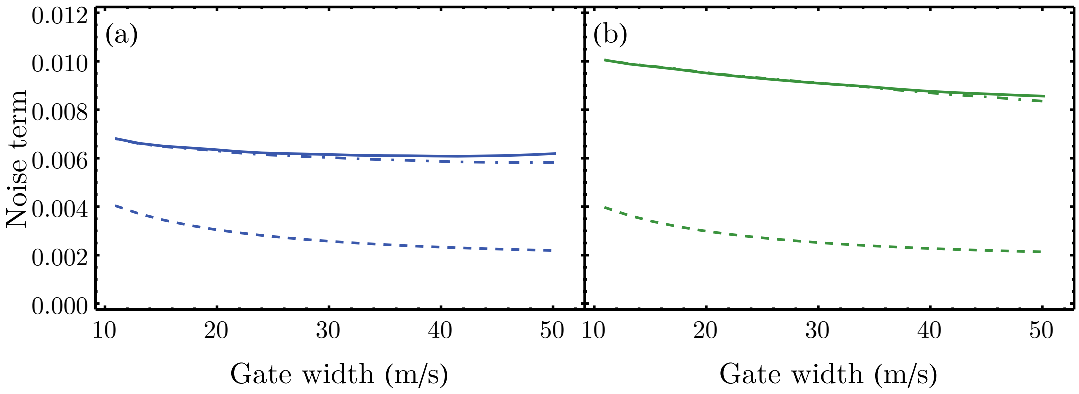

Figure 4.11.: Plots showing the expected shot noise limit (dashed line), "pure" asymmetry noise term $\sqrt{V_1}$ (dot-dash line) and the total asymmetry noise $\sigma_{\mathcal{A}}$ (solid line) as a function of gate width $v_2 - v_1$. All the integration gates are centred on the mean velocity of the molecular pulses, which was $610\,\mathrm{m\,s^{-1}}$ for this dataset. (a) Detecting $F = 0$ first, then $F = 1$. (b) Detecting $F = 1$ first, then $F = 0$.

where

$$\begin{aligned}
V_1 &= \frac{1}{N_\mathrm{t}^2}\int_{v_1}^{v_2} dv \int_{v_1}^{v_2} dv' N_\mathrm{mol}(v) N_\mathrm{mol}(v')\,\mathrm{Cov}[\mathcal{A}(v), \mathcal{A}(v')] \\
V_2 &= \frac{1}{N_\mathrm{t}^2}\int_{v_1}^{v_2} dv \int_{v_1}^{v_2} dv' [\mathcal{A}(v) - \mathcal{A}][\mathcal{A}(v') - \mathcal{A}]\,\mathrm{Cov}[N_\mathrm{mol}(v), N_\mathrm{mol}(v')] \\
V_3 &= \frac{2}{N_\mathrm{t}^2}\int_{v_1}^{v_2} dv \int_{v_1}^{v_2} dv' N_\mathrm{mol}(v)[\mathcal{A}(v') - \mathcal{A}]\,\mathrm{Cov}[\mathcal{A}(v), N_\mathrm{mol}(v')].
\end{aligned}$$

The term V_1 is the contribution to the noise when there are no shot-to-shot fluctuations in $N_\mathrm{mol}(v)$, which can be viewed as noise coming purely from fluctuations in the asymmetry. The term V_2 is the noise due to the shot-to-shot fluctuations in $N_\mathrm{mol}(v)$ which encompasses both fluctuations in the absolute number of molecules and changes in the distribution (i.e. the relative number of molecules at different velocities v). The term V_3 contains the covariance between the asymmetry and molecular beam fluctuations. If the asymmetry was independent of the molecule speed, then V_2 and V_3 vanish (since $\mathcal{A}(v) = \mathcal{A}$) and the noise becomes independent of source fluctuations.

The total noise $\sigma_{\mathcal{A}}$ and its "pure" asymmetry contribution $\sqrt{V_1}$ are plotted as functions of integration gate width $v_2 - v_1$ in Fig. 4.11, where the gates are centred on $610\,\mathrm{m\,s^{-1}}$ (the average centre velocity of the molecular beam pulses). I have also plotted the expected shot noise (see Eq. (2.36)) for comparison. We find that the molecular beam fluctuations contribute very little to the asymmetry noise, although it does seem that they become more important as we integrate over wider gates. The latter can be understood by observing that $\mathcal{A}(v) - \mathcal{A}$ becomes larger towards the wings of the molecular beam pulse, as shown in Fig. 4.9.

4.5. Sensitivity of the full experiment

In the previous sections, we have demonstrated a reduction in the noise down to twice the shot-noise limit in the asymmetry measurements. This noise is likely to be amplitude noise since both side-of-fringe and top-of-fringe measurements show no noticeable difference in the noise. Noise from the PMTs, laser scatter background and laser frequency fluctuations have accounted for most of this excess noise. At this point, we decided to proceed with measuring the sensitivity of the full experiment by taking blocks of data as described in Section 3.7.2.

4.5.1. Analysis methods

From each block, we obtain an arrival-time-dependent EDM channel, $\{\mathtt{E}\cdot\mathtt{B}\}/\{\delta\mathtt{B}\}$, from which we can obtain the eEDM, d_e, according to Eq. (2.26). The PMTs are sampled with a resolution of $10\,\mu\mathrm{s}$, so each point in this channel corresponds to an effective time bin of the same length. We label the EDM at each time bin as $d_e(t_i)$, where $\{t_i\}$ are the (discrete) arrival times. We switch the values of nine parameters, as listed in Table 3.8, over the course of a block. Since a block contains 4096 shots, and there are only $2^9 = 512$ unique machine states, we are able to obtain eight values for each channel in the block. The final channel value is an average over these eight values, from which we can also estimate a standard error for the channel.

There are two averaging procedures to be carried out in order to obtain an estimate of the eEDM, d_e, as well as its associated 1σ-uncertainty, σ_{d_e}, over a dataset of N_b blocks. The first involves estimating the mean across different time bins, and the second involves estimating the mean over different blocks. The two are different because the the first procedure needs to take into account the potential correlations between data over the different arrival times. For example, each molecule spends, on average, 20 µs interacting with the probe lasers in each detection region, which suggests that the data must be correlated on at least that timescale. The second averaging procedure, over different blocks, can be carried out assuming that the data points are independent of each other. These averaging procedures can be carried out in either order, but before discussing these, I will first review some of the statistics we need to deal with potential correlations in the data.

Estimating the mean from correlated data

The following discussion is based on [117]. Let $\{x_i\}, i = 1, \ldots, n$ be a set of n observations with correlations described by a covariance matrix $\mathbf{C}$. An efficient and unbiased estimator[3] of the mean, $\overline{x}$, is obtained by minimising the χ^2-function [117],

$$\chi^2 = \sum_{i,j=1}^{n} (x_i - \overline{x})(x_j - \overline{x}) C_{ij}^{-1}, \tag{4.7}$$

with respect to $\overline{x}$. However, the covariance matrix is often unknown or difficult to estimate. If the variances of the individual data points, σ_i^2, are known, we can instead estimate the mean by taking a weighted average, where the weights are the reciprocals of the variances:

$$\overline{x} = \sum_{i=1}^{n} w_i x_i, \; w_i = \frac{1/\sigma_i^2}{\sum_{j=1}^{n}(1/\sigma_j^2)}. \tag{4.8}$$

If the data were uncorrelated, then the covariance matrix is simply diagonal, $C_{ij} = \delta_{ij}\sigma_i^2$, and Eq. (4.8) is equivalent to minimising the χ^2 of Eq. (4.7). For correlated data, Eq. (4.8) is still an unbiased estimator but is no longer efficient. One can show using simple error propagation rules that the standard error of this estimate is

$$\sigma_{\text{se}} = \sqrt{\sum_{i,j=1}^{n} w_i w_j C_{ij}}. \tag{4.9}$$

We note that for uncorrelated data, this reduces to the familiar form $\sigma_{\text{se}} = (\sum_{i=1}^{n} \frac{1}{\sigma_i^2})^{-\frac{1}{2}}$.

---

[3] An efficient estimator is one that minimises the deviation of the estimate from the true value, whereas an unbiased estimator has an expectation value equal to the true value.

The reduced chi-squared statistic, $\chi_\mathrm{r}^2 = \chi^2/\nu$, is often used to assess how well a certain model fits the data. Here, ν is the number of degrees of freedom. In our case of estimating the mean, there is only one fitted parameter, so $\nu = n - 1$. If we assume uncorrelated data to be our "model", then

$$\chi_\mathrm{r}^2 = \frac{1}{n-1} \sum_{i=1}^{n} \frac{(x_i - \overline{x})^2}{\sigma_i^2}. \tag{4.10}$$

A value of $\chi_\mathrm{r}^2 = 1$ indicates that the model and error estimates σ_i^2 fit the data well. If $\chi_\mathrm{r}^2 > 1$, then the errors are either underestimated, or there are negative correlations between the data points. Conservatively, we can assume the former, which leads us to increase our error estimates $\sigma_i^2 \to \sigma_i^2 \chi_\mathrm{r}^2$. This also has the effect of increasing the weighted error estimate of Eq. (4.9) by χ_r. Conversely, if we have $\chi_\mathrm{r}^2 < 1$, then the errors are either overestimated, or there are positive correlations within the dataset. In this case, if it is likely that correlations are present, we can estimate them by assuming an *ansatz* for the covariance matrix of the form [117]:

$$C_{ij} = \delta_{ij}\sigma_i^2 + f_\mathrm{corr}\sigma_i\sigma_j, \tag{4.11}$$

where we have introduced a constant correlation between the different data points, f_corr. We then solve $\chi_\mathrm{r}^2(f_\mathrm{corr}) = 1$ (with the definition of χ^2 in Eq. (4.7)) to obtain an estimate for f_corr, from which we can make a revised estimate of the weighted mean error using Eq. (4.9).

Averaging procedures

We now return to the issue of obtaining an eEDM estimate from the data. There are two broad methods. (1) We average across the time bins first, obtaining an estimate $\overline{d_{e,j}}$ for the j^th block, and then estimate the mean across the N_b blocks. (2) We find the mean for each time bin over all the blocks, obtaining an estimate $\overline{d_e(t_i)}$ for each time bin, and then average over the time bins.

The first method is more straightforward and I call this Method I. In the j^th block, we have eEDM data $\{d_{e,j}(t_i)\}$ which could be correlated with each other. The covariance matrix cannot be estimated with any confidence since each $d_{e,j}(t_i)$ is obtained only from eight independent measurements. However, the errors associated with each of the time-binned data allow us to use the weighted mean (Eq. (4.8)) to obtain an estimate $\overline{d_{e,j}}$. Next, we can make an estimate of d_e across all the blocks and its standard error by using the bootstrapped 10% trimmed mean [118]. The trimmed mean is used because it is more robust to outliers, and bootstrapping is a random resampling technique used to easily obtain standard errors for parameter estimates even for non-normal distributions [118]. We generate a bootstrap set by drawing randomly from the N_b values of $\overline{d_{e,j}}$ we already have, allowing for the possibility of drawing the same value more than once. We estimate the 10% trimmed mean from this bootstrap set, obtaining a bootstrap estimate of the mean. By repeating this procedure many times (typically 5000 – 10000 repetitions), we build up a distribution for the estimate of the mean. The standard deviation of these bootstrap estimates is the standard error of the trimmed mean of the eEDM.

The second method involves averaging over the different blocks first in order to obtain estimates for the mean in each time bin, $\overline{d_e(t_i)}$. This first step, where we average over the blocks, is carried out using the bootstrapped 10% trimmed mean exactly as it was done in Method I, but for each time bin separately. After this, we combine the time-bin means in one of two ways. The first, which I call Method II(a), is the weighted mean of Eq. (4.8). As we will see later in the results section, the naïve error estimate Eq. (4.9) tends to give $\chi^2_\mathrm{r} < 1$, indicating that positive correlations exist between the different time bins. This can be addressed using the method of parameterising a correlation matrix with f_corr, as discussed in the preceding section, which will give us a better estimate of the standard error on our estimate of d_e.

The second way to combine $\{\overline{d_e(t_i)}\}$ is to extend the bootstrap method of the first step, which I call Method II(b). After we generate the bootstrap set, we estimate not just the trimmed mean for the individual time bins, but also the sample covariance matrix, defined as

$$C(t_i, t_k) = \frac{1}{N_\mathrm{b} - 1} \sum_{j=1}^{N_\mathrm{b}} (d_{e,j}(t_i) - \overline{d_e(t_i)})(d_{e,j}(t_k) - \overline{d_e(t_k)}). \tag{4.12}$$

We can then obtain a bootstrap estimate of the mean of d_e by minimising the χ^2 of Eq. (4.7), using the trimmed means for each time bin as the data points $\{x_i\}$ and $C(t_i, t_k)$ as the covariance matrix. This can again be repeated many times to obtain a set of bootstrap estimates, from which we can determine the standard error of the mean.

Data cuts

We also apply cuts to remove blocks that have a poor signal-to-noise ratio or particularly unstable source flux. First, I apply a "signal cut" which removes all blocks which has a total molecular signal (by adding up the signals from both detectors) of fewer than 5×10^4 photons. The second cut is a "contrast cut", where I remove blocks which have a measured contrast of less than 0.4. For both these cuts, I have varied the thresholds and checked that the mean and error estimates for d_e are consistent.

4.5.2. Results

We obtained three clusters of data, taken between October 2019 and March 2020. A summary of their results is presented in Table 4.1. The first thing to address is the number of blocks omitted from analysis due to the data cuts discussed earlier. The first cluster was taken with "normal" running conditions where the source was in a good condition and the signal was therefore consistently high, resulting in a low number of blocks cut from the final analysis. In contrast, the second and third clusters have poorer molecular signal and so there were a relatively larger number of blocks cut from the final analysis. The reason for this is because after the first cluster of data taken, when we next took data we saw a shift in the value for d_e. As all that had changed was replacing a faulty component in the electronics required for the preparation of the rf pulses, we naturally suspected that the rf had a role to play in this systematic effect. The second and third clusters were taken with different rf manual states, and indeed we see that the value of d_e depends on the rf manual state. However, when we were carrying out this investigation, we were not too concerned with the source condition, thus resulting in a poorer signal overall. This should not be a problem for the actual experiment as the source can be cleaned and optimised following the procedures laid out in Section 3.2.

The systematic effect was investigated thoroughly and we found that there was a small leakage current on the rf plates due to rf multipactor discharge, as was first reported by Devlin [85]. This leakage current can result in magnetic fields which can generate a false EDM. As the required rf pulse amplitudes are different in the two rf manual states, due to the slightly different standing wave that forms when the rf direction is reversed, and

Table 4.1.: Comparison of estimates of the mean and standard error for d_e for three separate clusters, using three different averaging methods. N_b refers to the total number of analysed blocks, excluding the blocks that had been cut from the analysis.

Cluster	N_b	# blocks cut	Method	χ^2_r	$d_e{}^\dagger$	$\sigma_{d_e}\sqrt{N_\mathrm{b}}{}^\dagger$	$\xi^*_{d_e}\sqrt{N_\mathrm{b}}$ †‡
24Oct1902	293	26	I	1.2	-1.1 ± 0.5	7.9	2.5
			II(a)	0.41	-0.9 ± 0.6	9.9	
			II(b)	0.1^*	-0.7 ± 0.5	8.1	
24Feb2004	111	35	I	0.93	4.3 ± 1.4	15	3.2
			II(a)	0.63	4.2 ± 1.3	13	
			II(b)	0.47^*	4.5 ± 1.5	16	
02Mar2010	103	53	I	0.96	-8.3 ± 0.6	6.6	3.1
			II(a)	0.72	-8.3 ± 0.8	7.7	
			II(b)	0.36^*	-8.3 ± 0.6	6.5	

[*] χ^2_r averaged over all bootstrap sets. [†] In units of 10^{-27} e cm.
[‡] $\xi^*_{d_e} = \xi_{d_e}\sqrt{F_e F_{b,\mathcal{A}}}$.

since the level of multipactor discharge is sensitive to the rf power, it is consistent with the fact that the value of d_e changes with rf manual state. As we did not see this effect in the first cluster of data, we can only hypothesise that something degraded within the machine which now causes the discharge. We are currently attempting to locate and minimise the source of this discharge.

I analysed these clusters using the averaging methods described above. The χ^2_r for Method I was consistently close to 1, which confirms that the assumption that data from different blocks are independent. Nevertheless, the standard error estimate obtained from the bootstrapping process was multiplied by $\sqrt{\chi^2_\mathrm{r}}$ in order to obtain our estimate for σ_{d_e}. For Method II(a), we see that the χ^2_r (for the weighted mean error estimate) ranges from 0.4 to 0.7 for the three clusters, and since we know that the data from different time bins could be correlated, it is likely that this is the reason for $\chi^2_\mathrm{r} < 1$. We therefore carry out the procedure to produce a new error estimate as described in Section 4.5.1. In Method II(b), where we minimise χ^2_r using an estimated covariance matrix for each bootstrap set, the χ^2_r shown in Table 4.1 is the average from all the bootstrap sets. The low values for this across all three clusters is indicative of the high degree of correlation between the time-bins in the data; nevertheless I still have confidence that the final error estimate is a good one as it is determined by the spread of bootstrap means.

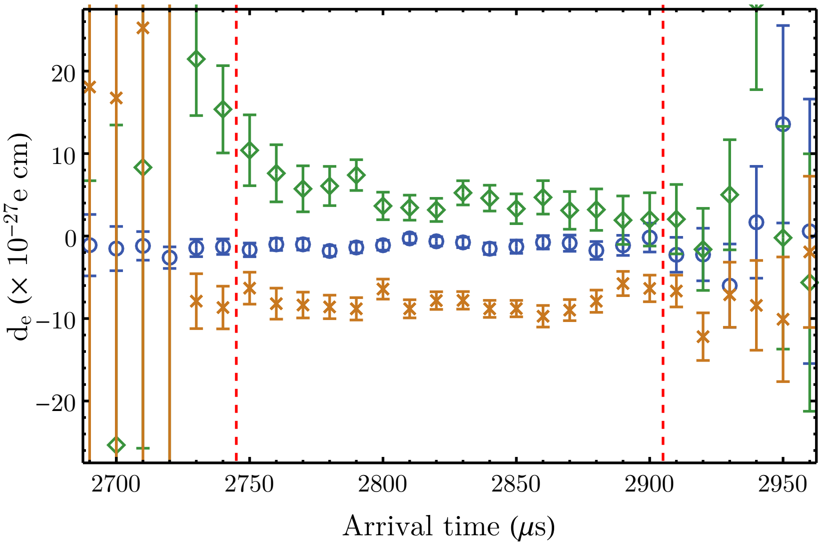

Figure 4.12.: The eEDM as a function of arrival time for the three clusters listed in Table 4.1. Blue circles: 24Oct1902. Green diamonds: 24Feb2004. Gold crosses: 02Mar2010. The second cluster shows a large increase in the eEDM at earlier arrival times (which corresponds to faster molecules). Note that systematic effects were being investigated in the green and gold datasets.

The results show that the estimates for the mean and error for d_e are consistent for all three methods used. The mean value does change significantly across clusters, but this is in part due to systematic tests that we were carrying out for the latter two clusters, so there is no significance to these changes. In order to better compare the experimental sensitivity for different clusters, we multiply the error estimate σ_{d_e} by $\sqrt{N_\mathrm{b}}$ to obtain an eEDM sensitivity per block of data. We can compare these to the shot-noise-limited sensitivities, ξ_{d_e}, calculated from Eq. (2.37) and including the excess noise factors due to the PMTs and laser scatter background described earlier in this chapter. We see that, at best, our experimental sensitivity is twice the shot-noise-limited sensitivity.

The first cluster analysed (24Oct1902) was the dataset used in a recent publication which stated that for 212 blocks analysed, the eEDM sensitivity was $\sigma_{d_e} = 1.8 \times 10^{-28}$ e cm [71]. This corresponds to a per-block statistical sensitivity of $\sigma_{d_e}\sqrt{N_\mathrm{b}} = 2.6 \times 10^{-27}$ e cm, which is smaller than the quoted per-block sensitivity in Table 4.1. This is because we had used Method II(a) in the data analysis for that paper, but without accounting for correlations and had therefore under-reported the error estimates. The second cluster analysed (24Feb2004) has worse sensitivity per block than the other two clusters, and we attribute this to an as-yet unresolved systematic effect which caused the value of

d_e to vary across the time-of-flight profile of the molecular beam pulse, as shown in Fig. 4.12 (green diamonds). The other two clusters (blue circles and gold crosses) show significantly less variation across the time bins. The remaining noise seen in the two "quieter" clusters is suspected to be magnetic noise.

4.5.3. Magnetic noise at block timescales

Previously, we had determined that any excess noise above the shot-noise for the asymmetry measurements was likely to be amplitude noise since both side-of-fringe and top-of-fringe measurements show no noticeable difference in the noise. However, these asymmetry measurements were taken over 40 s of integration time, whereas EDM data is taken over blocks that are six minutes long, which makes the latter more susceptible to low-frequency magnetic noise. Moreover, as seen in Fig. 3.22, the magnetic noise in the machine shows a strong $1/f$ behaviour below 1 Hz.

The `E` switch waveform does remove some of the noise. Taking Eq. (2.23) and adding a magnetic noise term β, the asymmetry measured in the i^{th} shot of a block is

$$\mathcal{A}_i = 2\mathcal{C}\left[(\delta\mathtt{B})_i\phi_{\delta B} + \mathtt{E}_i\mathtt{B}_i\phi_E + \mathtt{B}_i\phi_{\beta,i}\right], \tag{4.13}$$

where $\mathtt{E}_i$, $\mathtt{B}_i$ and $(\delta\mathtt{B})_i$ are the switch states in the i^{th} shot, and $\phi_{\beta,i} = g\mu_B\beta_i\tau/\hbar$ is the the i^{th} realisation of the phase noise due to β. The eEDM channel is then given by

$$\begin{aligned} \frac{\{\mathtt{E}\cdot\mathtt{B}\}}{\{\delta\mathtt{B}\}} &= \frac{\frac{1}{N}\sum_{i=1}^{N}\mathtt{E}_i\mathtt{B}_i\mathcal{A}_i}{\frac{1}{N}\sum_{i=1}^{N}(\delta\mathtt{B})_i\mathcal{A}_i} \\ &= \frac{\phi_E + \frac{1}{N}\sum_{i=1}^{N}\mathtt{E}_i\phi_{\beta,i}}{\phi_{\delta B}} \\ &= \frac{\phi_E}{\phi_{\delta B}} + \frac{1}{B_{\delta B}}\frac{1}{N}\sum_{i=1}^{N}\mathtt{E}_i\beta_i \\ &= \frac{\phi_E}{\phi_{\delta B}} + \frac{\beta_{\text{block}}}{B_{\delta B}}, \end{aligned} \tag{4.14}$$

where $N = 4096$ is the total number of shots in a block and β_{block} is the error term due to β. The error term averages to zero over many blocks if the noise is random, but its variance $\sigma^2_{\beta,\text{block}} = \overline{\beta^2_{\text{block}}}$ is non-zero. By defining the discrete Fourier transform (DFT) of β as

$$(F[\beta])_k = \frac{1}{\sqrt{N}} \sum_{j=1}^{N} \beta_j \mathrm{e}^{-i\frac{2\pi jk}{N}}, \tag{4.15}$$

we can show that the $\sigma^2_{\beta,\text{block}}$ can be written as [114]

$$\sigma^2_{\beta,\text{block}} = \frac{1}{N^2} \sum_{k=1}^{N} |(F[\beta])_k|^2 |(F^{-1}[\mathtt{E}])_k|^2, \tag{4.16}$$

where $F^{-1}[\mathtt{E}]$ is the inverse DFT of the switching waveform `E`. Thus, we find that the contribution of magnetic (phase) noise at some frequency is proportional to the Fourier component of the `E` waveform at that frequency. The `E` waveform is deliberately set to be slow because of hardware constraints; its largest Fourier components are between 0.01 and 0.1 Hz. Using Eq. (4.16) together with the known `E` waveform and magnetic noise spectrum of the main machine as measured by the magnetometers, we can calculate $\sigma_{\beta,\text{block}}$. We can also estimate the equivalent uncertainty in d_e arising from the magnetic field noise, given by

$$\sigma_{d_e,\beta,\text{block}} = \frac{g\mu_B \sigma_{\beta,\text{block}}}{\eta E_{\text{eff}}}. \tag{4.17}$$

The results are summarised in Table 4.2. Here, we also give the result of the measurement made inside the test shield where the magnetic field noise is at least ten times smaller.

We have also measured $\sigma_{\beta,\text{block}}$ directly by measuring “magnetic field blocks” where we carry out the experiment with the magnetometers operating, but without any molecules or changes in the applied field (effectively disabling the switches[4] `B` and δ`B`). For each block, the channel associated with switching the electric field direction, $\{\mathtt{E}\}_{\text{QuSpin}}$, for each of the magnetometers gives β_{block} for the block. The standard deviation of these channel values over a cluster of such blocks then gives $\sigma_{\beta,\text{block}}$. The results from a cluster of magnetic field blocks, consisting of $N_{\text{b}} = 133$ blocks, is shown in Table 4.2. The measured values for $\sigma_{\beta,\text{block}}$ agrees with the calculated values from offline measurements to within a factor of two. The equivalent magnetic noise in EDM units is also comparable to the measured eEDM sensitivities in Table 4.1, which leads us to believe that the excess noise we see in the EDM measurements is most likely due to magnetic field noise.

---

[4] We do this because the dynamic range of the *QuSpin* magnetometers is fairly small, on the order of the magnetic field step applied by δ`B`, so running the blocks with the magnetic field being stepped by `B` and δ`B` would make the magnetometer measurements unrealiable.

Table 4.2.: Magnetic field noise that our measurement of d_e is sensitive to, averaged over a block. We compare noise calculated from the measured magnetic field spectra shown in Fig. 3.22, to noise measured directly using magnetic field blocks, as described in the main text. We note that *QuSpin* 1 had operational issues at the time of taking magnetic field block data, and that the magnetometer used in the test shield was changed, but this did not affect the measurement result (as the noise is well above the noise floor of the magnetometers).

	Calculated*		Measured†	
Sensor	$\sigma_{\beta,\mathrm{block}}$(pT)	$\sigma_{d_e,\beta,\mathrm{block}}$($10^{-27}$ e cm)	$\sigma_{\beta,\mathrm{block}}$(pT)	$\sigma_{d_e,\beta,\mathrm{block}}$($10^{-27}$ e cm)
QuSpin 1	2.9	12	–	–
QuSpin 2	1.6	6.4	1.4	5.4
QuSpin 3	2.7	11	3.9	16
QuSpin 4	2.6	10	1.7	6.8
QuSpin 5	0.9	3.7	1.7	6.9
Test shield‡	0.14	0.58	0.09	0.37

[*] Calculated from Eq. (4.16) with $F[\beta]$ measured offline.

[†] Measured with magnetic field blocks.

[‡] *QuSpin* 2 used for calculated noise, whereas a second-generation *QuSpin* was used for the measured noise.

4.6. Summary

This chapter has focused primarily on identifying and minimising sources of noise in the experiment. First, I calculated excess noise factors due to secondary electron emission in the PMTs and laser scatter background. Next, I have described how we identified and reduced noise due to the beam pointing of the probe lasers and fluctuations in the laser frequency, and that there remains a small amount of excess noise from the latter. I have then shown how we can use the magnetometers and molecules themselves to identify sources of magnetic noise, which turned out to be primarily due to vibrations of the turbo pumps. With all these, we have managed to reduce the asymmetry noise to twice the shot-noise limit.

Next, I explained how we determined our sensitivity to the eEDM of the full experiment by introducing different averaging techniques we can use for our data. I have shown that the final sensitivity is independent of the chosen analysis method. The most recent cluster data obtained gives us an eEDM uncertainty per block of

$$\sigma_{d_e} = \frac{6.6 \times 10^{-27}\ e\ \mathrm{cm}}{\sqrt{N_\mathrm{b}}}, \tag{4.18}$$

which is just over twice the shot-noise limit for the cluster, given by

$$\xi^*_{d_e} = \frac{3.1 \times 10^{-27}\ e\ \mathrm{cm}}{\sqrt{N_\mathrm{b}}}, \tag{4.19}$$

which includes the excess noise factors, i.e. $\xi^*_{d_e} = \xi_{d_e}\sqrt{F_e F_{b,\mathcal{A}}}$. I have also shown how the noise above this limit is most likely due to slow magnetic noise, which are not picked up by the asymmetry measurements because the latter were carried out on a much faster timescale than the block measurements.

To conclude, we expect to take about $N_\mathrm{b} = 200$ blocks in a day, which gives us a per-day eEDM sensitivity of

$$\sigma_{d_e,\mathrm{day}} = \frac{4.7 \times 10^{-28}\ e\ \mathrm{cm}}{\sqrt{N_\mathrm{days}}}. \tag{4.20}$$

We expect to be able to take $N_\mathrm{days} = 100$ days worth of data, which would give us a final statistical sensitivity on the order of $\sigma_{d_e} \sim 5 \times 10^{-29}\ e$ cm.

5. Conclusions and outlook

This thesis describes an eEDM experiment with YbF molecules with a much-improved statistical sensitivity over its predecessor. In this final chapter, I review the main improvements made to the experiment. I then present an outlook for an eEDM measurement using YbF molecules at this level of precision and discuss its impact. Finally, I discuss potential improvements that can be made for a next-generation eEDM experiment using laser-cooled YbF molecules.

5.1. Summary of improvements

The improvements to the statistical sensitivity of the experiment have been achieved by increasing the number of useful molecules using a new state preparation scheme and improving the detection efficiency of these molecules by using an optical cycling transition for detection. These were first proposed in [85] and the initial implementation of these methods was first carried out in [86]. The state preparation scheme optically pumps molecules from the lowest three rotational states in the ground electronic and vibrational manifold into the absolute ground state of YbF, $(N, F) = (0, 0)$, which is the initial state of the experiment. In doing so, we increase the population in that state by a factor of 11.8. The previous method of state preparation only had one laser tuned to the $F = 1$ component of Q(0), and that yielded an increase in the $F = 0$ population by a factor of 1.9.

The state detection method has been changed from detecting $F = 0$ population directly using the Q(0) transition to detecting both $F = 0$ and $F = 1$ populations by coupling them to the $N = 1$ hyperfine levels and using the P(1) transition for detection. The

P(1) transition is rotationally-closed so molecules scatter photons until they decay to a higher-lying vibrational state. Since the branching ratio for that decay is 0.072, each molecule can scatter an average of 13.9 photons. This is an order of magnitude higher than the Q(0) detection method which scattered 1.2 photons per molecule on average. The new detection method also allows us to detect both $F = 0$ and $F = 1$ populations, thus doubling the number of molecules we detect.

A number of techniques were used to improve the detection efficiency and contrast of the interferometer. First, the polarisation of the probe lasers was modulated in two ways: by using an electro-optic modulator to directly modulate the polarisation of the lasers, and by counter-propagating the probe lasers to set up polarisation gradients along the beam direction. This was done to destabilise dark states that can form in the ground state manifold. This also reduces the amount of population left over in the $N = 1$ levels as the molecules move from the lower to upper detector; this leftover population causes detection crosstalk as leftover molecules from the lower $F = 0$ detector will be detected in the upper $F = 1$ detector. Second, a clean-up beam was introduced to the state preparation region to clear out any population from states in other isotopologues of YbF that was found to contribute to the background in the detectors. Third, the laser and microwave powers in the detectors were optimised to minimise off-resonant driving of the $F = 1$ state when detecting $F = 0$ population, and vice versa. We find that after applying these methods, we detect up to 11.9 photons per molecule on average, which is limited by the amount of interaction time between the molecules and probe lasers. We also find that the contrast is maximised at $\mathcal{C} = 0.6$, where the main limitation comes from leftover population (again, limited by interaction time in the detector) and incomplete pumping out of the $N = 1$ levels during state preparation, which also contributes to detection background.

The technical noise of the experiment was then characterised and minimised. The excess noise factor due to secondary electron emission in the PMTs was measured to be $F_e = 1.5$ which increases the detection noise by $\sqrt{F_e} = 1.2$. The laser scatter in the experiment was reduced by installing optical baffles in the probe laser ports and blackening the interior surfaces of the detection chamber. The residual scatter only contributes an increase in noise of $\sqrt{F_{\text{bg},\mathcal{A}}} = 1.1$. Probe laser frequency noise is expected to inflate the shot-noise uncertainty by a factor of 1.3, limited by the frequency stability of our laser lock. We can improve the performance of the laser lock to 0.2 MHz, which is the measured linewidth of our reference laser, by switching to an analog implementation of transfer cavity lock. Other sources of noise related to the probe lasers, such as beam pointing and power, were reduced and measured to be negligible at our level of sensitivity. The magnetic field noise in the experiment was characterised by newly-installed optical magnetometers from *QuSpin*. This allowed us to locate sources of noise, such as vibrations due to turbo pumps, and remove them.

5.2. Statistical sensitivity

In 2011, the published measurement reported a 1σ statistical uncertainty of 5.7×10^{-28} e cm from $N_\mathrm{b} = 6194$ blocks of data [57]. This uncertainty was limited entirely by the shot-noise [84]. This gave a per-block statistical uncertainty of

$$\sigma_{d_e}^{(2011)} = \frac{4.5 \times 10^{-26}}{\sqrt{N_\mathrm{b}}} e \text{ cm}. \tag{5.1}$$

Several small improvements were made between 2011 and 2013, including an upgrade of the rf transmission line, additional magnetic shielding and new high voltage supplies for the electric field plates [84]. The measured statistical uncertainty after these upgrades was 7.4×10^{-28} e cm from a dataset with $N_\mathrm{b} = 1074$, which translated to a per-block sensitivity of

$$\sigma_{d_e}^{(2013)} = \frac{2.4 \times 10^{-26}}{\sqrt{N_\mathrm{b}}} e \text{ cm}. \tag{5.2}$$

This was found to be 1.3 times the shot-noise limit, and the origin of excess noise had not been determined [84].

In this thesis, I have demonstrated a per-block sensitivity of

$$\sigma_{d_e}^{(2020)} = \frac{0.66 \times 10^{-26}}{\sqrt{N_\mathrm{b}}} e \text{ cm}. \tag{5.3}$$

I have also calculated the shot-noise limit, including excess noise due to the PMTs and laser scatter background, to be

$$\xi_{d_e}^{*(2020)} = \frac{0.31 \times 10^{-26}}{\sqrt{N_\mathrm{b}}} e \text{ cm}. \tag{5.4}$$

This shows that our experimental sensitivity is still 2.1 times the shot-noise limit, while we expect to be at best 1.3 times above this limit due to laser frequency noise. From auxiliary magnetic field block measurements using the *QuSpin* optical magnetometers, as described in Section 4.5.3, we find that the magnetic field noise in equivalent EDM units is

$$\sigma_B = \frac{0.64 \times 10^{-26}}{\sqrt{N_\mathrm{b}}} e \text{ cm}, \tag{5.5}$$

suggesting that our sensitivity is wholly limited by magnetic field noise. Using a set of test shields with a higher shielding factor, we find that a *QuSpin* magnetometer measures a magnetic field uncertainty (in EDM units) of

$$\sigma_B^{(\text{test})} = \frac{0.037 \times 10^{-26}}{\sqrt{N_\mathrm{b}}} e \text{ cm}. \tag{5.6}$$

This can be viewed as a lower bound to the magnetic field noise that can be measured in the lab by the *QuSpin* magnetometer. Therefore, it is entirely possibly to reduce the experimental uncertainty for d_e down to the shot-noise limit by improving the suppression of magnetic field noise in the main chamber of the experiment.

5.3. Outlook I: a near-term measurement of the eEDM

The shot-noise limit in Eq. (5.4) is a factor of 6.8 better than the experimental sensitivity demonstrated in 2013, and a factor of 14.5 better than that of the published measurement in 2011. We are able to take 200 blocks of data in a single day, and we plan to run the experiment for 100 days to obtain a dataset of $N_\mathrm{b} = 2 \times 10^4$ blocks. Assuming we are able to get to the shot-noise limit, the dataset will have a statistical sensitivity of

$$\sigma_{d_e}(\text{stat.}) = 2.2 \times 10^{-29} e \text{ cm}. \tag{5.7}$$

In order to make a measurement of d_e, we would need to be able to characterise systematic effects in the experiment at a precision better than that statistical uncertainty of Eq. (5.7). Table 5.1 lists the known systematic effects in the eEDM experiment and their current upper limits set by the 2011 and 2013 datasets. We are currently investigating

Table 5.1.: Table of current and projected upper limits for systematic errors in the experiment. There is currently no estimate for the systematic effect related to the high-voltage (HV) supplies, and this effect is not included in the estimate for the total uncertainty; see main text for a discussion.

Systematic effect	Current upper limit (10^{-29} e cm)	Projected upper limit (10^{-29} e cm)
HV supplies	–	–
Uncorrected E-asymmetry	6	0.8
Residual rf1 detuning	6	0.8
`E`-correlated magnetic fields	2.06*	0.83†
Voltage offset	0.63	0.63
rf rotation	0.84	0.84
Geometric phase	0.1	0.1
Motional magnetic field	0.005	0.005
Total	10.2	1.76

* The current limit is set by a combination of leakage current measurements and auxiliary offline shield magnetisation measurements [85].
† The projected limit is based on taking magnetic field blocks with the *QuSpin* magnetometers.

these systematic effects. The table also lists the projected upper limits for the current experiment.

The first of these is an unknown systematic effect related to the high-voltage (HV) supplies that generate the electric fields in the experiment [85]. As discussed in [85], this systematic error was difficult to analyse previously because its size was close to the statistical precision of the experiment. Now that the statistical precision is much better, we can return to a study of this effect.

The second effect is a possible shift in the value of d_e due to an asymmetry in the magnitude of the electric field, δE, upon reversal of its direction. The limit was set in 2013 by intentionally running the experiment with $\delta E = \pm 4.17\,\mathrm{V\,cm^{-1}}$ and measuring a gradient of $(\partial d_e/\partial(\delta E)) = (2.1 \pm 2.9) \times 10^{-28}$ e cm/(V/cm) [84]. When combined with a typical size of $\delta E \sim 0.1\,\mathrm{V\,cm^{-1}}$ in the experiment[1], this leads to the upper limit quoted in Table 5.1. The third effect is a residual correlation of the detuning of the first rf pulse,

---

[1] δE is estimated using the Stark shift of the molecules at the positions where the two rf pulses are applied, using the channels {`E`·`RF1F`} and {`E`·`RF2F`}, as described in Section 4.3.1 of [84].

δ_{rf1}, with the value of d_e. It was discovered during the 2011 measurement that there was a phase correlated with the detuning of both rf pulses which, when accompanied by an imperfect reversal of the electric field[2], causes a systematic shift of d_e. This was corrected on a block-by-block basis as described in [62]. However, even after the corrections were applied, it was found that when there was a voltage offset of the ground plane of the two field plates of order $\overline{V} = 100\,\mathrm{V}$, there remained a residual linear correlation of d_e with only δ_{rf1}. Although such a correlation was not present at $\overline{V} \sim 0$, a possible systematic shift was accounted for by multiplying the measured gradient $\partial d_e/\partial\delta_{\mathrm{rf1}}$ at zero offset, which was consistent with zero, with the average rf1 detuning for the dataset [84], giving the value in Table 5.1. For the second and third systematic effects, better measurements of the null gradients would reduce the size of the upper limits, which can be achieved with a better statistical sensitivity. I have therefore projected these upper limits to be reduced by a factor of 6.8, reflecting the gain in statistical sensitivity since 2013.

The fourth systematic effect concerns magnetic fields that are correlated with $\mathtt{E}$. Previously, the *Bartington* fluxgate magnetometers used were all external to the main vacuum chamber and we could not directly measure the magnetic field that the molecules see. Therefore, upper limits to the $\mathtt{E}$-correlated magnetic field were obtained by modelling the potential sources of such fields, such as leakage currents on the field plates and magnetisation of the inner magnetic shield, and making measurements of these quantities [85]. However, we now have a much more direct probe of the magnetic field inside the machine by using the *QuSpin* magnetometers. As described in Section 4.5.3, we can determine the size of any $\mathtt{E}$-correlated magnetic fields directly via the channel $\{\mathtt{E}\}_{\mathrm{QuSpin}}$ when taking magnetic field blocks. We plan to interleave these with regular blocks during data-taking. If we can get to the noise floor given by Eq. (5.6), and we take one magnetic field block for every 10 blocks of regular data (giving us 2000 magnetic field blocks), that will allow us to determine any $\mathtt{E}$-correlated magnetic fields to a precision of $8.3 \times 10^{-30}\ e\,\mathrm{cm}$.

The last four effects are sufficiently small that we will not need to discuss them here; they are described in [84]. In total, the systematic uncertainty is projected to be $1.76 \times 10^{-29}\ e\,\mathrm{cm}$, which when combined with the shot-noise-limited statistical uncer-

---

[2] An imperfect $\mathtt{E}$-reversal causes a different hyperfine Stark shift between the $F = 0$ and $F = 1$ states, leading to an $\mathtt{E}$-dependent rf detuning.

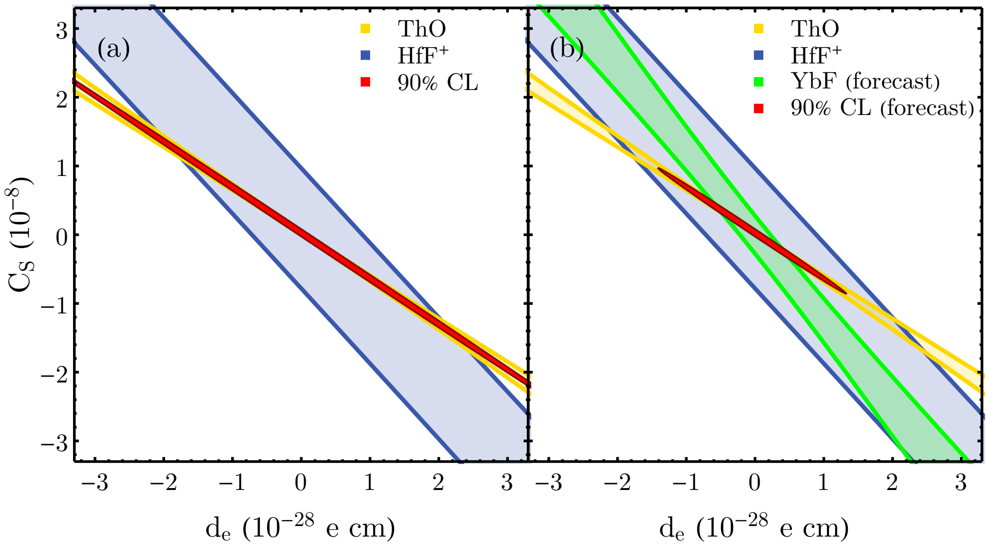

Figure 5.1.: Constraint plots for d_e and C_S. The sensitivities of each molecule to d_e and C_S are obtained from [22]. All bounds set by individual molecules are shown at the 1σ level. The red contour is the 90% confidence limit (CL) ellipse which combines all the measurements from individual molecular systems shown. (a) The 90% CL ellipse for the best measurements to date, which are the ThO and HfF$^+$ experiments. (b) The forecasted 90% confidence limit ellipse if we make a measurement with YbF molecules with an uncertainty given by Eq. (5.8).

tainty in Eq. (5.7), gives a total eEDM 1σ uncertainty of

$$\sigma_{d_e}^{\text{predicted}} = 2.8 \times 10^{-29}\ e\ \text{cm}. \tag{5.8}$$

Recall from the discussion in Section 1.1.3 that there are two CP-violating terms that contribute to the EDMs of paramagnetic atoms and molecules. The first is the electron EDM, d_e, and the second is the CP-violating scalar electron-nucleon interaction given by the parameter C_S. A measurement in a single system cannot measure both quantities. It is conventional to report the results of these measurements in terms of d_e alone, assuming $C_S = 0$. From measurements in two different systems, it becomes possible to constrain both d_e and C_S. Figure 5.1 shows the 90% confidence limit (CL) ellipse in the parameter space spanned by d_e and C_S obtained from the best current measurements, and shows how this would be reduced by a measurement in YbF at the level of sensitivity given in Eq. (5.8), assuming a central value of zero. The bounds in this plot, which are at the 1σ level, were calculated from the sensitivities of each molecular system to both d_e and C_S given in [22]. We see that the projected YbF measurement would significantly improve the current constraints, reducing the 90% CL on d_e and C_S by a factor of 3.2. This would be a very worthwhile improvement to our current knowledge of CP-violating quantities and interactions.

5.4. Outlook II: an eEDM experiment with laser-cooled YbF molecules

A next-generation eEDM experiment is currently being designed and built in our group. This experiment will use a cryogenic buffer-gas source of YbF, based on the design presented in [119], which has been shown to produce a molecular beam with an average forward speed of $160\,\mathrm{m\,s^{-1}}$ [80], a factor of 3.8 lower than the supersonic source we currently use for the eEDM experiment. Transverse laser cooling of YbF in one dimension has recently been demonstrated [80], and the extension to two dimensions is currently being tested. The eEDM experiment will then leverage the slower forward speed and much more collimated nature of the molecular beam by extending the interaction region to a length of 3.4 m, thus increasing the coherence time from 0.8 ms in the current experiment to 20 ms.

From the current experiment, we have learnt that the interaction time of the molecules with the lasers in the detection region limits both the number of photons scattered and contrast of the interferometer. The much slower beam in the new experiment will enable sufficient interaction time to overcome this limitation. Furthermore, we know that the incomplete pumping out of $N = 1$ molecules in the state preparation region is a large contributor to the background in the detectors. Thus, a dedicated clean-up region after the state preparation region is necessary to remove this population, which can be done using a laser tuned to the R(1) transition. An isotopically-pure source of Yb is also desirable as it would increase molecular yield and remove any background due to other Yb isotopes.

With these upgrades, the new experiment is expected to probe the eEDM at the 10^{-30} e cm to 10^{-31} e cm level, providing a platform for probing new physics at energies of 30–300 TeV.

A. An estimate of the enhancement factor

In Section 1.2, the EDM energy shift in paramagnetic atoms due to the electron EDM was given in Eq. (1.6) as

$$\Delta E_{\mathrm{edm}} = -2d_e \sum_{n\neq 0} \frac{\langle\phi_0|\, e\mathbf{r}\cdot\mathbf{E}_{\mathrm{ext}}\, |\phi_n\rangle \langle\phi_n|\, (1-\beta)\mathbf{\Sigma}\cdot\mathbf{E}_{\mathrm{int}}\, |\phi_0\rangle}{E_0 - E_n} - d_e \langle\phi_0|\, (1-\beta)\mathbf{\Sigma}\cdot\mathbf{E}_{\mathrm{ext}}\, |\phi_0\rangle\,. \tag{A.1}$$

We take the paramagnetic atom to be a hydrogen-like atom with nuclear charge Z. The Bohr radius is then $a = a_0/Z$, where a_0 is the Bohr radius for hydrogen. Then $\langle\phi_0|\, e\mathbf{r}\cdot\mathbf{E}_{\mathrm{ext}}\, |\phi_n\rangle \sim eaE_{\mathrm{ext}}$ and $|E_0 - E_n| \sim e^2/a$. Writing the term with $\mathbf{\Sigma}\cdot\mathbf{E}_{\mathrm{int}}$ out, we get

$$\langle\phi_n|\, (1-\beta)\mathbf{\Sigma}\cdot\mathbf{E}_{\mathrm{int}}\, |\phi_0\rangle = \langle\phi_n| \begin{pmatrix} 0 & 0 \\ 0 & \boldsymbol{\sigma}\cdot\mathbf{E}_{\mathrm{int}} \end{pmatrix} |\phi_0\rangle\,. \tag{A.2}$$

The operator only couples the small component of the wavefunctions, which are an order $\sim v/c$ smaller than the big components. The term can therefore be estimated as $\sim E_{\mathrm{int}} v^2/c^2$. The internal field is just the Coloumb field from the nucleus (at the Bohr radius): $E_{\mathrm{int}} \sim Ze/a^2$, and to estimate $(v/c)^2$ we can use the Bohr model where the electron undergoes circular motion due to the Coloumb potential:

$$\begin{aligned} \frac{m_e v^2}{a} = \frac{Ze^2}{4\pi\epsilon_0 a^2} &\implies m_e v^2 = \frac{Z^2 e^2}{4\pi\epsilon_0 a_0} \\ &\implies \frac{v^2}{c^2} = \frac{Z^2 e^2}{4\pi\epsilon_0 m_e c^2}\frac{m_e e^2}{4\pi\epsilon_0 \hbar^2} = Z^2\left(\frac{e}{4\pi\epsilon_0 \hbar c}\right)^2 = Z^2\alpha^2. \end{aligned} \tag{A.3}$$

Similarly, the second term in Eq. (A.1) can be estimated as $\langle\phi_0|\,(1-\beta)\boldsymbol{\Sigma}\cdot\mathbf{E}_{\text{ext}}\,|\phi_0\rangle \sim Z^2\alpha^2E_{\text{ext}}$. We can now estimate the EDM energy shift in paramagnetic atoms to be

$$\Delta E_{\text{edm}} \approx -2d_e e a E_{\text{ext}}\frac{a}{e^2}\frac{Ze}{a^2}Z^2\alpha^2 - d_e Z^2\alpha^2E_{\text{ext}} \approx -2d_eE_{\text{ext}}Z^3\alpha^2 \equiv -d_{\text{atom}}E_{\text{ext}}. \quad \text{(A.4)}$$

We have neglected the second term for heavy atoms, and the last equivalence shows the enhancement factor to be of order $R = d_{\text{atom}}/d_e \sim Z^3\alpha^2$.

B. Calculation of excess noise due to optical cycling detection

In this appendix, I calculate the excess noise factor due to optical cycling detection, F_{det}, following the methods given in [99]. This factor increases the uncertainty of the asymmetry measurements above the simple shot-noise limit given by the photon counts, i.e. for N detected photons this is $\sigma^2_{\mathcal{A}} = F_{\text{det}}/N$. Following Eq. (2.28), I discussed how each molecule scatters n_{sc} photons, where n_{sc} is a random variable. Lasner and DeMille [99] give a simple analysis of the distribution of n_{sc} arising from an optical cycling process such as ours. In short, it is a combination of a Poissonian distribution (arising from the randomness of spontaneous decay events) and a geometric distribution (since each decay event has a probability b of causing the molecule to end up in a dark state and therefore stop scattering photons). The mean and variance of n_{sc} are given by equations (6) and (7) of the aforementioned paper, and reproduced here:

$$\begin{aligned} \langle n_{\text{sc}} \rangle &= \frac{1-\mathrm{e}^{-brT}}{b}, \\ \sigma^2_{n_{\text{sc}}} &= \frac{1-b+\mathrm{e}^{-brT}b(2brT-2rT+1)-\mathrm{e}^{-2brT}}{b^2}, \end{aligned} \tag{B.1}$$

where r is the scattering rate and T is the interaction time of the molecules with the probe lasers. The scattering rate is given by $r = n_e\Gamma$, where $\Gamma = 2\pi \times 5.7\,\text{MHz}$ is the excited state linewidth [96] and n_e is the probability of occupying the excited state. An expression for n_e for this multi-level system can be found in [79, Appendix A], which I reproduce here:

$$n_e \simeq \frac{N_e}{(N_g+N_e)+2N_g^2 I_{\text{sat}}/I_{\text{tot}}}, \tag{B.2}$$

where N_g and N_e are the number of ground and excited state sublevels, respectively, $I_{\text{sat}} = \pi hc\Gamma/(3\lambda^3)$ is the two-level saturation intensity of the transition, and I_{tot} is the total intensity of the probe beams. This assumes that each sideband is addressed by an equal amount of laser intensity.

For the P(1) transition which we use to detect the molecules, we find that $b = 0.072$, $T = 20\,\mu\mathrm{s}$, $N_g = 12$, $N_e = 4$ and $I_{\mathrm{tot}} = 40 I_{\mathrm{sat}}$. Substituting these values into Eq. (B.1) gives $\langle n_{\mathrm{sc}} \rangle = 13.9$ and $\sigma^2_{n_{\mathrm{sc}}} = 179$. The excess detection factor is given, from Eq. (2.36), by

$$F_{\mathrm{det}} = 1 + \epsilon \left(1 - \frac{1}{\langle n_{\mathrm{sc}} \rangle} + \frac{\sigma^2_{n_{\mathrm{sc}}}}{\langle n_{\mathrm{sc}} \rangle^2} \right) = 1.15, \tag{B.3}$$

where $\epsilon = \epsilon_{\mathrm{c}} \langle n_{\mathrm{sc}} \rangle$ and $\epsilon_{\mathrm{c}} = 0.006$ is the collection efficiency of our detectors. This increases the shot-noise uncertainty of the experiment by $\sqrt{F_{\mathrm{det}}} = 1.07$.

Bibliography

[1] E. M. Purcell and N. F. Ramsey, "On the possibility of electric dipole moments for elementary particles and nuclei", Phys. Rev. **78**, 807 (1950).

[2] L. E. Ballentine, "Quantum mechanics: a modern development" (World Scientific, 1998).

[3] R. Golub and J. M. Pendlebury, "The electric dipole moment of the neutron", Contemp. Phys. **13**, 519 (1972).

[4] L. Landau, "On the conservation laws for weak interactions", Nucl. Phys. **3**, 127 (1957).

[5] C. S. Wu, E. Ambler, R. W. Hayward, D. D. Hoppes, and R. P. Hudson, "Experimental test of parity conservation in beta decay", Phys. Rev. **105**, 1413 (1957).

[6] R. L. Garwin, L. M. Lederman, and M. Weinrich, "Observations of the failure of conservation of parity and charge conjugation in meson decays: the magnetic moment of the free muon", Phys. Rev. **105**, 1415 (1957).

[7] J. I. Friedman and V. L. Telegdi, "Nuclear emulsion evidence for parity nonconservation in the decay chain $\Pi^+ - \mu^+ - e^+$", Phys. Rev. **105**, 1681 (1957).

[8] J. P. Lees et al. (*BaBar* Collaboration), "Observation of time-reversal violation in the B^0 meson system", Phys. Rev. Lett. **109**, 211801 (2012).

[9] J. Bernabéu, F. Martínez-Vidal, and P. Villanueva-Pérez, "Time reversal violation from the entangled $B^0\bar{B}^0$ system", J. High Energy Phys. **2012**, 64 (2012).

[10] I. B. Khriplovich and S. K. Lamoreaux, "CP violation without strangeness" (Springer Berlin Heidelberg, 1997).

[11] G. Lüders, "Proof of the TCP theorem", Ann. Phys. **2**, 1 (1957).

[12] R. Jost, "Eine Bemerkung zum CTP-Theorem", Helv. Phys. Acta **30**, 409 (1957).

[13] O. W. Greenberg, “Why is CPT fundamental?”, Found. Phys. **36**, 1535 (2006).

[14] M. Tanabashi et al. (Particle Data Group), “Review of particle physics”, Phys. Rev. D **98**, 030001 (2018).

[15] J. H. Christenson, J. W. Cronin, V. L. Fitch, and R. Turlay, “Evidence for the 2π decay of the K_2^0 meson”, Phys. Rev. Lett. **13**, 138 (1964).

[16] B. Aubert et al. (*BaBar* Collaboration), “Observation of CP violation in the B^0 meson system”, Phys. Rev. Lett. **87**, 091801 (2001).

[17] L. Canetti, M. Drewes, and M. Shaposhnikov, “Matter and antimatter in the universe”, New J. Phys. **14**, 095012 (2012).

[18] A. D. Sakharov, “Violation of CP invariance, C asymmetry, and baryon asymmetry of the universe”, Sov. Phys. Usp. **34**, 392 (1991).

[19] J. M. Cline, “Baryogenesis”, in *Particle physics and cosmology: the fabric of spacetime* (Elsevier, 2007), pp. 53–116.

[20] R. P. Feynman and M. Gell-Mann, “Theory of the fermi interaction”, Phys. Rev. **109**, 193 (1958).

[21] M. Kobayashi and T. Maskawa, “CP-violation in the renormalizable theory of weak interaction”, Prog. Theor. Phys. **49**, 652 (1973).

[22] T. E. Chupp, P. Fierlinger, M. J. Ramsey-Musolf, and J. T. Singh, “Electric dipole moments of atoms, molecules, nuclei, and particles”, Rev. Mod. Phys. **91**, 015001 (2019).

[23] R. D. Peccei, “The strong CP problem and axions”, in *Axions* (Springer Berlin Heidelberg, 2008), pp. 3–17.

[24] M. Pospelov and A. Ritz, “CKM benchmarks for electron electric dipole moment experiments”, Phys. Rev. D **89**, 056006 (2014).

[25] V. Andreev et al. (ACME Collaboration), “Improved limit on the electric dipole moment of the electron”, Nature **562**, 355 (2018).

[26] Y. Li, S. Profumo, and M. Ramsey-Musolf, “A comprehensive analysis of electric dipole moment constraints on CP-violating phases in the MSSM”, J. High Energy Phys. **2010**, 62 (2010).

[27] M. S. Safronova, D. Budker, D. DeMille, D. F. J. Kimball, A. Derevianko, and C. W. Clark, “Search for new physics with atoms and molecules”, Rev. Mod. Phys. **90**, 025008 (2018).

[28] V. Cirigliano and M. J. Ramsey-Musolf, “Low energy probes of physics beyond the standard model”, Prog. Part. Nucl. Phys. **71**, 2 (2013).

[29] J. Engel, M. J. Ramsey-Musolf, and U. van Kolck, “Electric dipole moments of nucleons, nuclei, and atoms: the standard model and beyond”, Prog. Part. Nucl. Phys. **71**, 21 (2013).

[30] N. F. Ramsey, “Molecular beams” (Oxford University Press, 1956).

[31] J. S. M. Ginges and V. V. Flambaum, “Violations of fundamental symmetries in atoms and tests of unification theories of elementary particles”, Phys. Rep. **397**, 63 (2004).

[32] T. Chupp and M. Ramsey-Musolf, “Electric dipole moments: a global analysis”, Phys. Rev. C **91**, 035502 (2015).

[33] P. A. Zyla et al. (Particle Data Group), “Review of particle physics”, Prog. Theor. Exp. Phys. **2020**, 083C01 (2020).

[34] C. Cesarotti, Q. Lu, Y. Nakai, A. Parikh, and M. Reece, “Interpreting the electron EDM constraint”, J. High Energy Phys. **2019**, 59 (2019).

[35] L. I. Schiff, “Measurability of nuclear electric dipole moments”, Phys. Rev. **132**, 2194 (1963).

[36] P. G. H. Sandars, “The electric dipole moment of an atom”, Phys. Lett. **14**, 194 (1965).

[37] E. A. Hinds, “Testing time reversal symmetry using molecules”, Phys. Scr. **T70**, 34 (1997).

[38] M. G. Kozlov and L. N. Labzowsky, “Parity violation effects in diatomics”, J. Phys. B: At. Mol. Opt. Phys. **28**, 1933 (1995).

[39] E. D. Commins, “Electric dipole moments of leptons”, Adv. At. Mol., Opt. Phys. **40**, 1 (1999).

[40] V. A. Dzuba and V. V. Flambaum, “Calculation of the (T,P)-odd electric dipole moment of thallium and cesium”, Phys. Rev. A **80**, 062509 (2009).

[41] D. Mukherjee, B. K. Sahoo, H. S. Nataraj, and B. P. Das, “Relativistic coupled cluster (RCC) computation of the electric dipole moment enhancement factor of francium due to the violation of time reversal symmetry”, J. Phys. Chem. A **113**, 12549 (2009).

[42] A.-M. Mårtensson-Pendrill and P. Öster, “Calculations of atomic electric dipole moments”, Phys. Scr. **36**, 444 (1987).

[43] S. A. Murthy, D. Krause, Z. L. Li, and L. R. Hunter, “New limits on the electron electric dipole moment from cesium”, Phys. Rev. Lett. **63**, 965 (1989).

[44] B. C. Regan, E. D. Commins, C. J. Schmidt, and D. DeMille, “New limit on the electron electric dipole moment”, Phys. Rev. Lett. **88**, 071805 (2002).

[45] B. Graner, Y. Chen, E. G. Lindahl, and B. R. Heckel, “Reduced limit on the permanent electric dipole moment of ^{199}Hg”, Phys. Rev. Lett. **116**, 161601 (2016).

[46] B. C. Regan, “A search for violation of time-reversal symmetry in atomic thallium”, PhD thesis (University of California at Berkeley, 2001).

[47] O. P. Sushkov and V. V. Flambaum, “Parity breaking effects in diatomic molecules”, Zh. Eksp. Teor. Fiz. **75**, 1208 (1978).

[48] P. G. H. Sandars, “Measurability of the proton electric dipole moment”, Phys. Rev. Lett. **19**, 1396 (1967).

[49] M. G. Kozlov, “Enhancement of the electric dipole moment of the electron in the YbF molecule”, J. Phys. B: At. Mol. Opt. Phys. **30**, L607 (1997).

[50] M. G. Kozlov, A. V. Titov, N. S. Mosyagin, and P. V. Souchko, “Enhancement of the electric dipole moment of the electron in the BaF molecule”, Phys. Rev. A **56**, R3326 (1997).

[51] A. N. Petrov, A. V. Titov, T. A. Isaev, N. S. Mosyagin, and D. DeMille, “Configuration-interaction calculation of hyperfine and P,T-odd constants on ^{207}PbO excited states for electron electric-dipole-moment experiments”, Phys. Rev. A **72**, 022505 (2005).

[52] L. V. Skripnikov, “Combined 4-component and relativistic pseudopotential study of ThO for the electron electric dipole moment search”, J. Chem. Phys. **145**, 214301 (2016).

[53] T. Fleig, “P,T-odd and magnetic hyperfine-interaction constants and excited-state lifetime for HfF^+”, Phys. Rev. A **96**, 040502 (2017).

[54] L. V. Skripnikov, “Communication: theoretical study of HfF^+ cation to search for the T,P-odd interactions”, J. Chem. Phys. **147**, 021101 (2017).

[55] M. Denis, M. S. Nørby, H. J. A. Jensen, A. S. P. Gomes, M. K. Nayak, S. Knecht, and T. Fleig, "Theoretical study on ThF^+, a prospective system in search of time-reversal violation", New J. Phys. **17**, 043005 (2015).

[56] M. Denis, P. A. B. Haase, R. G. E. Timmermans, E. Eliav, N. R. Hutzler, and A. Borschevsky, "Enhancement factor for the electric dipole moment of the electron in the BaOH and YbOH molecules", Phys. Rev. A **99**, 042512 (2019).

[57] J. J. Hudson, D. M. Kara, I. J. Smallman, B. E. Sauer, M. R. Tarbutt, and E. A. Hinds, "Improved measurement of the shape of the electron", Nature **473**, 493 (2011).

[58] S. Eckel, P. Hamilton, E. Kirilov, H. W. Smith, and D. DeMille, "Search for the electron electric dipole moment using Ω-doublet levels in PbO", Phys. Rev. A **87**, 052130 (2013).

[59] W. B. Cairncross, D. N. Gresh, M. Grau, K. C. Cossel, T. S. Roussy, Y. Ni, Y. Zhou, J. Ye, and E. A. Cornell, "Precision measurement of the electron's electric dipole moment using trapped molecular ions", Phys. Rev. Lett. **119**, 153001 (2017).

[60] J. J. Hudson, B. E. Sauer, M. R. Tarbutt, and E. A. Hinds, "Measurement of the electron electric dipole moment using YbF molecules", Phys. Rev. Lett. **89** (2002).

[61] J. J. Hudson, "Measuring the electric dipole moment of the electron with YbF molecules", PhD thesis (University of Sussex, 2001).

[62] D. M. Kara, I. J. Smallman, J. J. Hudson, B. E. Sauer, M. R. Tarbutt, and E. A. Hinds, "Measurement of the electron's electric dipole moment using YbF molecules: methods and data analysis", New J. Phys. **14**, 103051 (2012).

[63] S. Bickman, P. Hamilton, Y. Jiang, and D. DeMille, "Preparation and detection of states with simultaneous spin alignment and selectable molecular orientation in PbO", Phys. Rev. A **80**, 023418 (2009).

[64] P. Hamilton, "Preliminary results in the search for the electron electric dipole moment in PbO*", PhD thesis (Yale University, 2010).

[65] J. Baron et al. (ACME Collaboration), "Order of magnitude smaller limit on the electric dipole moment of the electron", Science **343**, 269 (2013).

[66] N. R. Hutzler, “A new limit on the electron electric dipole moment: beam production, data interpretation and systematics”, PhD thesis (Harvard University, 2014).

[67] A. C. Vutha, B. Spaun, Y. V. Gurevich, N. R. Hutzler, E. Kirilov, J. M. Doyle, G. Gabrielse, and D. DeMille, “Magnetic and electric dipole moments of the $H^3\Delta_1$ state in ThO”, Phys. Rev. A **84**, 034502 (2011).

[68] C. D. Panda, B. R. O’Leary, A. D. West, J. Baron, P. W. Hess, C. Hoffman, E. Kirilov, C. B. Overstreet, E. P. West, D. DeMille, J. M. Doyle, and G. Gabrielse, “Stimulated raman adiabatic passage preparation of a coherent superposition of ThO $H^3\Delta_1$ states for an improved electron electric-dipole-moment measurement”, Phys. Rev. A **93**, 052110 (2016).

[69] H. Loh, K. C. Cossel, M. C. Grau, K.-K. Ni, E. R. Meyer, J. L. Bohn, J. Ye, and E. A. Cornell, “Precision spectroscopy of polarized molecules in an ion trap”, Science **342**, 1220 (2013).

[70] W. B. Cairncross, “Searching for time-reversal symmetry violation with molecular ions: quantum state control and photofragment imaging”, PhD thesis (University of Colorado, 2019).

[71] C. J. Ho, J. A. Devlin, I. M. Rabey, P. Yzombard, J. Lim, S. C. Wright, N. J. Fitch, E. A. Hinds, M. R. Tarbutt, and B. E. Sauer, “New techniques for a measurement of the electron’s electric dipole moment”, New J. Phys. **22**, 053031 (2020).

[72] Y. Zhou, Y. Shagam, W. B. Cairncross, K. B. Ng, T. S. Roussy, T. Grogan, K. Boyce, A. Vigil, M. Pettine, T. Zelevinsky, J. Ye, and E. A. Cornell, “Second-scale coherence measured at the quantum projection noise limit with hundreds of molecular ions”, Phys. Rev. Lett. **124**, 053201 (2020).

[73] X. Wu, Z. Han, J. Chow, D. G. Ang, C. Meisenhelder, C. D. Panda, E. P. West, G. Gabrielse, J. M. Doyle, and D. DeMille, “The metastable $Q^3\Delta_2$ state of ThO: a new resource for the ACME electron EDM search”, New J. Phys. **22**, 023013 (2020).

[74] K.-K. Ni, H. Loh, M. Grau, K. C. Cossel, J. Ye, and E. A. Cornell, “State-specific detection of trapped HfF^+ by photodissociation”, J. Mol. Spec. **300**, 12 (2014).

[75] A. C. Vutha, W. C. Campbell, Y. V. Gurevich, N. R. Hutzler, M. Parsons, D. Patterson, E. Petrik, B. Spaun, J. M. Doyle, G. Gabrielse, and D. DeMille, "Search for the electric dipole moment of the electron with thorium monoxide", J. Phys. B: At. Mol. Opt. Phys. **43**, 074007 (2010).

[76] T. Cheng, "Progress towards a measurement of the electron electric dipole moment using cold cesium", PhD thesis (Pennsylvania State University, 2018).

[77] T. Inoue et al., "Experimental search for the electron electric dipole moment with laser cooled francium atoms", Hyperfine Interact. **231**, 157 (2014).

[78] P. Aggarwal et al. (NL-*e*EDM Collaboration), "Measuring the electric dipole moment of the electron in BaF", Eur. Phys. J. D **72**, 197 (2018).

[79] M. R. Tarbutt, B. E. Sauer, J. J. Hudson, and E. A. Hinds, "Design for a fountain of YbF molecules to measure the electron's electric dipole moment", New J. Phys. **15**, 053034 (2013).

[80] J. Lim, J. R. Almond, M. A. Trigatzis, J. A. Devlin, N. J. Fitch, B. E. Sauer, M. R. Tarbutt, and E. A. Hinds, "Laser cooled YbF molecules for measuring the electron's electric dipole moment", Phys. Rev. Lett. **120**, 123201 (2018).

[81] B. L. Augenbraun, Z. D. Lasner, A. Frenett, H. Sawaoka, C. Miller, T. C. Steimle, and J. M. Doyle, "Laser-cooled polyatomic molecules for improved electron electric dipole moment searches", New J. Phys. **22**, 022003 (2020).

[82] I. Kozyryev and N. R. Hutzler, "Precision measurement of time-reversal symmetry violation with laser-cooled polyatomic molecules", Phys. Rev. Lett. **119**, 133002 (2017).

[83] A. Vutha, M. Horbatsch, and E. Hessels, "Oriented polar molecules in a solid inert-gas matrix: a proposed method for measuring the electric dipole moment of the electron", Atoms **6**, 3 (2018).

[84] I. J. Smallman, "A new measurement of the electron electric dipole moment using ytterbium fluoride", PhD thesis (Imperial College London, 2013).

[85] J. A. Devlin, "Progress towards a more sensitive measurement of the electron electric dipole moment with YbF", PhD thesis (Imperial College London, 2015).

[86] I. M. Rabey, "Improved shot noise limit of the YbF EDM experiment", PhD thesis (Imperial College London, 2016).

[87] J. Wang, "Laser and radiofrequency spectroscopy of ytterbium fluoride ground state", PhD thesis (Yale University, 1996).

[88] B. E. Sauer, S. B. Cahn, M. G. Kozlov, G. D. Redgrave, and E. A. Hinds, "Perturbed hyperfine doubling in the and [18.6]0.5 states of YbF", J. Chem. Phys. **110**, 8424 (1999).

[89] K. L. Dunfield, C. Linton, T. E. Clarke, J. McBride, A. G. Adam, and J. R. D. Peers, "Laser spectroscopy of the lanthanide monofluorides: analysis of the $A^2\Pi$–$X^2\Sigma^+$ transition of ytterbium monofluoride", J. Mol. Spec. **174**, 433 (1995).

[90] B. E. Sauer, J. Wang, and E. A. Hinds, "Laser-rf double resonance spectroscopy of ^{174}YbF in the $X^2\Sigma^+$ state: spin-rotation, hyperfine interactions, and the electric dipole moment", J. Chem. Phys. **105**, 7412 (1996).

[91] J. M. Brown and A. Carrington, "Rotational spectroscopy of diatomic molecules" (Cambridge University Press, 2003).

[92] H. Lefebvre-Brion and R. W. Field, "Perturbations in the spectra of diatomic molecules" (Academic Press, 1986).

[93] J. Lim, J. R. Almond, M. R. Tarbutt, D. T. Nguyen, and T. C. Steimle, "The [557]–$X^2\Sigma^+$ and [561]–$X^2\Sigma^+$ bands of ytterbium fluoride, ^{174}YbF", J. Mol. Spec. **338**, 81 (2017).

[94] B. E. Sauer, J. Wang, and E. A. Hinds, "Anomalous spin-rotation coupling in the $X^2\Sigma^+$ state of YbF", Phys. Rev. Lett. **74**, 1554 (1995).

[95] C. H. Townes and A. L. Schawlow, "Microwave spectroscopy" (Dover Publications, 1975).

[96] X. Zhuang, A. Le, T. C. Steimle, N. E. Bulleid, I. J. Smallman, R. J. Hendricks, S. M. Skoff, J. J. Hudson, B. E. Sauer, E. A. Hinds, and M. R. Tarbutt, "Franck-Condon factors and radiative lifetime of the $A^2\Pi_{1/2}$–$X^2\Sigma^+$ transition of ytterbium monofluoride, YbF", Phys. Chem. Chem. Phys. **13**, 19013 (2011).

[97] M. R. Tarbutt, J. J. Hudson, B. E. Sauer, E. A. Hinds, V. A. Ryzhov, V. L. Ryabov, and V. F. Ezhov, "A jet beam source of cold YbF radicals", J. Phys. B: At. Mol. Opt. Phys. **35**, 5013 (2002).

[98] W. M. Itano, J. C. Bergquist, J. J. Bollinger, J. M. Gilligan, D. J. Heinzen, F. L. Moore, M. G. Raizen, and D. J. Wineland, "Quantum projection noise: population fluctuations in two-level systems", Phys. Rev. A **47**, 3554 (1993).

[99] Z. Lasner and D. DeMille, "Statistical sensitivity of phase measurements via laser-induced fluorescence with optical cycling detection", Phys. Rev. A **98**, 053823 (2018).

[100] S. M. Ross, "Introduction to probability models", 11th ed. (Academic Press, 2014).

[101] A. Stuart and J. K. Ord, "Kendall's advanced theory of statistics: volume 1: distribution theory", 6th ed. (John Wiley and Sons, 1994).

[102] P. C. Condylis, "Measuring the electron electric dipole moment using supersonic YbF", PhD thesis (Imperial College London, 2006).

[103] W. Z. Zhao, J. E. Simsarian, L. A. Orozco, and G. D. Sprouse, "A computer-based digital feedback control of frequency drift of multiple lasers", Rev. Sci. Instrum. **69**, 3737 (1998).

[104] D. M. Kara, "Toward an electron electric dipole moment measurement using ytterbium fluoride", PhD thesis (Imperial College London, 2010).

[105] B. E. Sauer, D. M. Kara, J. J. Hudson, M. R. Tarbutt, and E. A. Hinds, "A robust floating nanoammeter", Rev. Sci. Instrum. **79**, 126102 (2008).

[106] I. M. Rabey, J. A. Devlin, E. A. Hinds, and B. E. Sauer, "Low magnetic Johnson noise electric field plates for precision measurement", Rev. Sci. Instrum. **87**, 115110 (2016).

[107] D. C. Faircloth, "Technological aspects: high voltage", in *CERN-2013-007* (2014), pp. 381–419.

[108] R. J. Noer, "Electron field emission from broad-area electrodes", Appl. Phys. A **28**, 1 (1982).

[109] D. J. Berkeland and M. G. Boshier, "Destabilization of dark states and optical spectroscopy in Zeeman-degenerate atomic systems", Phys. Rev. A **65**, 033413 (2002).

[110] J. Osborne, J. Orton, O. Alem, and V. Shah, "Fully integrated, standalone zero field optically pumped magnetometer for biomagnetism", in Steep dispersion engineering and opto-atomic precision metrology XI, Proc. SPIE 10548, 105481G (2018).

[111] W. Happer and H. Tang, "Spin-exchange shift and narrowing of magnetic resonance lines in optically pumped alkali vapors", Phys. Rev. Lett. **31**, 273 (1973).

[112] I. K. Kominis, T. W. Kornack, J. C. Allred, and M. V. Romalis, "A subfemtotesla multichannel atomic magnetometer", Nature **422**, 596 (2003).

[113] T. J. Sumner, J. M. Pendlebury, and K. F. Smith, "Conventional magnetic shielding", J. Phys. D **20**, 1095 (1987).

[114] J. J. Hudson, M. R. Tarbutt, B. E. Sauer, and E. A. Hinds, "Stochastic multichannel lock-in detection", New J. Phys. **16**, 013005 (2014).

[115] M. Teich, K. Matsuo, and B. Saleh, "Excess noise factors for conventional and superlattice avalanche photodiodes and photomultiplier tubes", IEEE J. Quantum Electron. **22**, 1184 (1986).

[116] J. J. Hudson, H. T. Ashworth, D. M. Kara, M. R. Tarbutt, B. E. Sauer, and E. A. Hinds, "Pulsed beams as field probes for precision measurement", Phys. Rev. A **76**, 033410 (2007).

[117] M. Schmelling, "Averaging correlated data", Phys. Scr. **51**, 676 (1995).

[118] B. Efron and R. Tibshirani, "Bootstrap methods for standard errors, confidence intervals, and other measures of statistical accuracy", Stat. Sci. **1**, 54 (1986).

[119] S. Truppe, M. Hambach, S. M. Skoff, N. E. Bulleid, J. S. Bumby, R. J. Hendricks, E. A. Hinds, B. E. Sauer, and M. R. Tarbutt, "A buffer gas beam source for short, intense and slow molecular pulses", J. Mod. Opt. **65**, 648 (2017).